1990

Solid state chemistry of centered zirconium chloride clusters: synthesis and characterization of new compounds

Jie Zhang
Iowa State University

INFORMATION TO USERS

The most advanced technology has been used to photograph and reproduce this manuscript from the microfilm master. UMI films the text directly from the original or copy submitted. Thus, some thesis and dissertation copies are in typewriter face, while others may be from any type of computer printer.

The quality of this reproduction is dependent upon the quality of the copy submitted. Broken or indistinct print, colored or poor quality illustrations and photographs, print bleedthrough, substandard margins, and improper alignment can adversely affect reproduction.

In the unlikely event that the author did not send UMI a complete manuscript and there are missing pages, these will be noted. Also, if unauthorized copyright material had to be removed, a note will indicate the deletion.

Oversize materials (e.g., maps, drawings, charts) are reproduced by sectioning the original, beginning at the upper left-hand corner and continuing from left to right in equal sections with small overlaps. Each original is also photographed in one exposure and is included in reduced form at the back of the book.

Photographs included in the original manuscript have been reproduced xerographically in this copy. Higher quality 6" x 9" black and white photographic prints are available for any photographs or illustrations appearing in this copy for an additional charge. Contact UMI directly to order.

U·M·I

University Microfilms International
A Bell & Howell Information Company
300 North Zeeb Road, Ann Arbor, MI 48106-1346 USA
313/761-4700 800/521-0600

Order Number 9110584

Solid state chemistry of centered zirconium chloride clusters. Synthesis and characterization of new compounds

Zhang, Jie, Ph.D.

Iowa State University, 1990

U·M·I
300 N. Zeeb Rd.
Ann Arbor, MI 48106

Solid state chemistry of centered zirconium chloride clusters. Synthesis and characterization of new compounds

by

Jie Zhang

A Dissertation Submitted to the
Graduate Faculty in Partial Fulfillment of the
Requirements for the Degree of
DOCTOR OF PHILOSOPHY

Department: Chemistry
Major: Inorganic Chemistry

Approved:

Signature was redacted for privacy.

In Charge of Major Work

Signature was redacted for privacy.

For the Major Department

Signature was redacted for privacy.

For the Graduate College

Iowa State University
Ames, Iowa

1990

TABLE OF CONTENTS

INTRODUCTION

Since the discovery of the first group of cluster compounds, namely the reduced niobium and tantalum halides,[1,2] the cluster chemistry of early transition metals[3] and rare-earth metals[4] has been under intensive study. During the past twenty-five years, a large number of cluster compounds with various structural features have been synthesized and characterized, including metal-rich halides, chalcogenides and, more recently, reduced oxides as well as mixed chalcogenide and halides.[5-7] Although research in this area has involved solution chemistry,[8-10] the synthesis of cluster compounds is dominated by solid state routes, which are by far the most effective means of assembling atoms into clusters with extensive metal–metal bonding interactions.

Today, the study of the compounds has become an increasingly important branch of solid state chemistry, because it not only provides new, interesting and more complex solid state substances, but also contributes to the understanding of the structure and bonding features of solid state systems. In addition, investigations in this field have generated new solid state materials with specific or unusual properties as well as practical or potential applications.

The majority of the known cluster phases have discrete or condensed octahedral M_6 units as their basic building blocks. These phases are further divided into two categories according to the functionality of the ligands. The M_6X_8-type clusters have face-capping ligands, whereas M_6X_{12}-type clusters have edge-bridging ligands (inner ligands x^i's).[3] Furthermore, the vertices of the metal cores are connected to terminal ligands (outer ligands, X^a's) in both cases. In general, compounds that

have higher electron counts and contain a relative larger ligand X and smaller metal M prefer an M_6X_8 structure, for example, Ti_5Te_4,[11] Nb_6I_{11}[12-13] and Mo_6S_8.[14] In contrast, a cluster phase with relatively larger metal cores and lesser electron counts adopts M_6X_{12} structure, as in the cases of $Sc_7Cl_{12}C$,[15] $Zr_6I_{12}C$,[16] Nb_6F_{15}[17] and Ta_6Cl_{15}.[18]

The presence of an additional chemical and structural component, an interstitial atom, has been known since the beginning of the cluster chemistry for phases either with an extended metal matrix[19-20] or with a discrete cluster unit.[21,22] However, this phenomenon was usually treated in connection with impurity problems, and the interstitial elements were limited to H, C, N, and O. It was not until the late 1970s that the importance of the interstitial atoms in cluster formation and stabilization was recognized, investigated, rationalized, and appreciated. By occupying the void inside a metal core this interstitial atom provides strong bonding interaction with the host atoms; in addition, it also contributes its valence electrons to the metal–metal bonding band of the cluster, therefore stabilizing an otherwise electron-deficient cluster.[23] Since then, elements that cover a large portion of the periodic table have been introduced into the syntheses consciously, resulting in a rapid expansion in not only the number but also the structure variety of the cluster compounds. The research work in this area began with light main-group elements (H,Be–N)[24-29] and later expanded to heavier main group atoms (Al–P, Ge).[30,31] Soon after, clusters stabilized by 3d transition metals (Cr–Ni) were discovered,[32-34] which renewed the concept of the interstitial atoms. The next breakthrough of centered cluster chemistry

was the successful syntheses of clusters centered by 4d and 5d transition metals (Rh, Ru, Pd, Re–Os, Ir, Pt, Au).[10,34-36] As the number of the valence electrons of the interstitial atoms change, systematic studies of the electronic configuration of the cluster phases become possible. Moreover, as the cluster size varies, the richness and beauty of structure chemistry of cluster phases are uncovered, especially marked by the recent achievement of synthesizing condensed superclusters[36] centered by 4d and 5d transition metals.

Among the centered cluster phases, the zirconium chloride clusters form a unique family. They are at the present the most extensively studied and the best described and understood systems. As a result of continuous efforts during the past ten years, a rich solid-state chemistry has been revealed, in company of the advances of synthetic techniques and the development of new characterization methods.[26,37] Meanwhile, a new cluster chemistry that fills the gap between the traditional solid state chemistry and the conventional solution chemistry has also been established.[9,10] Each Zr–Cl cluster phase obtained via the solid state route can be considered as a member of the $M_m(Zr_6Cl_{12}Z)Cl_n$ series[26] (M = alkali metal, alkaline earth metal, rare-earth metal, or Zr; Z = H, Be–N, Mn–Ni; $0 \leq n \leq 6$, $0 \leq m \leq 6$). These obey the cluster electron counting rules, 14 electrons per cluster for Z = main group element[24,37] and 18 electrons per cluster for Z = transition metal[32,33] with only a few exceptions. The variation of the interstitial atoms and countercations allow one to generate a large number of new cluster phases of various chemical compositions within the electron rules. These also lead to a large range of Zr/Cl ratios, and therefore,

to the remarkable versatility of the cluster connectivities and structure types shown in Table 1.

The remainder of this thesis will present the advances in the solid-state chemistry of Zr–Cl clusters since 1986. Part of the progress arose from the encapsulation of 3d transition metals (Mn–Ni) in the Zr_6 core. These interstitials not only produced a group of transition-metal-centered Zr–Cl clusters with known structure types but also generated several structure types that were new to Zr–Cl clusters or even to the entire metal cluster field. The accommodation of multivalent counter cations is the other important factor associated with the recent development in solid state Zr–Cl cluster chemistry. It provides a series of 6–18 cluster phases with intriguing structural relationships, and it provided the first cluster phase of M_6X_{17} stoichiometry and a new cluster connectivity,[38] therefore completing the cluster series of $[Zr_6Cl_{12}Z]Cl_n$ ($0 \leq n \leq 6$).

The following sections will discuss the synthesis and characterization of the new Zr–Cl cluster compounds. As their electronic characters, namely, via 14- and 18-cluster electron counting rules, have been well explained in terms of molecular orbitals prior to this work, the emphasis of the succeeding sections will be on the new structural features and relationships of the new cluster phases. The effects of the size of the interstitial atom and of the charge, number, and size of the countercations on the structure variations and modifications will also be addressed.

Table 1. The known structure types and cluster connectivities among the $[Zr_6Cl_{12}Z]Cl_n$ series (n = 0–6)

Connectivity	Structure Type	Space Group	References
$[Zr_6Cl^i_{12}Z]Cl^a_6$	$Li_6Zr_6Cl_{18}H$	$R\bar{3}$	39, this work
	$Rb_5Zr_6Cl_{18}B$	Pmna	40
	$K_4Nb_6Cl_{18}$	C2/m	41
	$Ba_3Zr_6Cl_{18}Be$	$R\bar{3}c$	this work
	$K_2ZrCl_6 \cdot Zr_6Cl_{12}H$	$R\bar{3}$	22,42
	$CsLuNb_6Cl_{18}$	$P\bar{3}1c$	43
$[Zr_6Cl^i_{12}Z]Cl^a_4Cl^{a-a}_{2/2}$	$Ba_2Zr_6Cl_{17}B$	I4/m	38, this work
$[Zr_6Cl^i_{12}Z]Cl^a_2Cl^{a-a}_{4/2}$	$Na_4Zr_6Cl_{16}Be$	Pccn	44
	$Cs_3Zr_6Cl_{16}C$	$P2_1/c$	44
$[Zr_6Cl^i_{12}Z]Cl^{a-a}_{6/2}$	Nb_6F_{15}	Im3m	17
	$Li_2Zr_6Cl_{15}Mn$	Im3m	this work
	$Cs_3(ZrCl_5)Zr_6Cl_{15}Mn$	$R\bar{3}c$	10, this work
	Ta_6Cl_{15}	Ia3d	18
	$K_3Zr_6Cl_{15}Be$	C2/c	45
	$K_2Zr_6Cl_{15}B$	Cccm	45
	$CsNb_6Cl_{15}$	Pmma	46
	$KZr_6Cl_{15}C$	Pmma	47
	$CsKZr_6Cl_{15}C$	Pmma	47
	$KZr_6Cl_{15}Fe$	Cmcm	this work
$[Zr_6Cl^i_{10}Cl^{i-a}_{2/2}Z]Cl^{a-i}_{2/2}Cl^{a-a}_{4/2}$	Nb_6Cl_{14}	Cmca	48
	$CsZr_6I_{14}C$	Cmca	16,24
	$LiZr_6Cl_{14}Mn$	Cmca	this work
$[Zr_6Cl^i_{10}Cl^{i-i}_{2/2}Z]Cl^{a-a}_{6/3}$	$Zr_6Cl_{13}Be$	Pnnm	25
	$KZr_6Cl_{13}Be$	Pnnm	25
$[Zr_6Cl^i_6Cl^{i-a}_{6/2}Z]Cl^{a-i}_{6/2}$	$Zr_6I_{12}C$	$R\bar{3}$	16,24

EXPERIMENTAL

Materials

Zirconium powder was prepared via dehydrogenation of zirconium hydride. Reactor grade Zr metal (<500 ppm Hf) was obtained from the Ames Laboratory in the form of cold-rolled sheets (0.3 to 0.5 mm thickness). The metal Zr strips were cleaned with a mixed acid (45% conc. HNO_3, 10% conc. HF, 45% H_2O by volume), rinsed with H_2O, and dried in air. For a typical preparation, 5 g of Zr strips was loaded into a Mo boat placed in a fused silica vessel. The leak-free reaction chamber was filled with one atmosphere of H_2 (Matheson, 99.999%) and heated to 450°C, around which rapid hydrogen uptake started. The temperature was gradually raised to 650°C to speed up the reaction and to assure the diffusion of hydrogen into the bulk of the strips. After the H_2 uptake ceased, the system was cooled to room temperature under hydrogen, and the resulted ZrH_x ($x \sim 1.5$) strips were taken into a glove box and ground with a diamond mortar and pestle until the powder passed through a 100-mesh screen. The ZrH_x powder was reloaded into the Mo boat and carefully degassed by slow heating under dynamic vacuum to 300°C where the hydride decomposition began. The temperature was increased in 50°C steps up to 700°C or until the H_2 release stopped (the vacuum system stayed below discharge of a tesla coil, $P \lesssim 5 \times 10^{-6}$ torr). For easy handling, the sample was slightly sintered at 750°C and cooled down as soon as this temperature was reached. The dehydrided metal was ground under an inert atmosphere into Zr powder that passed through a 100-mesh sieve. The refined lattice parameters based on the Guinier diffraction pattern were within 3σ of the reported values for Zr metal.[49]

Zirconium tetrachloride was synthesized by reacting the elemental Cl_2 with excess Zr metal. The reaction container was a two-arm fused silica vessel. After loading reactor grade Zr strips in the horizontal arm, Cl_2 (Matheson, >99.5%) was condensed into the vertical arm cooled with a trap filled with dry ice and acetone. This apparatus was sealed off under vacuum while the Cl_2 was frozen at liquid N_2 temperature. To provide a feasible Cl_2 pressure, the arm with Cl_2 was kept at -40°C ($CaCl_2$/ice bath) at which temperature the Cl_2 pressure was slightly below 1 atmosphere. Repeated heating of the zirconium chamber with a gas/O_2 torch was necessary in order to remove the $ZrCl_4$ formed on the surface of the metal and to reignite the reaction, even though the reaction itself was exothermic. The crude $ZrCl_4$, usually a light orange color, was vacuum sublimed at least twice at 250°C over Zr metal and through a course-grade frit. Purified $ZrCl_4$ was also obtained through multiple sublimations of a commercial $ZrCl_4$ (Aldrich, reactor grade, >99.5%), which probably contained zirconium oxide or hydroxide impurities since a small amount of a light, cotton-like residue was left behind after the first sublimation. The sublimed $ZrCl_4$ was a white, poorly crystallized phase that did not provide a readable Guinier pattern unless it was annealed at 400 to 500°C in a sealed container. The product was separated into small batches of about 1 g each, sealed in evacuated Pyrex ampoules, and opened in the glove box when necessary.

The sources of the countercations were the corresponding chlorides. The alkali-metal chlorides were vacuum dried and then sublimed. The alkaline-earth metal chlorides were prepared by slow thermal decomposition of the corresponding hydrated salts under dynamic vacuum.

The Guinier diffraction patterns were examined to confirm the desired chlorides were free of hydroxides, oxides, or oxychlorides. The $LaCl_3$ was obtained via the reaction of La_2O_3 with NH_4Cl[50] followed by multiple sublimations of the crude product at 800°C in Ta containers under dynamic vacuum.

Interstitial atoms Be, B, and C were introduced into the syntheses as elements. Beryllium flakes (Pechiney, France) were stored and handled in the air with care. Amorphous B (AESAR, particle size <1 μm) necessary for quantitative syntheses was first degassed at ambient temperature and stored in the glove box. Spectroscopic grade graphite (National Brand, Union Carbide) was employed as the source of carbon. To produce H-centered clusters, $ZrH_{1.7}$ was prepared (as above). The hydride composition was calculated from the amount of Zr and the H_2 pressure change at room temperature in a known volume. $ZrD_{1.2}$ was synthesized through a similar procedure, except the Zr/D ratio was determined by the weight gain (0.104 g for 4.000 g Zr) of the sample after the deuteration.

Metal chlorides that provided centered transition-metal atoms were prepared via dehydration by either refluxing the corresponding hydrated salts ($MnCl_2 \cdot 4H_2O$, Baker analyzed reagent; $CoCl_2 \cdot 6H_2O$, Baker & Adamson, reagent grade) with $SOCl_2$, or by slow heating the starting compounds ($FeCl_3$, ROC/RIC, 99%; $NiCl_2 \cdot 6H_2O$, Mallinckrodt, analytical reagent) under dynamic vacuum. The resultant anhydrous materials were sublimed under static vacuum in sealed silica ampoules with narrow necks that separated the crude chlorides from the sublimed products. An iron powder (Baker,

analyzed reagent) was also used as a supplement in several reactions without causing noticeable differences in products or yields.

Synthetic Techniques

The search for new centered zirconium chloride clusters began with syntheses, the goal of which was to provide not only interesting compounds but also supporting evidence for the ultimate structural characterizations. To achieve this goal, special care was taken in the synthesis processes.

One major complication in the syntheses is the sensitivity to O_2 and H_2O of both the reactants and products. During the past twenty years, a great deal of knowledge and experience has been accumulated in overcoming similar problems while investigating numerous reduced halide systems of the early transition metals.[51,52] Several practical techniques have been developed to keep the starting materials as well as products in environments that give minimum contamination from H_2O and O_2, for example, storing the materials in evacuated, sealed ampoules, and handling them only under an inert atmosphere in a glove box. These effective means were adapted to the research on the Zr–Cl systems. In addition, the advancement of the glove box technology has greatly improved the quality of the inert atmosphere in a box, and the storage of rather sensitive reagents including Zr powder and $ZrCl_4$ in stoppered vials in a glove box for reasonable periods (up to two months) has become acceptable. Typically, the glove box (VAC, HE-493) provided a N_2 atmosphere that had a combined moisture and O_2 contamination far below 1 ppm (an operating light bulb with a 20 watt filament lasted for over 20 days). To secure their qualities, all the reagents were saved in capped

vials inside tightly closed Mason jars, while large quantities of hypersensitive substances like $ZrCl_4$ and Zr powder were still stored in sealed ampoules until they were needed, protected against possible accidental damage to the glove box system such as from holes in the gloves.

Another troublesome feature unique to the centered cluster chemistry is the difficulty in identifying or confirming the presence of an interstitial atom. Because of the limited analytical methods available for small main-group elements (H, Be, B, C, N) in centered Zr–Cl clusters, the identification of an interstitial atom depends to a large extent on the possible sources of centering atoms and the yields of the phases of interest. Although it is relatively straightforward to locate a centered transition metal atom in a cluster by X-ray diffraction, problems of adventitious impurities could not be ignored either since the formation of possible side products would complicate or at least slow down the characterization process. In addition, caution should be taken in assigning a centered atom for it is practically impossible to distinguish elements with close atomic numbers by X-ray analysis. Therefore, special care was given at all stages of the syntheses to avoid impurity sources, such as residue H in a metal powder, H_2O, and hydrocarbons. "Quick-and-dirty" operations are not recommended.

The third important aspect of Zr–Cl cluster syntheses is the selection of a proper container material. It was observed in the previous research that the reduced halides of early transition metals as well as rare-earth metals attacked Pyrex and fused silica, the common

container materials, at temperatures near and above 600°C required to form clusters. During the course of the past 15 years, a solution to this problem has been developed by employing welded Nb or Ta tubes as containers. For Zr-Cl systems, Ta was selected as the better container material. This has been shown by SEM analysis to be inert to the reactants and products under the chosen reaction conditions. Furthermore, the distinctive difference in the atomic numbers of Zr and Ta would make the characterization simpler under the circumstance that Ta did take part in the cluster formation, although this has not yet been observed. For a representative reaction, a piece of 3/8" dia. Ta tubing of 4-cm length was treated with Ta cleaning solution (55% conc. H_2SO_4, 25% conc. HNO_3, 20% conc. HF by volume), thoroughly rinsed with H_2O, and dried in the air. One end of the tube was crimped and Heliarc welded.[53] This tube usually was not further treated prior to use. However, if an additional cleaning was required and the mixed acid was used, this must be followed by an extensive rinsing with H_2O to avoid contamination from O, N, C, or even S in the solution.

Starting materials designed to prepare 150 mg of a hypothetical target phase were loaded into a Ta tube in the glove box with the above precautions. Necessary protection was taken to keep the open end of the tube clean, since vaporization or decomposition of small amounts of starting materials near the end of the container might generate holes during the welding. The tube was then closed shut in the box, and transferred to the welder in a air-tight container as soon as possible. After the second end was welded, the Ta tube was placed in a fused silica jacket so that the Ta would be protected from oxidation by air

during the reaction. The inside of the fused silica jacket carrying the Ta tube was cleaned with Ta cleaning solution, carefully rinsed, dried, degassed with a gas/O_2 torch under dynamic vacuum ($P < 5 \times 10^{-6}$ torr), and then sealed off. The reaction thus loaded was usually heated at 800° to 850°C for 20 to 30 days and quenched in the air afterward. To enhance crystal growth, special heat treatments such as slow cooling, temperature gradients, or cycling between two temperatures could be applied. For the same purpose, a chemical that could serve as a mineralizer, flux, or vapor transport agent could also be selected and added into the reaction system.

All the reactions were opened in a glove box under a N_2 atmosphere. The products were visually inspected, samples for powder patterns loaded, and crystals mounted. The materials left after these samplings were sealed in evacuated Pyrex ampoules.

Characterization Methods

Visual inspection

Careful visual inspections were conducted after the reaction containers were opened in a second glove box equipped with a nearly horizontal window and a microscope. Based on the colors and the morphologies of the products, these examinations were used to estimate the numbers and relative yields of products from multiphase reactions. Some of the side products, such as ZrCl or $ZrClO_x$ ($x<1$), could be identified exclusively by their appearances, and this simplified the characterization process. The yields were estimated on the basis of the volume of each product since the physical separation of powdered

products mixed together was very difficult, and other more accurate methods were not accessible. The information obtained through visual inspections was valuable in evaluating each reaction and suggesting further actions toward final characterization of an interesting product, although its reliability was limited, especially when different phases appeared similar so that the estimation of the yields was not possible.

Powder X-ray diffraction

Following visual inspections, the reaction products were further screened by Guinier powder diffraction. This was the primary characterization method that provided more objective, reliable, and semiquantitative identification of the products. Information regarding the numbers, identities, and yields of products can be so obtained. In addition, the lattice constants of each may be calculated if necessary.

Samples were mounted between two pieces of Scotch tape together with a small amount of Si powder as an internal standard (NBS, SRM-64). When necessary, nonwater-based tape was used to avoid the decomposition of a sample in contact with the emulsion. Frequently, more than one sample was prepared from a multiphase product, so that the complexity of powder patterns would be greatly reduced. If several phases did appear on the same pattern, the relative yields could also be estimated based on the number and intensities of reflections from each phase.

The Guinier powder patterns were collected with a ENRAF NONIUS (FR552) diffractometer equipped with an evacuable sample chamber. The incident radiation was Cu $K_{\alpha 1}$ (λ=1.54056 Å) and the 2θ range of the recorded pattern on the film was from 2 to 85°, allowing the display of the first five Si lines.

Powder patterns were first compared against the calculated patterns of known phases generated by program POWDER (version 5)[54] to eliminate starting materials as well as any unimportant side products from further investigation. Whenever a new compound was discovered, the powder pattern was read on an Enraf Nonius Guinier viewer with 0.005 mm precision. These values were then converted into 2θ values by GUIN[55] using a quadratic equation derived from the positions of the standard Si lines. If the structure type of the new compound was recognized, the reflections were manually indexed and cell parameters were refined with LATT99.[56] When the pattern was unknown, the program TREOR (version 4)[57] was employed to obtain the lattice system and cell dimensions if possible. The indexing of an unknown powder pattern by TREOR was often tried but with limited success, mainly because the powder patterns seldom contained the reflections from only one phase.

Single crystal X-ray diffraction

The success in this research can be attributed to a large extent to the effective structural characterizations by single crystal X-ray analyses. It was the only accessible method to identify a new phase in an unknown structure. In addition, it was used to determine or confirm the stoichiometry of new compounds, which was essential in understanding the structure and bonding features of the cluster phases.

Crystals, usually with well defined facets, were selected and mounted in the glove box with vacuum grease (APIEZON L) into thin-walled capillaries (0.2, 0.3 mm dia). Oscillation photos were taken on a Weissenberg camera to evaluate the quality of the crystals and to select

the most suitable ones for further study. Sometimes, Weissenberg or precession photos were also taken for additional information.

The majority of the data sets were collected at room temperature on either an ENRAF NONIUS CAD4 diffractometer or a RIGAKU AFC6R diffractometer. Both are automated diffractometers with Mo K_α radiation (λ=0.7017 Å) and monochromaters in the incident beam. The beam intensity of the latter instrument was stronger because the X-ray tube has a rotating anode (12 KW). The software packages enabled convenient routine examinations prior to data collection and allowed searching, refining, and indexing of reflections, determination of the orientation matrix, and reduction of the cell. Axial photos were taken, first to assure the quality of the crystals, and second, to confirm the lattice parameters and symmetries determined by the preliminary analyses. Based on the information from these photos, lattice types and Laue symmetries were determined, and data collection parameters were carefully selected. Following the data collections, ψ-scans were measured at least on three intense reflections with χ close to 90° for empirical absorption corrections.

The complete data sets, generally containing redundant data, were inspected to confirm the Laue class and to determine the space group if possible. The data processing included Lorentz-polarization correction, decay corrections with standard reflections when necessary, and an empirical absorption correction using ψ-scans. The observed data, defined by $I/\sigma_I>3$; $F/\sigma_F>6$, thus prepared were then averaged in the proper Laue group, and a reduced data file was created for further structure determination and refinement.

The initial models were obtained either from isostructural parent compounds or by direct methods in SHELXS-86.[58] The structure refinements were carried out with least-squares full matrix calculations and standard Fourier syntheses using the programs in the structure determination software packages, namely SDP[59] or TEXSAN[60] which were furnished with CAD4 or RIGAKU, respectively. The structure factors were calculated using neutral atomic scattering factors with corrections for both the real and imaginary parts of anomalous dispersion for heavier elements (Z>10).[61] Atoms were located, and their positional parameters, isotropic thermal parameters, and anisotropic thermal parameters were refined successively. At the later stage of the refinements, the secondary extinction coefficient was refined. A numerical absorption correction (DIFABS)[62] could be applied based on a model with isotropical thermal parameters if the original empirical absorption correction did not appear adequate. Occupancies of certain positions were studied, and final electron difference maps were examined and residue election densities were reported to evaluate the quality of the solution. Part of the important structure refinement parameters listed in the crystal data tables are defined as following:

1) Linear absorption coefficient μ

$$\mu = \frac{1}{V_c} \sum_i n_i \mu_{ia}$$

where V_c is the unit cell volume and n_i is the number of a given atom in the unit cell. μ_{ia} is the atomic absorption coefficient tabulated in the International Tables.[61]

2) $$R_{ave} = \frac{\sum_{i=1}^{n} \sum_{j=1}^{m} | \langle F_i^2 \rangle - F_{ij}^2 |}{\sum_{i=1}^{n} m \langle F_i^2 \rangle}$$

for all observed reflections ($I > 3\sigma_I$), where n is the number of unique reflections that are observed more than once and m is the number of times a given reflection is observed. $\langle F_i^2 \rangle$ is the average value of F^2 for unique reflection i.

3) Secondary extinction coefficient g[63]

$$F_{c(corr)} = \frac{F_c}{1 + g F_c^2 \cdot Lp}$$

where Lp is the Lorentz-polarization factor.

4) $$R = \frac{\Sigma | |F_o| - |F_c| |}{\Sigma |F_o|}$$

$$R_w = \left[\frac{\Sigma w(|F_o| - |F_c|)^2}{\Sigma w F_o^2}\right]^{1/2}$$

for refinement on F where $w = \frac{1}{\sigma_F^2}$.

In a few cases, the data were collected on a SYNTEX $P2_1$ or a DATEX diffractometer and the structures were solved with methods and programs previously described.[37]

For a completed structure solution, positional and thermal parameters were reported with standard deviations. The anisotropic thermal parameters, B_{ij}'s, are defined by $T = \exp[(-1/4\ (B_{11}h^2a^{*2} + B_{22}k^2b^{*2} + B_{33}\ell^2c^{*2} + 2B_{12}hka^*b^* + 2B_{13}h\ell a^*c^* + 2B_{23}k\ell b^*c^*)]$. Important interatomic distances were calculated with the lattice constants provided by powder diffraction, which are considered to be more accurate because of the calibration with the Si standard and the larger number of observations utilized. Structures and their interesting fragments were revealed by drawings generated with the ORTEP program.[64]

Specific details of individual structure determination processes and structure solutions will be presented under each compound.

^{7}Li solid state NMR studies

Although X-ray diffraction is a powerful structure determination tool, it should not be considered as the only method to characterize new phases. One of its limitations, namely the poor sensitivity toward light elements, becomes rather obvious in dealing with H or Li. In both cases, solid state NMR was chosen as the alternative to provide additional supporting evidences for structure determinations. Proton solid-state NMR experiments were first conducted on H-centered cluster phases to confirm the presence of the interstitial hydrogen,[65] while ^{7}Li NMR was more recently used in the research on Zr-Cl cluster systems involving Li. Its first advantage is the good availability of the NMR-active isotope ^{7}Li (I = 3/2, natural abundance 92.57%). In addition, the nucleus has a very high sensitivity (for equal numbers of nuclei, 0.294 at constant field, 1.94 at constant frequency with respect to ^{1}H). Its third attractive factor is that it provides information unique to

the solid state, including symmetry of the coordination sphere, and the electron distribution around the Li in question. These NMR studies were used to answer the following questions: 1) Is Li present in the sample? 2) Is Li in the phase of interest, or in LiCl, one of the starting materials? 3) Is it possible to determine, or at least to acquire information on, the symmetry of the Li coordination environment? The first two questions were answered satisfactorily. However, because of the limited examples and experience available, ^{7}Li NMR could not unambiguously determine the symmetry of the Li positions. Yet, combined with results from X-ray analyses, the data could lead to useful conclusions.

The NMR samples were prepared from reactions that produced the phase of interest with estimated yield higher than 95%. Since the instrument available was not designed to handle air sensitive materials, the samples had to be protected with sealed containers. About 40 mg of a sample that appeared to be free of impurities under the microscope was loaded to a piece of Pyrex tubing (0.7 cm O. D.) that had one end sealed. The open end was plugged with grease before it was brought out of the box. The tube was sealed using a small gas/O_2 torch, with care taken to minimize overheating that might cause decomposition of the sample. The resultant glass bulb with a drop shape fit into an NMR rotor (1.0 cm I. D., 1.5 cm tall).

The NMR spectra were collected by Vinko Rutar at I.S.U. Instrument Service Center on a BRUKER WM-200 NMR spectrometer. Information was obtained from both room temperature and low temperature experiments. Because the samples could not be packed directly into the rotor, the

delicate balance required for high speed rotation could not be achieved, and hence the spinning function of the instrument was practically disabled. The signals shown on the static spectra are generally broader, an intrinsic feature of the method resulting from the random distributions of the nuclei in a powder sample. With this limitation, the NMR studies still provided interesting information, such as chemical shift δ, quadrupole coupling constant Q_c, asymmetry parameter η and peak profiles. The interpretations of these results were made in combination with X-ray structure analyses and will be given in the discussion section.

RESULTS AND DISCUSSION

The results of structure characterizations of new cluster compounds will be presented in the order of the increasing Zr/Cl ratio. Under each given Zr/Cl ratio, cluster examples are further divided into groups according to their structure types and stoichiometries.

Because of technical difficulties and limited access, the stoichiometries of the phases under study were established without chemical analyses. However, the validity of these results was first supported by controlled, high yield syntheses and, secondly, confirmed by X-ray analysis on both powder and single crystal samples. An empirical formula obtained through a single crystal X-ray was evaluated from crystallographic point of view by examining factors such as the occupancies, the residue peaks, ΔF's, the standard deviations and the correlation between multiplicities and thermal parameters. More important, its chemical meaning was also pursued by taking the cluster electron counts into consideration, and by comparing the distances with the corresponding crystal radii.[66]

In addition, other experiments such as solid state NMR studies, magnetic susceptibility measurements and SEM analysis were also employed to provide supporting evidences if necessary. The results of these efforts in structure determinations will be presented, and the chemical and structural meaning the models thus established will be discussed. Whenever possible, these materials will be organized into relatively independent packages under each compound or a group of compounds in question.

Zr_6Cl_{18} Type

The Zr-Cl cluster compounds are composed of discrete $Zr_6Cl^i_{12}Z$ Cl^i = edge-bridging Cl units with the monochloride as the only exception. Although they are often referred as M_6X_{12} type of clusters, the additional terminal Cl^a atoms are indispensable for cluster formation and stabilization.[67] In fact, the structure diversity in these systems is largely because of the functional varieties of the exo-chlorines. Among these structure series, the $[Zr_6Cl_{12}{}^iZ]Cl_6{}^a$ phases can be considered as the simplest ones with isolated cluster units that are the basic building blocks for constructing cluster phases with higher complexities.

The first examples of M_6X_{18} clusters were $K_4Nb_6Cl_{18}$[41] and $Ba_2Nb_6Cl_{18}$[68-70] that were discovered in the early days of metal cluster chemistry. Excluding a group of Nb_6Cl_{18} phases with organic s countercations studied in the early 70s,[71-72] the next structure type in this family was the well known double salt $M_2ZrCl_6 \cdot Zr_6Cl_{12}(H)$ (M = Na - Cs)[22] synthesized via solid state reactions. More recently, a series of ternary or quaternary Nb_6Cl_{18} cluster phases containing rare-earth metal counter cations have been characterized[73] which have either the above double salt structure or that of $CsLuNb_6Cl_{18}$,[43] a modified double salt structure that can be considered as a superstructure of $Ba_2Nb_6Cl_{18}$. Meantime, a new M_6X_{18} structure, namely, $Rb_5Zr_6Cl_{18}B$ was uncovered.[40] Yet, only one of the above four niobium types had Zr-Cl cluster examples, whereas the extensive research that has led to a rich structural chemistry of the Zr-Cl cluster systems is marked by up to 12 structure types.[26] By purposely increasing the Cl/Zr ratio as well as

introducing rare-earth or alkaline-earth metal countercations into the syntheses, the number of $Zr_6Cl_{18}Z$ structure types has been increased to six, including two new ones ($Li_6Zr_6Cl_{18}H$, $Ba_3Zr_6Cl_{18}Be$), and four known types ($M_2Zr_7Cl_{18}(H)$, $K_4Nb_6Cl_{18}$, $CsLuNb_6Cl_{18}$, $Rb_5Zr_6Cl_{18}B$). Besides the structure diversity, the $Zr_6Cl_{18}Z$ family is also rich in chemical components, including a variety of countercations and both main-group and transition metal element centering atoms. Having similar cluster units but different packing arrangements, these new compounds serve as good examples to demonstrate the effects of charge, number, and size of countercations on the structure of solid state cluster phases. In addition, with isolated cluster units, some of these compounds are suitable candidates for the solution cluster chemistry.

$\underline{Li_6Zr_6Cl_{18}H}$[39]

$Li_6Zr_6Cl_{18}H$ is the third known example of Zr-Cl clusters stabilized by an interstitial hydrogen. The other two compounds in this series, namely, $Zr_6Cl_{12}H$ and $M_2Zr_7Cl_{18}(H)$ (M = alkali metals),[22] were among the first few cluster phases discovered in the Zr-Cl systems, and in both cases, the interstitial H was initially involved in the syntheses as an adventitious element. The correct chemical compositions of these two compounds were later confirmed by improved high yield syntheses achieved with sufficient hydrogen, and also by solid state ^1H NMR studies on $Zr_6Cl_{12}H$.[65] The importance of the hydrogen atom in cluster stabilization was further rationalized in terms of molecular orbitals established for centered clusters through extended Hückel calculations.[24,37] It is believed that the electron shared by the H atom plays a key role in stabilizing these two types of H-centered clusters, both with cluster

electron count of 13. With an advanced understanding of the electron and bonding features of the cluster compounds, efforts were made to synthesize new hydride clusters with new structures and probably with 14 cluster electron count, the optimal value for clusters centered by main-group element. As a result, $Li_6Zr_6Cl_{18}H$ with a new structure type was discovered. Interestingly, it is again a 13-electron cluster, and therefore has similar bonding features as the other two hydride clusters. Yet, the new chemical component Li and the new stoichiometry provide interesting structural characteristics. As with all M_6X_{18} clusters, there is no direct cluster connection, contrary to what is observed in $Zr_6Cl_{12}H$[74] ($Zr_6I_{12}C$ type). In addition, the lack of strong interactions between clusters combines with the countercations to make the packing of the clusters the dominate factor in determining the three dimensional structure of $Li_6Zr_6Cl_{18}H$. It has proved to be a suitable candidate for solution chemistry. Furthermore, because of its large Li content, it is an ideal compound for ^7Li solid state NMR studies.

Synthesis $Li_6Zr_6Cl_{18}H$ was first discovered from a reaction with a loaded stoichiometry of $LiZr_6Cl_{12}H_{1.8}$. Assuming that the excess hydrogen would diffuse through the Ta container, the target compound was $LiZr_6Cl_{12}H$, a 14-electron cluster phase with a structure possibly related to $Zr_6I_{12}C$[16,24] or $Sc_7Cl_{12}C$.[15] After being heated at 700°C for two weeks, the reaction produced a black powder and several dark crystals. The powder diffraction pattern showed that the product contained approximately equal amounts of $Zr_6Cl_{12}H$, the new hydride $Li_6Zr_6Cl_{18}H$, ZrO_xCl, and at least one other phase that still remains unidentified. Following the structural characterization by the single crystal X-ray

analysis, $Li_6Zr_6Cl_{18}H$ was prepared in high yield (>90%) from reactions with the revised stoichiometry, accompanied by a small amount of ZrCl and $ZrCl_4$. No significant changes in the cell parameters were observed when the Li and H contents in the starting materials were varied, indicating that $Li_6Zr_6Cl_{18}H$ is a line compound. An attempt to increase the Li/Zr ratio to 7/6 to synthesize a 14-electron cluster was unsuccessful. Moreover, partial or complete substitution of Li with Na or replacement of H with Be also failed, producing 50% of an unknown phase in the former case and $LiZr_6Cl_{14}Be$ in the latter case.

Large quantities of $Li_6Zr_6Cl_{18}H$ and $Li_6Zr_6Cl_{18}D$ were prepared for vibration spectral studies by inelastic neutron scattering. The reactions were loaded in welded Ta tubes with diameters of 1.5 cm and lengths of 8 cm, each containing up to 1.8 g of the starting materials. The reactions were slowly heated to 700°C in a week and maintained at this temperature for over 4 weeks. The Ta tubes were usually slightly bulged after the reaction, indicating substantial pressure over the reaction system under the chosen conditions. The estimated yield of the products were at least 90%, and the major impurity was ZrO_xCl which seems to always coexist with the desired product, similar to what was observed for the $Zr_6Cl_{12}H$ system.[42]

Structure determination The single crystal used for X-ray analysis was selected from the reaction loaded with stoichiometry of $LiZr_6Cl_{12}H_{1.8}$. One quadrant of data ($hk\ell$, $\bar{h}k\ell$) was collected on a SYNTEX diffractometer (Table 2). The data were corrected for absorption using one ψ-scan and averaged for space group $R\bar{3}$ which was selected based on the information from axial photos and diffraction conditions. The Zr

Table 2. Crystal Data for $Li_6Zr_6Cl_{18}H$

space group	$R\bar{3}$ (No. 148)
Z	3
a, Å[a]	15.969(1)
c, Å	8.883(1)
V, Å^3	1961.7(4)
crystal dimens, mm	0.20 x 0.20 x 0.25
data collection instrument	SYNTEX $P2_1$
scan mode	ω–2θ
$2\theta_{max}$, deg	55
reflections	h, k, $\pm\ell$
measured	1656
observed	1346
independent	839
absorp coeff μ, cm^{-1}	41.3
range of transm coeff	0.93-1.00
R_{ave}, %	1.5
second ext coeff	$0.53(5) \times 10^{-4}$
R, %	2.2
R_w, %	2.5
largest residue peak, e$^-$/Å^3	0.5

[a]Guinier powder diffraction data (38 observations).

atom was located by analyzing the Patterson map. After refinement (R=33%), the calculated electron density map revealed three sets of peaks each with one-third of the electron density of the Zr, and hence they were assigned to Cl atoms. Following refinement of the positional parameters and the isotropic temperature factors (R=7%), the thermal parameters of the first four atoms were refined anisotropically. The extinction coefficient was also refined (R=3.5%, R_w=4.6%). A difference Fourier map was calculated, and the peaks associated with about 2 $e^-/Å^3$ were assigned to Li atoms. After the refinement of Li was completed isotropically with full occupancy, the R and the R_w reached 2.2% and 2.6%, respectively. The occupancy of the Li position refined to 84(3)% accompanied by a decrease in its isotropic thermal parameter from 3.7(2) to 2.6(3), but the agreement factors did not change significantly (R = 2.2%, R_w = 2.5%). The validity of this result was in question as the Li atoms are required to stabilize the cluster by providing electrons and the experiments showed that $Li_6Zr_6Cl_{18}H$ is a line compound. The Li at full occupancy could also be refined anisotropically (R = 2.2%, R_w = 2.5%); however, since the three principal B's were essentially the same (B_{11} = 3.5(6), B_{22} = 2.9(5), B_{33} = 2.5(5), B_{12} = 1.6(4), B_{13} = 0.2(4), B_{23} = 0.1(4)), this result was not significant. As expected, the H atom could not be located due to its poor X-ray diffraction power. The final difference map was essentially flat, and no residue bigger than 0.5 e/A^{-3} was found. The atom positions and temperature factors resulted from the isotropic refinement of the fully occupied Li atoms and anisotropic refinement of the Zr and Cl atoms are listed in Table 3.

Table 3. Positional and Thermal Parameters for $Li_6Zr_6Cl_{18}H$

	x	y	z	B_{11}
Zr	0.10662(2)	0.12293(2)	0.14606(3)	1.05(1)
Cl1	0.10153(6)	0.25834(6)	0.00089(9)	1.83(3)
Cl2	0.52716(6)	0.31435(6)	0.00273(9)	1.83(3)
Cl3	0.43807(6)	0.06773(6)	0.00322(9)	1.63(3)
Li	0.0586(6)	0.4932(6)	0.160(1)	–

B_{22}	B_{33}	B_{12}	B_{13}	B_{23}	B_{eq}
1.03(1)	0.86(1)	0.556(9)	0.047(9)	0.048(9)	0.89(1)
0.98(3)	1.50(3)	0.59(2)	-0.46(3)	-0.07(3)	1.34(3)
1.27(3)	1.25(3)	0.72(3)	-0.55(3)	-0.06(2)	1.33(4)
1.36(3)	1.57(3)	0.63(3)	-0.34(3)	-0.24(3)	1.41(4)
–	–	–	–	–	3.7(3)

Important distances calculated with lattice parameters provided by an powder X-ray diffraction study are reported in Table 4.

Structure descriptions $Li_6Zr_6Cl_{18}H$ consists of two structural elements, namely, the $[Zr_6Cl_{18}H]^{6-}$ cluster and the countercation Li^+ (Figure 1). The metal core of the cluster has comparable dimensions to the other two known 13-electron, H-centered chloride cluster compounds.[22,42] The trigonal compression indicated by the 0.01 Å difference in the two Zr-Zr distances is only about a quarter of what was observed for another 13-electron cluster, the double salt $K_2Zr_7Cl_{18}(H)$, implying that this type of distortion is a combined result of the electronic factor and matrix effects. Notice that the interaction between the countercation Zr and Cl^a in the double salt is so strong that the Cl^a's are pulled away from the cluster and toward the countercation (Zr–Cl^a, 2.474 Å vs 2.770 Å), forming a $ZrCl_6^{2-}$ group. In contrast, the electrical field around Li in $Li_6Zr_6Cl_{18}H$ is weaker and it is responsible for the less severe distortion of the cluster core in $Li_6Zr_6Cl_{18}H$. The Zr to Cl^a distance, which is almost 0.1 Å shorter than the corresponding one in the double salt, is accounted for by the same effect.

The Li atom sits on a general position and is surrounded by three cluster units, each contributing one Cl^i and one Cl^a (Figure 2). The six Li-Cl distances, ranging from 2.430(9) Å to 2.804(9) Å, have an average of 2.595 Å, slightly larger than the summation of the crystal radii[66] of Li^+ (CN=6, 0.90 Å) and Cl^- (1.67 Å). The wide range of distances shows that the coordination polyhedron of Li is highly distorted, implying Li is a less predominant structural element in this

Table 4. Important Distances (Å) in $Li_6Zr_6Cl_{18}H$

Zr-Zr		x6	3.1975(8)
		x6	3.1856(7)
	$\bar{d}$		3.1916
Zr-Cl^i	Zr–Cl1	x6	2.5532(9)
		x6	2.560(1)
	Zr-Cl2	x6	2.5671(9)
		x6	2.576(1)
	$\bar{d}$		2.564
Zr-Cl^a	Zr–Cl3	x6	2.687(1)
Li–Cl	Li-Cl1	x1	2.605(9)
	Li-Cl2	x1	2.430(9)
		x1	2.500(9)
		x1	2.563(9)
	Li-Cl3	x1	2.669(9)
		x1	2.804(9)
	$\bar{d}$		2.595

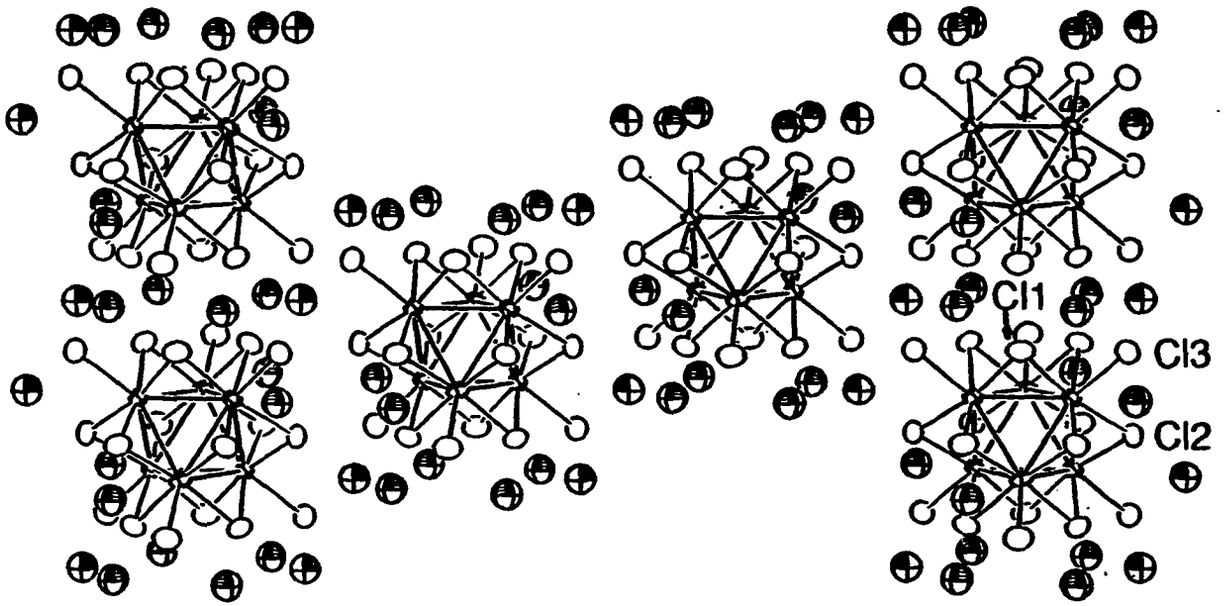

Figure 1. The [110] projection of $Li_6Zr_6Cl_8H$ (90% probability) with the $\bar{c}$ axis vertical. The H atom occupies the center of cluster (point symmetry S_6), and the shaded spheres around the cluster represent the Li atoms

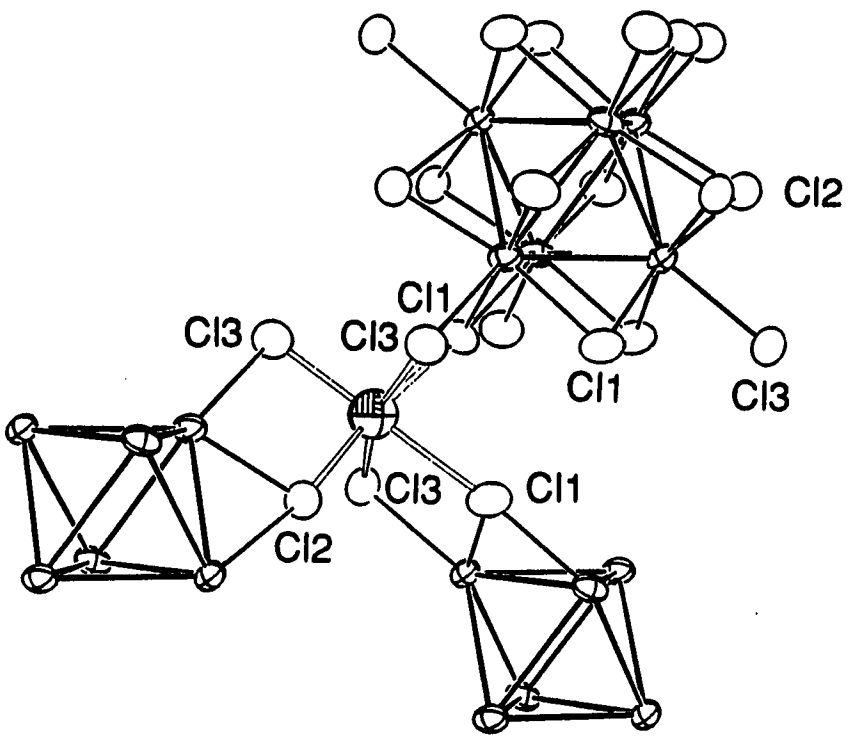

Figure 2. The coordination environment of the Li ion in $Li_6Zr_6Cl_{18}H$ (90% probability)

phase, and its relatively weak field as well as small size allow or even favor this distortion. The large range of the Li–Cl distances is also the direct reflection of the coordination environment of each individual Cl. For instance, the terminal Cl^a (Cl3, CN = 1(Zr) + 2(Li)) has the shortest Li-Cl distances, and among the two inner chlorines (Cl1, CN = 2(Zr) + 1(Li); Cl2, CN = 2(Zr) + 2(Li)), Cl2 with higher total coordination number has the longer Li-Cl distances. Although the occupancy of the Li position refined to 84(3)%, it is reasonable to believe that this position is fully occupied because of the electron deficient nature of the cluster unit and the fact that a preparation with 20% Li deficiency yielded ZrCl, $ZrCl_4$ and the cluster phase with essentially the same cell parameters as those from a reaction loaded to make $Li_6Zr_6Cl_{18}H$.

Since the dominant interactions between Li^+ and other structure components are ionic in nature, the Li atom tends to settle in an environment with the fewest cationic second neighbors around its coordination polyhedron. The position that Li occupies has 3 Zr and 3 Li nearest neighbors (Li–Zr: 3.73 Å, 3.95 Å, 3.99 Å; Li–Li: 3.47 Å, 3.84 Å, 3.84 Å). The other two sets of vacancies with the same chlorine coordination number have either 4 Zr and 7 Li (general position, multiplicity 6; Li–Zr: 3.24 Å to 4.38 Å, Li–Li: 3.25 Å to 3.98 Å) or 6 Zr and 6 Li ($\bar{3}$ at (0,0,1/2), multiplicity 1; Li–Zr: 3.65 Å; Li–Li: 3.84 Å) around them, and the energy cost of filling these positions restricts the upper limit of Li content in this phase. Therefore, the cluster electron count deviates away from the optimum value of 14 to 13. A similar argument may be applied to the other solid state 13-electron

hydride clusters. Besides the cluster electron count, these structural limitations, including geometry, packing, and ionic interaction imposed on the solid state materials, are important factors that determine whether a phase is stable. It is only when a balance among these factors is achieved that a phase may be obtained from high temperature solid state reactions.

The unsuccessful substitution of Li by Na may be explained by the size of the cation position. Since the Li atoms occupy the six-coordinate positions between Cl layers as the Zr atoms and have similar radii, replacing them with larger cations Na (CN = 6, 1.16 Å) leads to the expansion and distortion of the Cl layers, which in turn may destabilize the cluster units as well as the entire structure.

The three-dimensional structure of $Li_6Zr_6Cl_{18}H$ is related to that of $Zr_6I_{12}C$ in the sense that they both have a cubic close packed Cl sublattice (•••ABC••• or $(c)_3$) and a cubic close packed cluster array. However, as the number of Cl increases to 18 per cluster in the lithium-hydride compound, the shared Cl^{i-a} atoms in $Zr_6I_{12}C$ are replaced by terminal Cl^a atoms. The cluster units become isolated and farther apart from each other as the bonds pulling them closer to each other no longer exist. This causes an expansion of the a and b axes while the stacking of the close packed layers along c axis remains unchanged. The negatively charged cluster units are held together by Li atoms, and for each cluster there are 12 Li atoms above and below it, and six additional ones around its waist between the same layers of Cl atoms as the Zr atoms (Figure 1). Even though these cations are symmetry related in the structure, when each individual cluster is concerned, the lithium

atoms around the waist are closer to the cluster than those at its top and bottom. The entire structure may be described as close packed $Zr_6Cl_{18}H$ clusters with a Li-sheath around them. It also may be viewed as close packed Cl atoms with part of the pseudo octahedral holes selectively filled by either Zr or Li atoms.

Solid state ^1H NMR study Since the interstitial H atom in $Li_6Zr_6Cl_{18}H$ cannot be located with X-ray diffraction analysis, ^1H solid state NMR was employed to confirm its presence in the cluster phase. The experiment was conducted on a sample of about 50 mg sealed in Pyrex tubing. The spectrum collected at room temperature by Lucy Flanagan showed a broad and weak signal at around -400 ppm with respect to water, which is characteristic of a proton in a paramagnetic environment inside a metal cage based on the previous ^1H NMR studies on $Zr_6Cl_{12}H$[65] (~-500 ppm). This shows that instead of being empty, the cluster is stabilized by a H atom.

Solid state ^7Li NMR study Although the single crystal X-ray analysis succeeded in locating and refining the Li atom, confirmation of the results seemed necessary because of the limited scattering of X-rays by a light atom such as Li. In addition, the other objective of this experiment was to accumulate experience in solid state ^7Li NMR since no examples of this type could be found in the literature. The room temperature NMR spectrum (Figure 3) of $Li_6Zr_6Cl_{18}H$ showed a signal at +11.8 ppm with respect to LiCl. This chemical shift is the largest observed so far for the Li-containing zirconium chloride cluster phases ($LiZr_6Cl_{14}Mn$, δ = −2.2 ppm; $Li_2Zr_6Cl_{15}Mn$, δ = −0.4 ppm). On one hand, it is difficult to interpret this shift because unpredictable results could

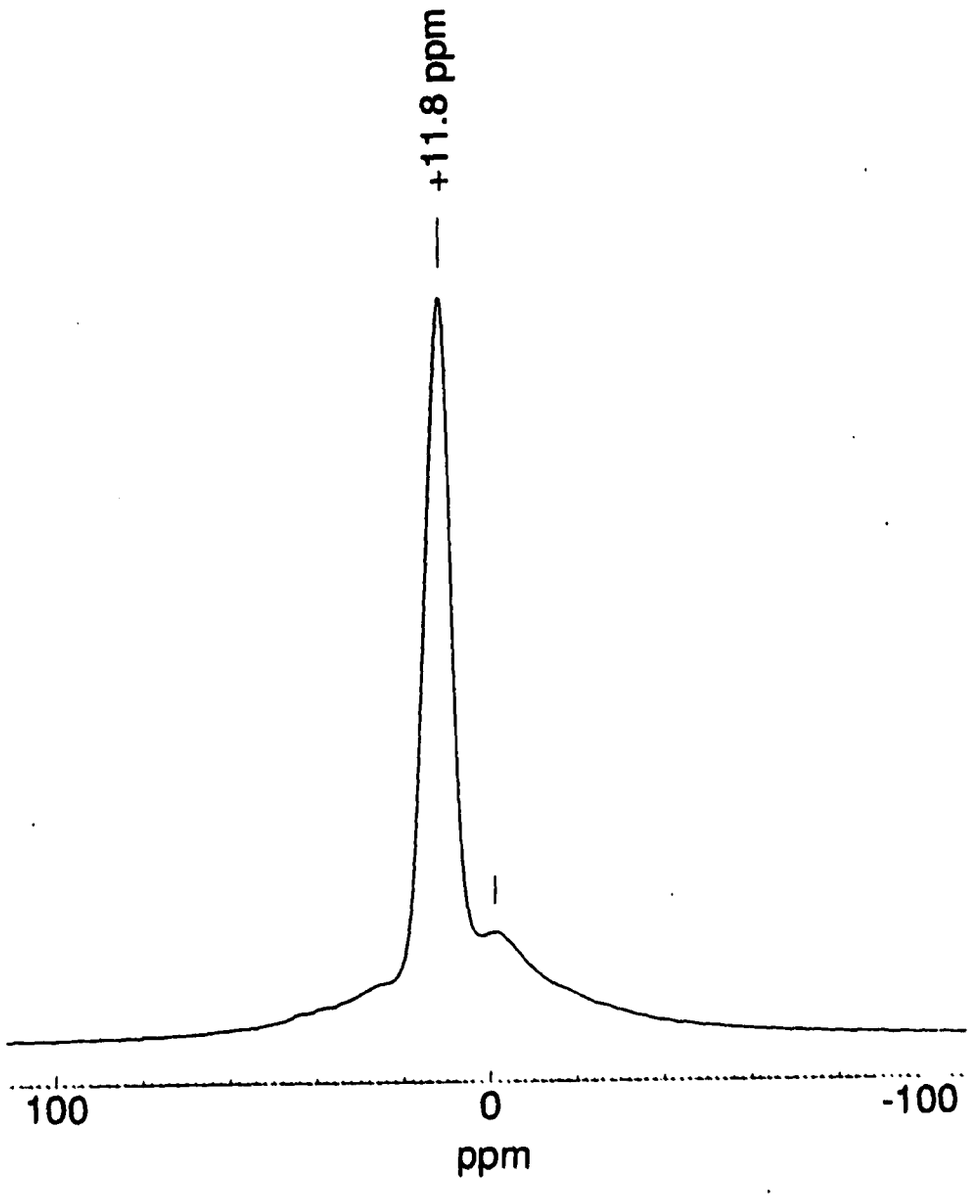

Figure 3. The ^{7}Li solid state NMR spectrum of $Li_6Zr_6Cl_{18}H$

arise from van Vleck (field-induced) paramagnetism. On the other hand, a certain portion of this shift could be associated with a highly exposed nucleus, as the electron deficient cluster core may draw the electrons further away from the Li atoms in this compound than in LiCl where the charge transfer is less complete. The central peak is sharp and narrow (width at half maximum height = 9.5 ppm) and is best described as a Lorentzian peak, in contrast to a Gaussian peak associated with the signal of Li atoms with cubic symmetry that do not experience quadrupole interactions (width at half maximum height = 62 ppm, Figure 4). As the NMR signal from a powder sample should always be symmetrical with respect to the central peak, the small shoulder that appears at about 0 ppm was assigned to Li in LiCl, which could be the result of the incomplete reaction and/or partial decomposition of the sample while it was being sealed in the container.

The lack of detailed features in this spectrum limits the information that can be extracted, and the asymmetry parameter as well as the quadrupole coupling constant remain undetermined. There might be three factors associated with this problem. First, magic angle spinning might sharpen the signals, therefore revealing more details that are hidden under the broad peak. Secondly, samples with improved quality may eliminate the broad peak from LiCl. Finally, this type of peak profile may be intrinsic for Li in a low symmetry environment as in this structure. The latter two are considered to be the dominant factors since well defined profiles of both the center signal and the side bands were observed in a static spectrum of another cluster phase, $Li_2Zr_6Cl_{15}Mn$, as will be presented later.

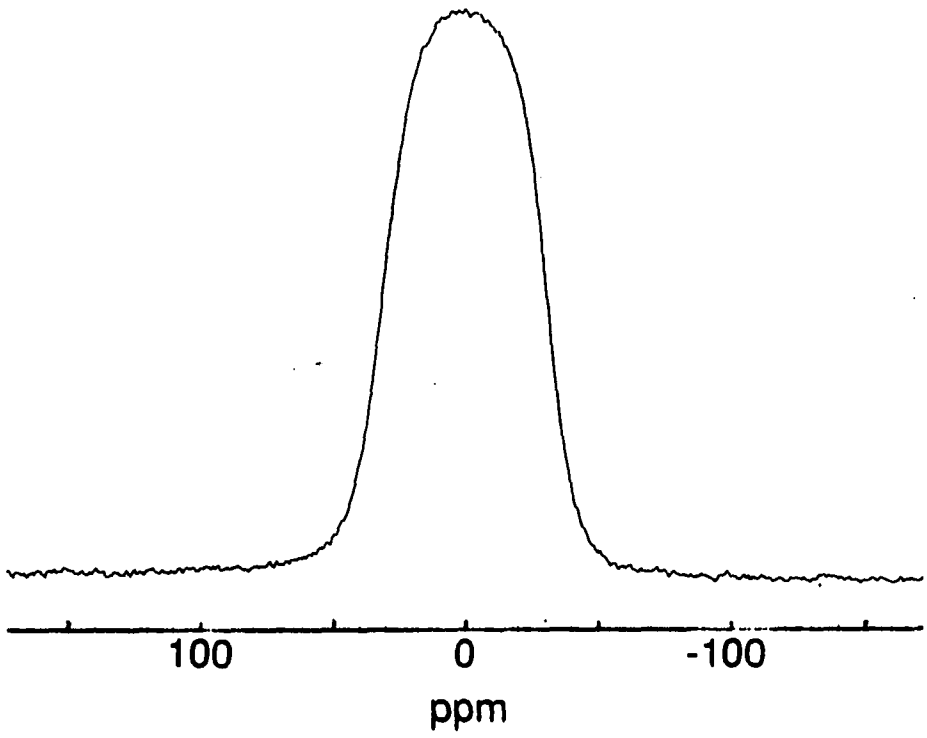

Figure 4. The ^{7}Li solid state NMR spectrum of LiCl (room temperature, static spectrum), which shows a typical Gaussian peak with a half maximum width of 62 ppm

Magnetic susceptibility measurement Based on the stoichiometry deduced from crystal structure determination and NMR studies, $Li_6Zr_6Cl_{18}H$ is a paramagnetic substance with a 13-cluster-electron count. To confirm this, its magnetic susceptibility was measured on a sample of about 50 mg. The magnetic behavior of this compound obeys Curie-Weiss law over a large temperature range, and $1/\chi$ varies with T linearly between 60K and 260K (Figure 5). The slope of this line corresponds to a magnetic moment of 1.1 BM, which is smaller than expected for one unpaired electron and another measurement on $Li_6Zr_6Cl_{18}D$ gave a similar effective moment of 0.96 BM. These values are smaller than what is expected for one localized unpaired electron, and the substantial discrepancy might be the result of spin-orbital coupling. In addition, the possibility of the compounds being Li or H deficient cannot be ruled out. The extrapolation of this line gives a Curie temperature as small as 0.6 K. The deviation of magnetic susceptibility from the ideal Curie-Weiss behavior at higher temperature (>260 K) may be the result of a thermal excitation from ground states to an excited state with a different magnetic character. If this is true, the threshold energy associated with this transition is estimated to be 0.02 eV. Yet, when this assumption is evaluated, the fact that the absolute values of the susceptibilities become very small at higher temperatures, and therefore less accurately known, must also be taken into consideration.

$Rb_4Zr_6Cl_{18}C$ and other compounds with the $K_4Nb_6Cl_{16}$ structure

Although the structure type of $K_4Nb_6Cl_{18}$ has been known since 1968,[41] its zirconium chloride analogues were not established until $Rb_4Zr_6Cl_{18}C$ was characterized. This compound belongs to the M_6Cl_{18} family and contains

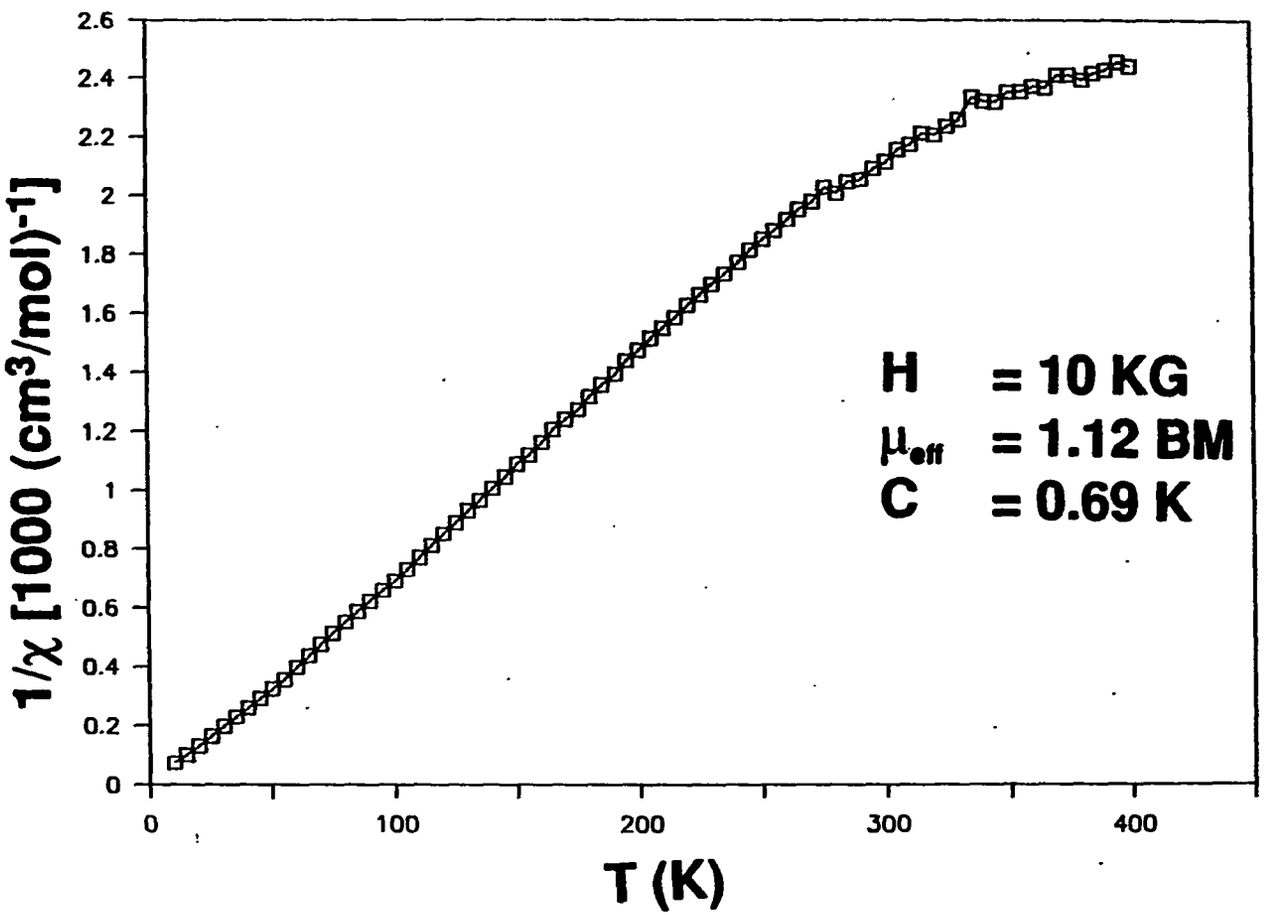

Figure 5. The $1/\chi \sim T$ curve of $Li_6Zr_6Cl_{18}H$ (H = 10 kG)

isolated $[Zr_6Cl_{18}C]^{4-}$ cluster units in a pseudo close packed array. In contrast to the other known $M_xZr_6Cl_{18}Z$ examples, the chlorine atoms do not form close packed layers in $Rb_4Zr_6Cl_{18}C$ owing to the arrangement of the countercations. This is reflected by the low symmetry of both the Rb coordination environment and the lattice, which is unique among the solid state $M_xZr_6Cl_{18}Z$ clusters. The packing of the clusters and countercations also results in the relatively weak binding interactions between slabs of clusters, and this might be the cause of the peculiar crystallization behavior of this phase. In addition, the high content and low charge of the counter cation make it a suitable candidate for solution investigations.

Synthesis $Rb_4Zr_6Cl_{18}C$ was first produced in a well crystallized form via a reaction with a loaded stoichiometry of $Rb_3Zr_6Cl_{15}C$ (600°C to 850°C, 1 day; 850°C, 14 days). The ruby-like crystals obtained from the same reaction were hexagonal prisms. The quantitative synthesis of this compound was not trivial even though the crystal structure determination succeeded without any difficulties. After the compound was characterized with single crystal X-ray analysis, reactions were loaded to reproduce $Rb_4Zr_6Cl_{18}C$. Under the conventional reaction conditions (800-850°C, 14-20 days), the reactions seemed to be complete. The products had a uniform black color and appeared to be crystalline under the microscope. However, it was surprising that the major content(s) was amorphous and most of the powder patterns collected showed only broad lines of Rb_2ZrCl_6 plus a few (<10) less intense reflections from $RbZr_6Cl_{15}C$ (estimated yield <10%). Non-water based mounting tape did not provide better diffraction patterns, which might imply that the problem existed prior to the X-ray sample

preparation. Slow cooling or annealing after the reaction period did not make noticeable differences in the diffraction power of the product. Changing the stoichiometry of the starting materials to $Rb_3Zr_6Cl_{15}C$, as in the original reaction, failed to repeat the expected result. Based on experience, it is believed that the desired product $Rb_4Zr_6Cl_{18}C$ did form during the reaction, since a reaction that fails to produce a target compound usually forms another relatively more stable cluster phase, for example, $RbZr_6Cl_{15}C$, in a reasonable yield (>70%). The difficulty in detecting $Rb_4Zr_6Cl_{18}C$ by its diffraction pattern may be associated with the poor crystallinity of the product, the high reactivity of an amorphous phase, or the possibility that the product decomposed upon cooling to give crystalline Rb_2ZrCl_6 and one or several amorphous, reduced zirconium chloride phases.

The reaction and crystallization mechanisms are not understood. Nonetheless, there was a surprising success of obtaining a good diffraction pattern as well as nicely formed crystals of $Rb_4Zr_6Cl_{18}C$ from reacting the product of a reaction that had undergone annealing at lower temperatures (600-450°C) with excess Zr powder ($Rb_4Zr_6Cl_{18}C$:Zr 1:2). This suggests that the preheating procedure and the more reducing condition are probably crucial to stabilizing the crystalline cluster phase in question. It seems plausible that a slower reaction at lower temperature provides fewer nuclei, and this generally improves the quality of the crystallization; a more reducing condition may also alter the vapor pressure over the system to facilitate the formation of the desired phase. All the experiment observations indicate that the problem is not the stability of the cluster but the stability of the lattice, since the cluster unit has the normal 14

electron count whereas the lattice has neither direct cluster interconnections nor a close packed anion sublattice and might have a relatively low lattice energy.

The products from reactions to make analogue $K_4Zr_6Cl_{18}B$ behaved similarly to that described above. In addition, incomplete structure analyses (R ~ 15%, R_w ~ 20%) on crystals from a reaction with the stoichiometry of $Na_3Zr_6Cl_{15}C$ suggests that there is a sodium analogue of $Rb_4Zr_6Cl_{18}C$. The partial solutions show that the arrangement of the clusters and countercations is similar in these two compounds, except possible lattice distortions associated with replacing Rb by Na, which is believed to also contribute to the difficulties in obtaining a correct solution. On the other hand, efforts to replace the interstitial carbon by iron yielded mainly $MZr_6Cl_{15}Fe$ (M = Rb, Cs; $CsNb_6Cl_{15}$ type) and M_2ZrCl_6, which implies that the Fe analogues of this structure type are less stable.

Structure determination A single crystal selected from the original reaction (starting stoichiometry $Rb_3Zr_6Cl_{15}C$) was employed for the structure determination. The data collection was conducted on an Enraf Nonius CAD4 diffractometer. A primitive triclinic cell was obtained through indexing 25 reflections located by program SEARCH, and this was then transferred to a standard reduced C-centering monoclinic cell. Photos were taken along the three principal axes, and a mirror plane was observed perpendicular to the $\vec{b}$ direction. In order to further confirm the Laue symmetry, an additional photo was taken along the [110] direction, which showed the expected d spacing corresponding to the vector $\frac{1}{2}(\vec{a}+\vec{b})$. One hemisphere of data was collected with the C-centering condition (h+k=2n), and seven ψ-scans were measured. The data preparation included a nonlinear

decay correction for the 9% intensity loss during the 53-hour X-ray exposure, an empirical absorption correction with the ψ-scan measurements, and the Lorentz and polarization corrections. Other important parameters of the data collection and the structure refinement are summarized in Table 5.

The initial model was provided by program SHELXS-86[58] and was refined with least square calculations. The interstitial carbon was located on a difference Fourier map calculated after the heavier atoms were refined anisotropically. The occupancies of the C and Rb were refined and later fixed to be fully occupied since they were not significantly different from 100% (C, 98(2)%; Rb, 100.1(1)%) and the results agreed with the electron counting rule. The final difference Fourier map was flat with neither positive nor negative peaks higher than 1 $e^-/Å^3$. Important interatomic distances (Table 6) were calculated with the refined lattice constants from an indexed powder pattern with 42 observations. The refined temperature factors (Table 7) are about twice as large as those normally observed for Zr-Cl cluster systems, and most of the thermal ellipsoids are noticeably elongated along the b direction (the prism axis). Except for the slightly over-sized, yet still acceptable thermal parameters, the structure model refined satisfactorily to provide a reasonable stoichiometry and distances. Hence, rather than a problem with the space group, the ellipsoids are likely to be an indication of either an inadequate absorption correction or a low quality crystal associated with the difficulties in obtaining this compound in crystalline form, as discussed previously.

Structure description As a member of the M_8Cl_{18} family, $Rb_4Zr_6Cl_{18}C$ is composed of isolated $[Zr_6Cl_{18}C]^{4-}$ cluster units and Rb^+ ions. The

Table 5. Crystal Data for $Rb_4Zr_8Cl_{18}C$

space group	C2/m (No. 12)
Z	2
a, Å[a]	10.460(4)
b, Å	17.239(4)
c, Å	9.721(4)
β, deg	115.05(3)
V, Å^3	1588.0(9)
crystal dimen, mm	0.18 x 0.18 x 0.12
data collection instrument	ENRAF NONIUS CAD4
scan mode	ω-2θ
$2\theta_{max}$, deg	60
reflections	h, ±k, ±ℓ
measured	4852
observed	3076
absorp coeff μ, cm^{-1} (Mo Kα)	93.5
range of transm coeff	0.68 - 1.00
R_{ave}, %	3.2
second ext coeff	9(3) x 10^{-6}
R, %	2.4
R_w, %	3.3
largest residue peak, e$^-$/Å^3	+0.76 (0.85Å,Zr2) -0.71 (0.72Å,Rb)

[a]Guinier powder diffraction data (42 observations).

Table 6. Important Distances and Angles in $Rb_4Zr_6Cl_{18}C$

Distances (Å)

Zr-C	Zr1-C	x 2	2.2939(6)	Rb-Cl2	x 1	3.577(1)
Zr2-C		x 4	2.2831(4)	Rb-Cl3	x 1	3.4987(9)
Zr-Zr	Zr1-Zr2	x 4	3.2409(6)		x 1	3.780(1)
		x 4	3.2319(7)	Rb-Cl5	x 1	3.115(1)
	Zr2-Zr2	x 2	3.2292(6)	Rb-Cl6	x 1	3.188(2)
		x 2	3.2283(4)		x 1	3.287(1)
	$\bar{d}$		3.2338		x 1	3.186(2)
Zr-Cl[i]	Zr1-Cl3	x 4	2.551(1)	$\bar{d}$		3.376
$\bar{d}$	Zr1-Cl4	x 4	2.528(1)			
	Zr2-Cl1	x 4	2.538(1)			
	Zr2-Cl2	x 4	2.545(1)			
	Zr2-Cl3	x 4	2.545(1)			
	Zr2-Cl4	x 4	2.521(1)			
	$\bar{d}$		2.538			
Zr-Cl[a]	Zr1-Cl5	x 2	2.564(2)			
	Zr2-Cl6	x 4	2.606(1)			
	$\bar{d}$		2.592			

Angles (°)

Zr2-Cl1-Zr2	x 2	79.00(4)
Zr2-Cl2-Zr2	x 2	78.74(5)
Zr1-Cl3-Zr2	x 4	78.99(4)
Zr1-Cl2-Zr2	x 4	79.60(4)
average		79.15
Cl3-Zr1-Cl4	x 2	169.74(5)
Cl1-Zr2-Cl2	x 2	168.84(3)
Cl3-Zr2-Cl4	x 2	168.82(4)
average		169.14

Table 7. Positional and Thermal Parameters for $Rb_4Zr_6Cl_{18}C$

	x	y	z	B_{11}
Zr1	0.12273 (5)	0	0.85252 (5)	1.96(2)
Zr2	0.14648(4)	0.09366(3)	0.15148(4)	1.95(1)
Cl1	0.3265(2)	0	0.3325(2)	2.09(5)
Cl2	0	0.2078(1)	0	3.41(6)
Cl3	0.2981(1)	0.10448(7)	0.0053(1)	2.68(3)
Cl4	0.0256(1)	0.10443(7)	0.3266(1)	3.02(3)
Cl5	0.2625(2)	0	0.6903(2)	3.84(5)
Cl6	0.3134(1)	0.20005(8)	0.3266(1)	2.94(4)
Rb	0.39310(5)	0.16175(4)	0.68488(6)	4.05(2)
C	0	0	0	1.6(2)

B_{22}	B_{33}	B_{12}	B_{13}	B_{23}	B_{eq}
3.05(2)	1.27(1)	0	0.66(1)	0	2.10 (1)
2.79(2)	1.255(9)	-0.21	0.368(8)	-0.17(1)	2.102(7)
3.96(7)	1.63(4)	0	-0.04(4)	0	2.84(3)
2.71(6)	2.15(4)	0	0.32(4)	0	3.05(3)
4.50(5)	2.25(3)	-1.20(4)	1.15(2)	-0.48(3)	3.11(2)
3.91(5)	1.68(3)	-0.18(4)	1.03(2)	-0.58(3)	2.86(2)
4.95(9)	3.02(4)	0	2.37(3)	0	3.62(4)
3.87(5)	2.60(3)	-0.68(4)	0.48(3)	-0.95(4)	3.37(2)
4.76(3)	3.97(2)	-0.43(2)	1.70(1)	-0.74(2)	4.26(1)
3.0(3)	1.3(2)	0	0.3(2)	0	2.1(2)

isostructural relationship between $Rb_4Zr_6Cl_{18}C$ and the parent compound $K_4Nb_6Cl_{18}$[41] is obvious. The only significant differences are the expansion of the cluster core due to the change of the cluster metal and the presence of an interstitial atom, and the involvement of a larger counter cation, Rb^+. In addition, when compared to the solution of $K_4Nb_6Cl_{18}$, which was determined by film methods, the precision of the structure analysis on $Rb_4Zr_6Cl_{18}C$ is much higher due to the increased number of observations and improved accuracy on intensity measurements. The clusters form pseudo-close packed slabs in the (001) plane, and the Rb atoms are spread in the surface of these layers of clusters (Figures 6,7).

The cluster unit possesses C_{2h} symmetry imposed by the lattice and has the normal dimensions of a carbon-centered zirconium chloride cluster. Among the twelve Zr-Zr distances, there are four symmetry-related ones that are 0.009 Å (~13σ) longer than the rest, and this distortion is apparently connected with a matrix effect rather than electronically driven. The Zr-Cl^i distances have the normal average of a 14-electron carbon-centered cluster. In contrast, the Zr-Cl^a distances, which in general are more directly influenced by the cluster connectivity and countercations, are the shortest among all the $M_xZr_6Cl_{18}Z$ examples. This is because of the relatively low cation per cluster ratio as well as the weaker electrical field around each cation. Compared with $Li_6Zr_6Cl_{18}H$ and $Rb_5Zr_6Cl_{18}B$, the total count of cation–Cl^a contacts drops from 18 to 16 per cluster ($4Cl^a$ atoms per Rb x 4Rb atoms per cluster), resulting in a relatively smaller average coordination number (16/6) for the Cl^a and hence shorter Zr–Cl^a distances. For the same reason, the two Zr-Cl^a distances differ from each other as their coordination numbers are not equal (Cl5, CN = 1(Zr) + 2(Rb);

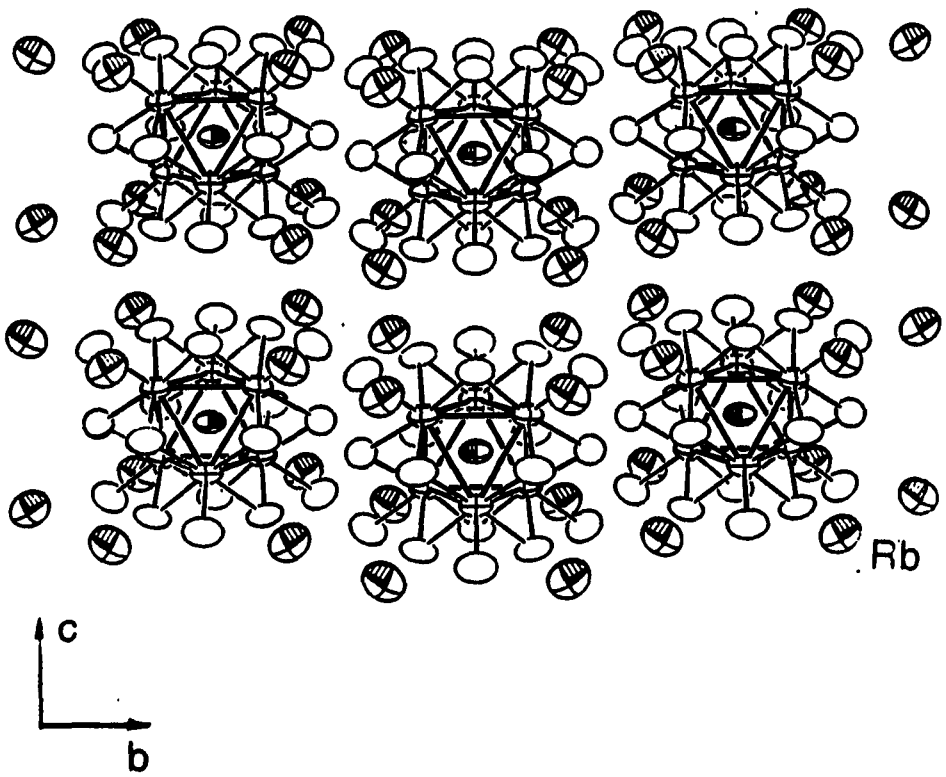

Figure 6. The [100] projection of $Rb_4Zr_6Cl_{18}C$ showing two cluster layers (90% probability). The clusters in the middle of the picture are related to those at the corners by C-centering. The 2-fold axis along $\vec{b}$ and the mirror plane perpendicular to $\vec{b}$ intersect at the center of the clusters

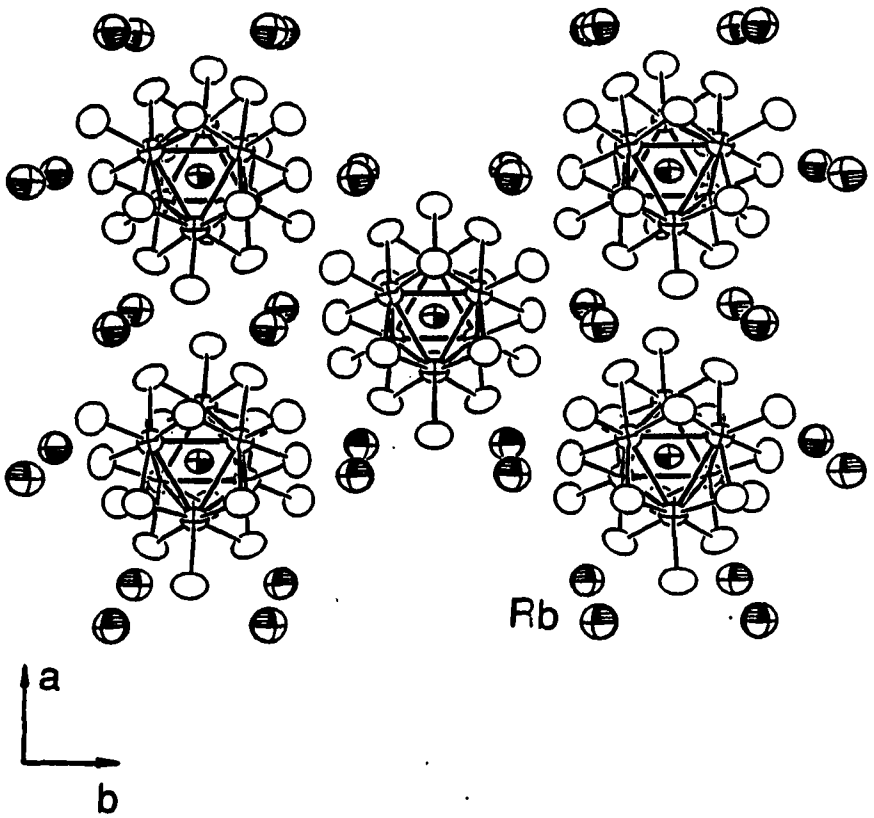

Figure 7. One cluster layer in C-centered $Rb_4Zr_6Cl_{18}C$ (90% probability). The 2-fold axis along b and the mirror plane perpendicular to b intersect at the center of the clusters

Cl6, CN = 1(Zr) + 3(Rb)). Moreover, in contrast to the multiply charged countercations in other 6-18 phases, such as Ba^{2+} in $K_2BaZr_6Cl_{18}C$ and $Ba_3Zr_6Cl_{18}Be$, Rb^+ has lower electrical field and consequently the Cl^a atoms are pulled closer to the cluster core. This phenomenon is repeatedly observed throughout Zr-Cl systems, and the simple ionic interaction argument works particularly well in the 6-18 family where there is no direct interconnection between clusters.

The Rb^+ ions are situated within the cluster layers and near the gaps separating these layers (Figure 7). As a result of the arrangement of the clusters and cations required by the stoichiometry and the nature of the cation, Rb^+ is located on a general position and its coordination polyhedron is rather anisotropic. Compared with the counter cation Li^+ in $Li_6Zr_6Cl_{18}H$, the Rb^+ ion is much larger and therefore prefers to occupy larger sites in the Cl layers instead of filling the octahedral vacancies between these layers. As there are fewer Rb^+ ions for each cluster, the average Rb-Cl distances are shorter in comparison with those for the three Rb sites in $Rb_5Zr_6Cl_{18}B$. For the same reason, the Rb atoms are located only on the surface of the cluster layers as opposed to both in the center of (Rb1) and between (Rb2, Rb3) the layers of clusters in $Rb_5Zr_6Cl_{18}B$.[40] Each Rb^+ is surrounded by four clusters in a pseudo tetrahedral fashion (Figure 8). The three clusters from the same layer form the base of the tetrahedron, contributing three Cl^i and three Cl^a atoms. These three Cl^a's define a triangular plane with the Rb atom residing at the center. An additional Cl^a (Cl6) that from the adjacent cluster layer caps this fragment at a slightly longer distance, and the three Cl^i atoms on the other side of the plane complete the Rb coordination polyhedron. The

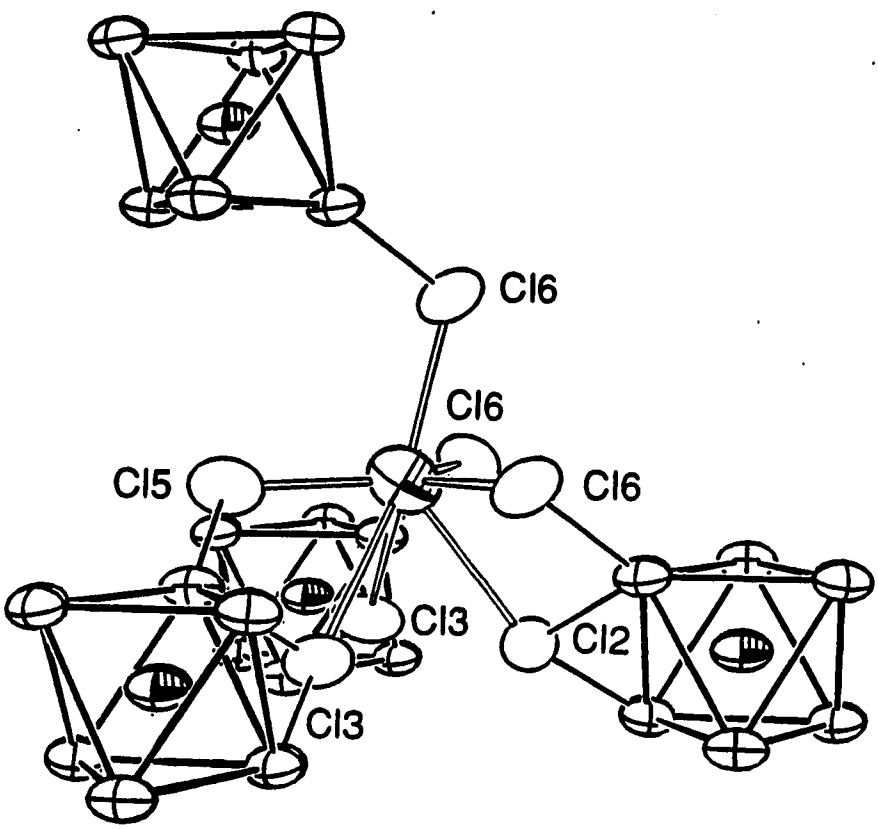

Figure 8. The coordination environment of Rb^+ ion in $Rb_4Zr_6Cl_{18}C$ and its surrounding cluster units (90% probability) with the $\vec{c}$ axis vertical

average distance from the Rb to the seven Cl's in its first coordination sphere is 3.376 Å, in good agreement with the summation of the corresponding crystal radii (Cl, 1.67 Å; Rb(CN=7), 1.70 Å).[66] The significant differences between individual Rb-Cl distances again reflect the function and therefore coordination number of each Cl; a Rb-Cl^a distance is at least 0.2 Å shorter than a Rb-Cl^i distance.

The lattice of $Rb_4Zr_6Cl_{18}C$ is composed of close packed cluster layers with the pseudo 3-fold axes of the clusters normal to the (001) plane. Yet, the stacking of these layers is not in a close packed manner owing to the fact that a three-dimensional, close-packed structure only generates two tetrahedral vacancies per cluster whereas the stoichiometry requires four cation sites for each cluster. There are two other structure types, namely, $Rb_5Zr_6Cl_{18}B$[40] and $Ba_2Nb_6Cl_{18}$,[70] that have similar two-dimensional close-packed cluster sublattices. Besides the fact that the clusters do not have the same orientation in $Rb_5Zr_6Cl_{18}B$, the major difference between $Rb_4Zr_6Cl_{18}C$ and the other two is that the clusters do not stack on top of each other and the $\vec{c}$ axis is not normal to these layers in the (001) plane. Instead, the layers slide with respect to each other, giving a β of 115°. This peculiar cluster array not only creates the required cation sites, but also provides maximum interaction between the Rb^+ and the Cl^a atoms. Another feature of this structure is that the chlorine atoms do not have close packed arrays. The chlorine sublattice is composed of chlorine layers parallel to the (001) plane. They contain close packed regions associated with the cluster units. Because of the intrusion of the Rb atoms in the same layers, the long range close-packed sublattice no longer exists. This may introduce certain instability of the structure.

After analyzing the structure, the poor crystallinity of $Rb_4Zr_6Cl_{18}C$ may be less puzzling. In contrast to $Rb_5Zr_6Cl_{18}B$, where the Rb atoms hold the clusters within the layers (Rb1) and also between the layers (Rb2, Rb3), $Rb_4Zr_6Cl_{18}C$ has only one type of Rb^+ that does not provide significant interaction between cluster layers. This Rb is bonded to the cluster layer where it resides much more strongly via three Rb-Cl^a and three Rb-Cl^i interactions. In the other layer, it only has one Cl^a as a close neighbor. Stacking faults caused by the lack of sufficient cation-anion attraction and maybe considerable Cl-Cl repulsion between cluster layers in combination with the unique array of the clusters as well as the anionic sublattice may hinder the crystallization process, yielding a material that does not exhibit long rang ordering. However, from the "destructive" point of view, these structural features may make $Rb_4Zr_6Cl_{18}C$ an interesting layered compound for intercalation studies and a good candidate for investigating a cluster solution chemistry.

$(K,Ba)_2BaZr_6Cl_{18}C$ and other compounds with the double salt structure

The double salt, $K_2ZrCl_6 \cdot Zr_6Cl_{12}H$ ($=K_2Zr_7Cl_{18}H$),[22] was among the first few Zr-Cl cluster compounds discovered. It was first characterized as an empty cluster and later corrected to be a H-centered cluster. This structure was also the first M_6X_{18} type in the Zr-Cl systems. Many interesting structure features of this group of compounds are to a great extent due to the two different cation positions, namely, the M and M′ position in the general formula of $M_xM'Zr_6Cl_{18}Z$. Since its discovery, several clusters adopting this structure type had been found, including Zr-Cl clusters (M = alkali metal; M′ = Zr; Z = H, Be; x = 2)[42] and a group of ternary or quaternary Nb-Cl clusters (M = alkali metal; M′ =

rare earth metal; x = 0-2).[73] The recent progress in searching for new cluster phases with the double salt structure originated with a desire to expand the diversity of their chemical compositions. By selecting the proper combination of M, M′ and Z (M = alkali metal; M′ = rare-earth metal or alkaline-earth metal; Z = B, C, Mn, or Fe; x = 1, or 2), a cluster phase with either a 14- or 18-cluster electron count may be synthesized. In addition, it was observed that this group of compounds exhibits intriguing interstructural relationships with two other structure types. The structure variations induced by the changes in the size, occupancy and charge of the countercations will be illustrated with three examples, namely, $(K_{.85}Ba_{.13})_2BaZr_6Cl_{18}C$ ($K_2Zr_7Cl_{18}H$ type), $CsLaZr_6Cl_{18}Fe$ ($CsLuNb_6Cl_{18}$ type) and $Ba_3Zr_6Cl_{18}Be$. It is worthwhile to point out that, although the quaternary Nb–Cl clusters exhibit both the $K_2ZrCl_6 \cdot Zr_6Cl_{12}H$ and the $CsLuNb_6Cl_{18}$ structure types, the relationships between these two structure types were not properly emphasized.[43,73] This was partially due to the lack of detailed descriptions and profound understanding of the structural chemistry of the related compounds. In the succeeding sections, the connections and differences between the above three 6–18 structures will be addressed, following the structure description of each of these compounds.

Synthesis The new $M_xM'Zr_6Cl_{18}Z$ phases with the double salt structure are listed in Table 8 with the lattice constants refined from Guinier powder diffraction data. The compounds with countercations Ca^{2+} or La^{3+} were obtained by design to produce Zr-Cl analogues of the rare-earth-metal containing Nb-Cl cluster phases. In contrast, $(K,Ba)_2BaZr_6Cl_{18}C$ and $(Cs,Ba)_2BaZr_6Cl_{18}Fe$ were first discovered from

Table 8. Cell Parameters (Å) and Volumes (Å^3) for the $K_2ZrCl_6 \cdot Zr_6Cl_{12}H$-Type Compounds[a] (space group $R\bar{3}$, hexagonal setting)

Compound	a	c	V
$K_2LaZr_6Cl_{18}B$	9.5749 (9)	26.661 (5)	2116.8 (5)
$KLaZr_6Cl_{18}C$	9.538 (2)	26.549 (5)	2091.7 (8)
$Cs_2LaZr_6Cl_{18}Mn$	9.7996 (5)	27.296 (3)	2270.1 (3)
$KCsLaZr_6Cl_{18}Mn$	9.7478 (9)	27.210 (3)	2239.1 (5)
$KLaZr_6Cl_{18}Fe$	9.703 (3)	26.88 (1)	2191 (2)
$CsLaZr_6Cl_{18}Fe$[b]	9.746 (2)	27.197 (7)	2237.3 (9)
$(K,Ba)_2BaZr_6Cl_{18}C$[c]	9.5950 (4)	26.926 (2)	2146.8 (3)
$Cs_2CaZr_6Cl_{18}Fe$	9.6890 (4)	27.113 (2)	2204.3 (3)
$KCsCaZr_6Cl_{18}Fe$	9.6335 (6)	27.013 (2)	2171.1 (3)
$(Cs,Ba)_2BaZr_6Cl_{18}Fe$	9.8697 (2)	27.653 (4)	2332.8 (5)

[a]All values are from Guinier powder diffraction data.

[b]Coexists with the $P\bar{3}1c$ phase. See text.

[c]The real stoichiometry is $(K_xBa_y)_2BaZr_6Cl_{18}C$ with x = 0.85(9) and y = 0.13(3).

reactions aimed at making $MBaZr_6Cl_{17}Z$ (M = K, Cs; Z = C, Fe) compounds; therefore, they are alkali metal deficient and have mixed cations in one position. All these phases can be made in high yield (>95%) starting with the correct stoichiometries, except for the special cases (M = Rb, Cs; Z = C, Fe; x = 1) where the phases with the double salt structure[43] (space group $R\bar{3}$) were always obtained in the company of the phases with the $CsLuNb_6Cl_{18}$ structure (space group $P\bar{3}1c$), which is a variation of the former. These cases have two common features: first, as required by the cluster electron count, the M site in the $R\bar{3}$ structure is 50% occupied, and second, the monovalent countercation has a relatively large size (M = Rb, Cs). It was observed that a $R\bar{3}$ phase was never obtained free of the $P\bar{3}1c$ phase even though sometimes its yield could be as high as 60%, and a long equilibration usually converted it to its $P\bar{3}1c$ counterpart. Detailed studies concerning this transition will be discussed under the compounds with the $P\bar{3}1c$ structure ($CsLuNb_6Cl_{18}$ type).

Structure determination The crystal used for single crystal analysis was obtained from a reaction loaded to make $KBaZr_6Cl_{17}C$, a hypothetical 14-electron carbon-centered 6-17 phase. However, a 6-18 phase with the double salt structure was produced. The deep red transparent gem was indexed on the diffractometer with a rhombohedral cell, in agreement with the powder pattern information that the main product was isostructural with $K_2Zr_7Cl_{18}(H)$ ($R\bar{3}$). Although the structure type was known, a single crystal analysis was necessary to determine the chemical composition, and to prove that an alkaline-earth metal may occupy the M′ position. The data were collected on the RIGAKU

diffractometer after the unit cell and its LAUE symmetry ($\bar{3}$) were confirmed by axial photos and the Laue program. One hemisphere of data was collected with the confirmed reflection condition for R-centering and the obverse setting ($-h+k+\ell=3n$). Other important crystal data are listed in Table 9.

Since the analysis of the standard reflections indicated only a small net intensity increase of 3%, presumably caused by the power fluctuation of the X-ray source, no decay correction was made. An empirical absorption correction was conducted based on the averaged curve from three ψ-scans. As a careful examination of the data set did not give any additional extinction conditions, the only possible choices for the space group were $R\bar{3}$ and R3. Then the three-fold redundant data ($I>0$) were averaged for the $R\bar{3}$ Laue class with surprising low R_{ave} (2.1%), apparently due to the high percentage of observed data (81% with $I>3\sigma_I$). The space group of the parent compound, $R\bar{3}$, was chosen, and refinement using $K_2Zr_7Cl_{18}(H)$ as model but replacing Zr2 with Ba was successful. The difference Fourier map revealed a residue peak about 5 $e^-/Å^3$ at the center of the Zr_6 cluster after the heavier atoms had been refined anisotropically. A carbon atom was added to the interstitial site, based on the 14-electron rule and the interstitial element available in the starting materials, and this was followed by a refinement to a satisfactory level.

The occupancy of the cation positions as well as the interstitial site were examined, and both Ba and C were, as expected, fully occupied (Ba 100.2(2)%; C 100(2)%). The simultaneous refinement of the thermal parameters and occupancy of the K position, on the other hand, seemed to

Table 9. Crystal Data for $M_2BaZr_6Cl_{18}C$[a]

space group	$R\bar{3}$ (No. 148)
Z	3
a, Å[b]	9.5950(4)
c, Å	26.926(1)
V, Å^3	2146.8(2)
crystal dimen, mm	0.40 x 0.14 x 0.12
data collection instrument	RIGAKU AFC6R
scan mode	ω-2θ
$2\theta_{max}$, deg	60
reflections	h, ±k, ±ℓ
measured	4398
observed	3554
observed independent	1148
absorp coeff μ, cm^{-1} (Mo Kα)	54.1
range of transm coeff	0.80 - 1.00
R_{ave}, % (I > 0)	2.1
second ext coeff	1.3(5) x 10^{-8}
R, % (I > 3σ_1)	1.5
R_w, %	2.3
largest residue peak, e$^-$/Å^3	+0.5(0.46 Å, to K)
	-0.6 (0.9 Å to Zr)

[a]M = $K_{0.85(9)}Ba_{0.13(3)}$.
[b]Guinier powder diffraction data (48 observations).

be troublesome. While the B_{iso} increased from 2.87(6) to 3.85(4), the occupancy of K boomed up to 125.9(5)% which is structurally impossible. Considering the facts that the reaction was loaded with a K deficiency, and the 12-coordinate K site is large enough for a Ba, partial substitution of K by Ba seemed possible. Therefore, K and a second Ba, Ba2, were refined on the same position with proper constrains on both the positional and thermal parameters. Taking the probably 14-electron count into consideration, the total charge contributed by each mixed cation position ($M = K_xBa_y$) should be +1 ($x + 2y = 1$), and as a consequence, the total occupancy of this position must be less than 1 ($x + y < 1$). Hence, the multiplicities of both K and Ba2 were refined independently, resulting a mixed cation position of $K_{.85(9)}Ba_{.13(3)}$. The validity of this refinement was supported first by the improved quality of the entire structure solution. Compared with the model with 100% K on the M site, the mixed cation model reduced the residue peak around this position from 2.5 $e^-/Å^3$ to 0.5 $e^-/Å^3$, and the standard deviations of all of the positional and thermal parameters were decreased by a factor of two. The chemical meaning of this model was also evaluated. Besides the acceptable total occupancy ($x + y < 1$), the total charge of this position agrees with the 14-electron rule within the experimental error ($x + 2y = 1.1(1)$). In addition, the refined result is consistent with the average distance from this mixed cation to the neighboring chlorines and the fact that Ba does occupy a similar position in $Ba_3Zr_6Cl_{18}Be$. Although a chemical analysis is at the present not available, this solution was accepted. The refined final positional and thermal

parameters as well as important distances and angles are listed in Tables 10 and 11, respectively.

Structure description The structure of $(K_{0.85}Ba_{0.13})_2BaZr_6Cl_{18}C$ is built with three fragments: the cluster unit, the Ba^{2+} ion and the mixed cation position (Figure 9). The $[Zr_6Cl_{18}C]^{4-}$ cluster in $(K_{.85(9)}Ba_{.13(3)})_2BaZr_6Cl_{18}C$ has S_6 point symmetry, and the Zr_6 metal core deviates from an ideal octahedron through a slight trigonal compression. The two types of crystallographically different Zr-Zr distances differ from each other by 0.013 Å (43σ, 0.4%), which is much less than what was observed in the parent compound, $K_2Zr_7Cl_{18}(H)$,[22] a 13 e^- cluster phase that has a cation Zr^{4+} with a stronger electric field. The Zr-C distance and the average Zr-Zr distance fall into the range expected for a 14-electron carbide cluster and so does the average Zr-Cl^i distance. The difference between the two types of Zr-Cl^i bonds follows the same pattern observed for the parent compound, with the shorter one, namely, Zr-Cl2, reflecting the lower coordination number (Cl1, CN = 2(Zr) + 2(K); Cl2, CN = 2(Zr) + 1(K)). The Zr-Cl^a distance is shorter than a representative Zr-Cl^{a-a} for many carbon centered clusters or the Zr-Cl^a in $K_2Zr_7Cl_{18}(H)$ which all have two Zr as their nearest neighbors, apparently caused by the weaker interaction between this Cl (Cl3) and the Ba^{2+} instead of Zr^{4+}.

The Ba^{2+} occupies the 6-coordinate M′ position. The local symmetry of the $[BaCl_6]^{4-}$ group is D_{3d} (Figure 10), and it distorts away from a perfect octahedron through a trigonal compression (Cl3-Cl3 4.538 vs 4.134 Å). The Ba-Cl distance, 3.0651 Å, is less than the sum of crystal radii [1.49 (Ba^{2+}, CN=6) + 1.67 (Cl^-) Å] and it is the shortest of the

Table 10. Positional and Thermal Parameters for $M_2BaZr_6Cl_{18}C$[a]

	x	y	z	B_{11}
Zr	0.02423(2)	0.20502(2)	0.048597(7)	1.145(8)
Cl1	0.22490(7)	0.19787(7)	0.10920(2)	1.89(2)
Cl2	0.42599(6)	0.17339(7)	0.00019(2)	0.99(2)
Cl3	0.04060(8)	0.43723(7)	0.10405(2)	2.47(2)
Ba	0	0	1/2	1.792(8)
M	0	0	0.22080(5)	3.17(6)
C	0	0	0	1.11(8)

[a] $M = K_{.85(9)}Ba_{.13(3)}$.

B_{22}	B_{33}	B_{12}	B_{13}	B_{23}	B_{eq}
0.963(8)	1.019(8)	0.547(6)	-0.013(4)	-0.151(4)	1.06(1)
1.79(2)	1.57(2)	1.00(2)	-0.62(2)	-0.57(2)	1.76(3)
1.98(2)	2.00(2)	0.60(2)	0.06(2)	0.40(2)	1.74(3)
1.71(2)	2.06(2)	1.07(2)	-0.17(2)	-0.79(2)	2.11(3)
B_{11}	1.89(2)	$1/2B_{11}$	0	0	1.85(2)
B_{11}	5.76(2)	$1/2B_{11}$	0	0	2.87(6)
B_{11}	1.0(2)	$1/2B_{11}$	0	0	1.0(2)

Table 11. Important Distances and Angles in $M_2BaZr_6Cl_{18}C$[a]

Distances (Å)						
Zr-C		x 6	2.2757(2)	Ba-Cl3	x 6	3.0651(6)
Zr-Zr		x 6	3.2118(3)			
		x 6	3.2248(3)			
	$\bar{d}$		3.2183	M-Cl1	x 3	3.632(1)
Zr-Cl[i]	Zr-Cl1	x 6	2.5460(6)	M-Cl1	x 3	3.7624(6)
		x 6	2.5509(6)	M-Cl2	x 3	3.646(1)
	Zr-Cl2	x 6	2.5237(5)	M-Cl3	x 3	3.2160(6)
		x 6	2.5251(6)	$\bar{d}$		3.564
	$\bar{d}$		2.5364			
Zr-Cl[a]	Zr-Cl3	x 6	2.6207(5)			
Angles (°)						
Zr-Cl1-Zr		78.50(2)				
Zr-Cl2-Zr		79.01(2)				
C-Zr-Cl3		177.85(2)				
Zr-Cl3-Ba		124.60(2)				
Cl3-Ba-Cl3		180, 92.64(2), 87.36(2)				

[a]M = $K_{.85(9)}Ba_{.13(3)}$.

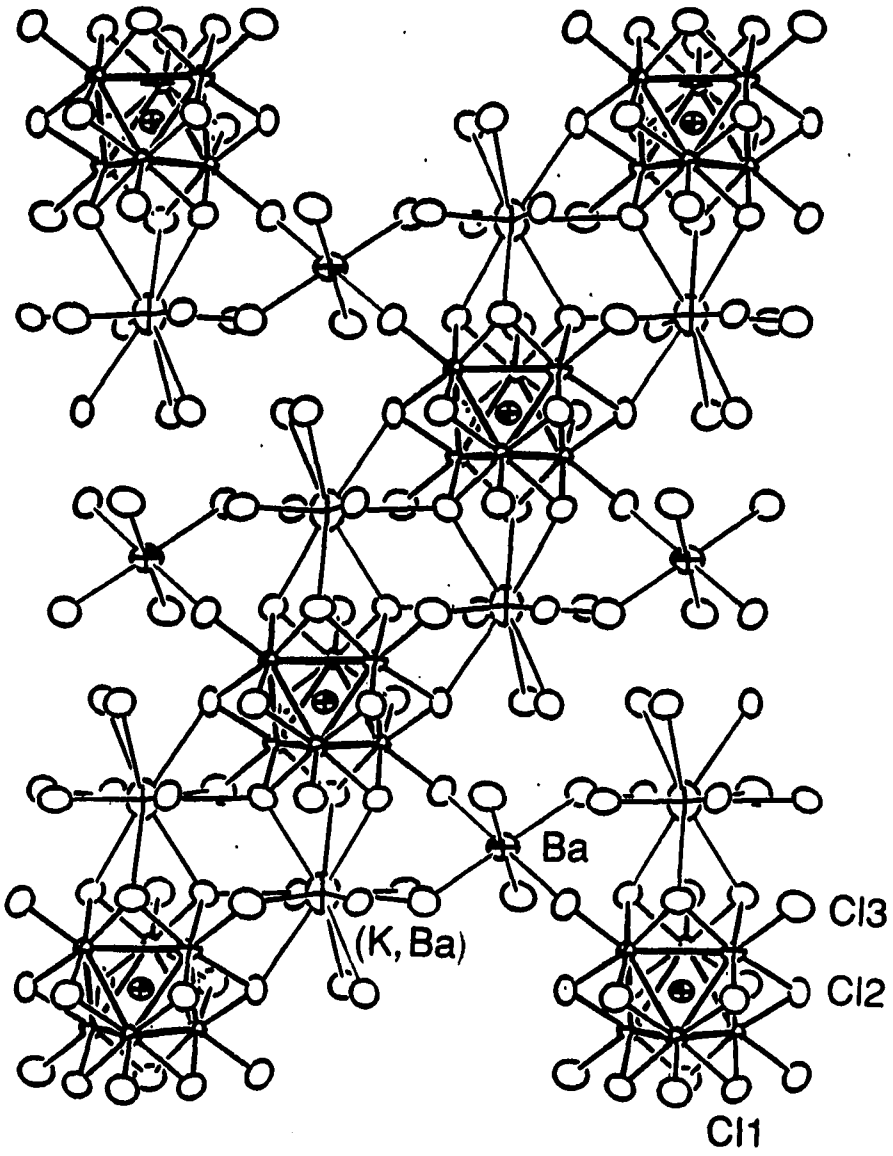

Figure 9. The [110] projection of $(K,Ba)_2BaZr_6Cl_{18}C$ (90% probabilities)

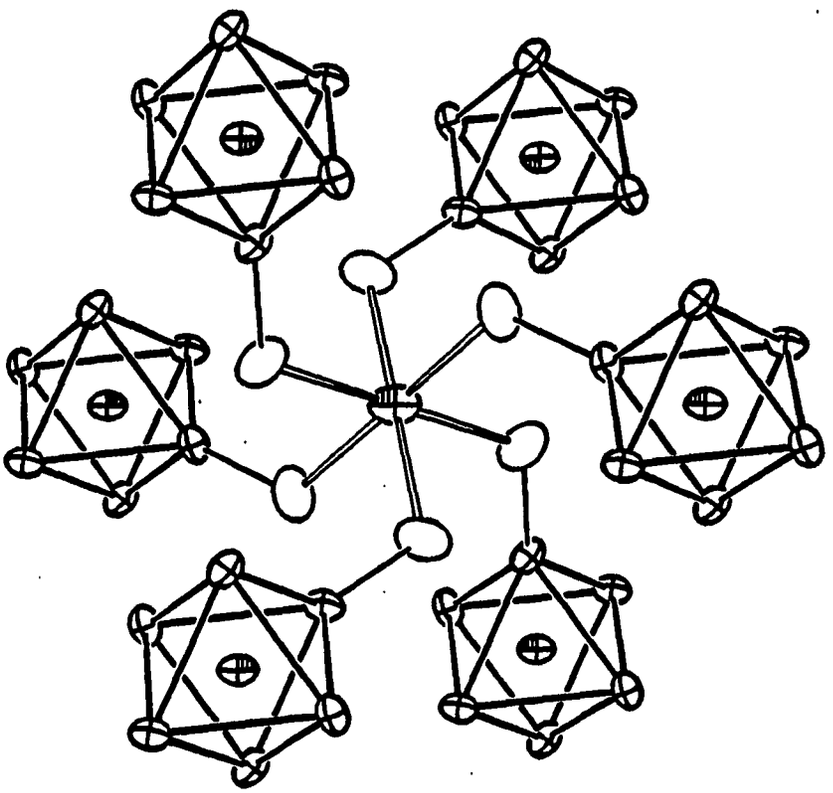

Figure 10. The Ba coordination environment in $(K,Ba)_2BaZr_6Cl_{18}C$ and its surrounding cluster units (90% probabilities). The $BaCl_6^{2-}$ group processes D_{3d} symmetry (3-fold axis perpendicular to the plane of the paper)

Ba-Cl distances observed in Ba-containing cluster compounds, namely, $Ba_2Zr_6Cl_{17}B$ and $Ba_3Zr_6Cl_{18}Be$. Each Ba is connected to six cluster units via Cl^a atoms, and although its size and chemical properties are quite different from Zr^{4+} in $K_2Zr_6Cl_{18}(H)$ and RE^{3+} in the niobium clusters compounds, it performs the same function in this structure as do the other two cations, i.e., constructing a structure network by linking the clusters together.

The mixed K and Ba position, referred as M, is 12-coordinate (Figure 11). Although it has only C_3 crystallographic symmetry, the coordination polyhedron is rather regular. M has three short and three long M-Cl distances around its waist, and six other chlorine neighbors in the intermediate range at its top and the bottom. M is a member of the close-packed layers dominated by Cl atoms (Figure 9). If the clusters are considered as the basic structural elements, the mixed cations are in the tetrahedral vacancies formed by the clusters, among which one contributes three Cl1 while each of the other three provides one Cl1, one Cl2 and one Cl3. The interactions between M^+ and the cluster cores displace the M^+ away from the Zr atoms at closer distances (4.52 vs 5.00 Å), and the M moves slightly (0.16 Å) off the center of the close-packed layer formed by Cl1 and Cl3 (upward in Figure 11). The striking difference of over 0.4 Å in M-Cl^i and M-Cl^a distances once again is induced by the difference in the relative strengths of the fields around each Cl atom. With lower total effective positive charge around it, Cl3 (CN = 1(Zr) + 1(Ba) + 1(M)) has the M-Cl distance well below the sum of the corresponding crystal radii (K^+ CN=12, 1.78 Å; Ba^{2+} CN=12, 1.75 Å; Cl^- 1.67 Å), while the rest of the M-Cl distances are

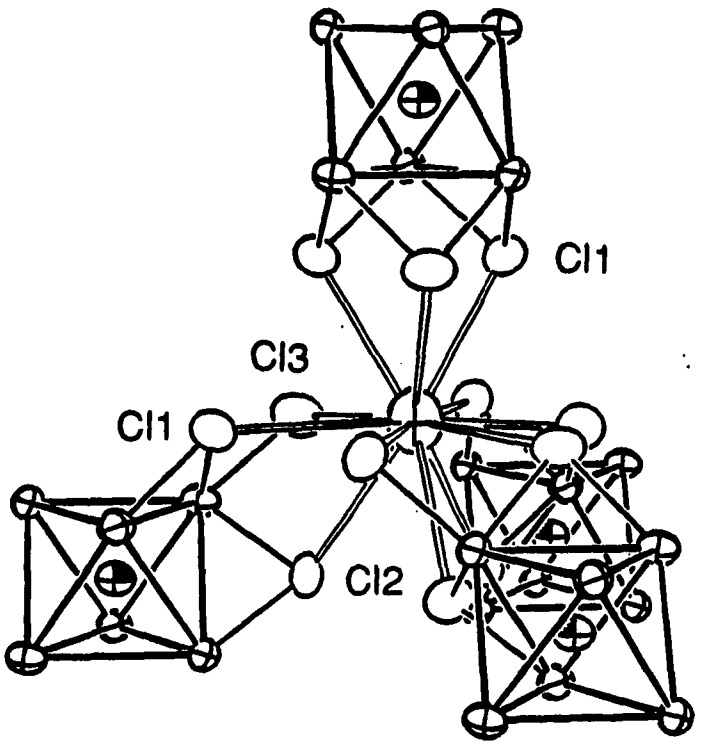

Figure 11. The mixed cation site in $(K,Ba)_2BaZr_6Cl_{18}C$ (90% probabilities). The MCl_{12} fragment has C_3 symmetry (3-fold axis vertical) and there are four cluster units around it

above this value. In contrast to this observation, the order of the K-Cl^a and the K-Cl^i distances in the parent double salt, $K_2ZrZr_6Cl_{18}H$, are reversed and the difference between them is less pronounced (<0.2 Å), due to the fact that the counter cation Zr^{4+} makes the Cl^i and Cl^a atoms experience a more similar effective electrical field. Since the structure framework is defined by the clusters and cluster connections through Ba, the function of M is basically filling space and providing electrons. Although its structural and electronic contributions are essential to the stabilization of this phase, the M-Cl interaction is considered of less importance compared with other types of bonds. This is reflected by the rather significant deviation of the averaged M-Cl distance from the sum of the crystal radii as well as its large thermal ellipsoid that is somewhat elongated along $\vec{c}$. As also observed in the parent compound, the oversized monovalent cation position and the smaller distance between the multivalent cation to its neighboring Cl's seem to be a common character of the double salt structure, which is a direct indication of the different functions of the above two structural elements.

The close-packed-layer representation of this structure has been clearly stated for the parent compound.[22] $M_2BaZr_6Cl_{18}C$ also has nine layers along $\vec{c}$, with sequence of (...ABABCBCAC...) or $(chh)_3$. The cross-section of the unit cell perpendicular to $\vec{c}$ contains seven close-packing positions (7x9 in each unit cell) which are occupied by either Cl, C, or K atoms (3x(2K+18Cl+C) in each unit cell), with no vacancies. The layers are approximately equally spaced, except the three layers around the common cluster core are pulled closer to each other (2.88 Å

apart) by Zr atoms while the layers having only Ba^{2+} in between are further apart (3.23 Å). The closest Cl neighbors are separated by 3.3968(8) Å (Cl2-Cl3), and the short distance is believed as the result of their connections to the common Zr and M atoms.

$CsLaZr_6Cl_{18}Fe$ and other compounds with the $CsLuNb_6Cl_{18}$ structure

Synthesis The Zr-Cl clusters (Table 12) with the general formula of $MLaZr_6Cl_{18}Z$ (M = Rb, Cs; Z = C, Fe) and structure of $CsLuNb_6Cl_{18}$[43] (space group $P\bar{3}1c$) were obtained in the systems where cluster electron count requires only one M for each cluster unit, and M is a relatively large alkali metal. Without special treatment, a reaction loaded for the stoichiometry and quenched in air after being heated at a temperature between 800 and 850°C for about two weeks always produces a mixture of the $R\bar{3}$ and the $P\bar{3}1c$ phase. This phenomenon was also observed in the 16-electron Nb-Cl cluster systems for the Rb but not the Cs series.[43] However, it was not well understood or at least not well explained. The nature of this equilibrium or transition was pursued using $CsLaZr_6Cl_{18}Fe$ as the subject.

As the $P\bar{3}1c$ structure allows only one M per cluster whereas the $R\bar{3}$ structure may accept up to two M atoms per cluster, the stoichiometry of the reactions were varied. Yet, increasing the M content in the starting materials alone neither lowers the relative yield of the $P\bar{3}1c$ phase nor change the lattice constants of the $R\bar{3}$ phase, indicating that the stoichiometries of these products are to a large extent regulated by the electron counting rule, and that the transition between these two phases which apparently have the same composition is unlikely to be stoichiometrically driven. The influence of a second factor, the

Table 12. Cell Parameters (Å) and Volumes (Å^3) for the $CsLuNb_6Cl_{15}$-Type Compounds[a] (Space group $P\bar{3}1c$)

Compound	a	c	V
$CsLaZr_6Cl_{18}Fe$	9.6404 (4)	18.332 (1)	1475.5 (2)
$RbLaZr_6Cl_{18}Fe$	9.6229 (9)	18.262 (3)	1464.5 (4)
$CsLaZr_6Cl_{18}C$	9.5098 (9)	17.939 (3)	1405.0 (3)

[a]All values are Guinier powder diffraction data.

temperature, was also studied. Since the two space groups do not have a group-subgroup relation, the possibility of a second order phase transition was eliminated, in agreement with the fact that in several reactions the two phases coexisted in a temperature range as wide as from 600 to 900°C. For a first order phase transition, the ratio of the two phases at equilibrium should vary as the function of the temperature. Studies in the Nb-Cl systems concluded that the $R\bar{3}$ phase was mainly formed at 700°C, whereas the ratio of the two phases changed with temperatures below 800°C,[73] which could imply that the $R\bar{3}$ phase was the low temperature phase.

Contrary to this observation, similar experiments in the $CsLaZr_6Cl_{18}Fe$ system seemed to point to different results. Among two reactions having the same stoichiometry, reaction temperature and heating period, the one that was quenched from the reaction temperature has the higher content of the $R\bar{3}$ phase than the one that was annealed at lower temperature or slow cooled to 400°C afterward. However, the conclusion that the product ratio is temperature dependent or that lower temperature favors the $P\bar{3}1c$ phase cannot be drawn before the third factor, the reaction time, is also taken into consideration, because the quenched reactions obviously also had shorter total reaction periods. Another group of reactions that started with the same stoichiometry were then carried out at 700 and 900°C, respectively. They were heated for the same period of time, 70 days, which was supposed to be sufficient for each system to achieve equilibrium. The result of this experiment was surprising at the time, as both reactions yielded a single phase product, the $P\bar{3}1c$ phase. Thus, the new interpretation of the above

observations is that the $R\bar{3}$ phase is a metastable phase between the starting materials and the final product $P\bar{3}1c$ phase. The transition from the $R\bar{3}$ phase to the thermodynamically more stable $P\bar{3}1c$ phase has a high energy barrier and therefore requires a long reaction time. This conclusion agrees with other experimental observations. First, the $R\bar{3}$ phase is the one with both a higher symmetry and a random partial occupation of the Cs position, which is also apparently less stable under the conditions examined. Second, for $CsLaZr_8Cl_{18}Fe$, the formula volume of the $R\bar{3}$ phase is 1% (8 $Å^3$/cluster) larger than that of the corresponding $P\bar{3}1c$ phase, and the higher space filling efficiency makes the $P\bar{3}1c$ phase more favorable under the conditions investigated.

Comparing the Nb-Cl systems against their Zr-Cl counterpart, on one hand, it is clear why this type of transition occurred among the $RbRENb_6Cl_{18}$ clusters, whereas the $CsRENb_6Cl_{18}$ series exhibited only the $P\bar{3}1c$ phase. The relatively smaller Nb_6 cluster core (Nb-Nb 2.91 to 2.92 Å in $CsLuNb_6Cl_{18}$) means that the countercation Cs^+ is so large that the $R\bar{3}$ phase is destabilized with respect to the $P\bar{3}1c$ phase. On the other hand, the different behaviors of this transition in the Nb and Zr cluster systems remain as a puzzle. Although there is no available information on the relative densities of the two structure types the symmetry and the occupancy arguments are still valid. One possibility might be that those $RbRENb_6Cl_{18}$ systems investigated did not achieve equilibrium and, at lower temperature, the conversion from the $R\bar{3}$ phase to the corresponding $P\bar{3}1c$ phase was slow, resulting in the observed higher percentages of the $R\bar{3}$ phases in the final product.

The Zr-Cl cluster compounds with the $CsLuNb_6Cl_{18}$ structure have several restrictions on their chemical compositions. The interstitial elements that are required by the cluster electron count and the M/cluster ratio are at present limited to C and Fe, while the multivalent cation has to be La or, supposedly, any other rare-earth metal. Using N as the centering atom has not been attempted. Meanwhile, efforts to make a Co analogue of this structure type, or as a matter of fact, of any 6-18 compounds led to the formation of $Zr_6Cl_{15}Co$ (Nb_6F_{15} type). Substitution of an alkaline-earth metal for La or change the interstitial to B or Mn both require an increase in the alkali metal/cluster ratio to two, and hence form only the $R\bar{3}$ phase. In addition, as mentioned previously, there is also a restriction on the size of the alkali metal. For small alkali metals, namely, K in Zr-Cl systems and Na or K in Nb-Cl systems,[73] the corresponding cation position in the $P\bar{3}1c$ structure is too big, and the $P\bar{3}1c$ phase is destabilized, in fact not observed. Instead, the $R\bar{3}$ phases with 50% occupied alkali metal sites are formed.

Structure determination The single crystals used for X-ray analysis were selected from a reaction with the proper stoichiometry of $CsLaZr_6Cl_{18}Fe$ (800-900°C temperature gradient, 50 days). The powder pattern of the product indicated that the major cluster phase (30%) was the $R\bar{3}$ $CsLaZr_6Cl_{18}Fe$. These crystals were black under reflected light, dark purple under transmitted light, and had roughly rod-like shapes. The first few crystals examined on RIGAKU belonged to the $R\bar{3}$ phase and seemed to have a twinning problem. Although the INDEX program could index every reflection found by SEARCH, giving the rhombohedral cell as

expected, the profiles of the peaks showed significant splitting. Therefore, several crystals were tried until one providing satisfactory peak profiles was found. However, this crystal was indexed to a primitive hexagonal cell, corresponding to that of the $P\bar{3}1c$ $CsLaZr_6Cl_{18}Fe$. Axial photos were normal yet failed to provide any symmetry information, and program LAUE indicated only $\bar{3}$ symmetry. Therefore, one hemisphere of data was collected. At the end of the data collection, another Laue check was conducted with refined cell parameters and orientation matrix, again without being able to provide the expected Laue symmetry, $\bar{3}1m$, as in the supposed parent compound $CsLuNb_6Cl_{18}$. Other important data collection parameters are listed in Table 13.

The structure determination began with the determination of the space group. Although the ability of RIGAKU to provide symmetry information through axial photos and the LAUE program is limited, careful analysis of the data set clearly revealed the presence of c-glides along the $\vec{a}$, $\vec{b}$ and $\vec{a}+\vec{b}$ direction ($hh2\bar{h}\ell$, $\ell=2n$). Combining the lattice type and the LAUE symmetry, the possible space groups were limited to $P\bar{3}1c$ and $P31c$. At this point, it was almost certain that the crystal under study was isostructural with $CsLuNb_6Cl_{18}$ ($P\bar{3}1c$). No decay correction was necessary since the intensity of the standard reflections changed only 0.3%. After an empirical absorption correction based on three ψ-scan measurements was applied, the six-fold redundant data with positive intensities were averaged, resulting in a rather high R_{ave} that was caused by a lower signal/noise ratio and large uncertainty of the weaker reflections. Successive isotropic and anisotropic refinements using $CsLuNb_6Cl_{18}$ as a model were successful, and the subsequent Fourier

Table 13. Crystal Data for $CsLaZr_6Cl_{18}Fe$

space group	$P\bar{3}1c$ (No. 163)
Z	2
a, Å[a]	9.6404(4)
c, Å	18.332(1)
V, Å^3	1474.7(2)
crystal dimen, mm	0.20 x 0.12 x 0.10
data collection instrument	RIGAKU AFC6R
scan mode	ω-2θ
$2\theta_{max}$, deg	60
reflections	h, ±k, ±ℓ
measured	8996
observed ($I > 3\sigma$)	5005
observed independent	957
absorp coeff μ, cm^{-1} (Mo Kα)	67.5
range of transm coeff	0.70 - 1.00
R_{ave}, % ($I > 0$)	8.9
second ext coeff	0
R,%	3.0
R_w,%	4.2
largest residue peak e$^-$/Å^3	+2.2(1.2 Å, Cs) -2.9(0.3 Å, Fe)

[a]Guinier powder diffraction data (60 observations).

synthesis clearly indicated a large residue peak at the center of the Zr_6 cluster (~20 $e^-/Å^3$) on the difference map. Then an Fe atom was added to the atom list and was refined satisfactorily. The simultaneous refinement of the thermal parameters and occupancy of the two cation positions showed they are fully occupied (La 101.2(4)%, Cs 103.0(5)%), whereas the study of the interstitial site led to only 81.0(6)% occupancy of Fe. A similar phenomenon has been noticed for other cluster phases of both main-group and transition metal interstitials. Rather than a true structural defect at the interstitial site, this is attributed to the crystallographic errors, which often result in troublesome systematic errors at high symmetry positions. This assumption agreed with the fact that refining the occupancy of Fe did not improve the quality of the solution significantly, although a decrease of 5 to 10% of the standard deviations was observed. The problem could not be corrected with DIFABS,[62] and in the final step of the structure refinement, all the atom positions were fixed at 100% occupancy corresponding to the formula $CsLaZr_6Cl_{18}Fe$. Attempts to refine the secondary extinction coefficient were not successful, indicated by its small negative value and large standard deviation, and it was fixed at zero and ignored in the refinement process. The final difference Fourier map was essentially flat for 2 $e^-/Å^3$ residues in the center of the rings of six-chlorine atoms on the top and the bottom of the Cs, and a negative peak of 3 $e^-/Å^3$ associated with the interstitial Fe which was fixed at 100% occupancy. The refined positional and thermal parameters are listed in Table 14, and the important distances and angles are reported in Table 15.

Table 14. Positional and Thermal Parameters for $CsLaZrCl_6Cl_{18}Fe$

	x	y	z	B_{11}
Zr	0.22047(6)	0.04109(7)	0.07524(3)	1.14(2)
Cl1	0.1919(2)	0.2344(2)	0.1610(1)	1.92(6)
Cl2	0.1494(20	0.4250(2)	0.0007(1)	1.91(6)
Cl3	0.4575(2)	0.0744(2)	0.1623(1)	1.87(6)
La	2/3	1/3	1/4	1.47(3)
Cs	1/3	2/3	1/4	4.58(8)
Fe	0	0	0	1.60(5)

B_{22}	B_{33}	B_{12}	B_{13}	B_{23}	B_{eq}
1.18(2)	1.20(2)	0.59(2)	-0.07(2)	0.00(2)	1.17(2)
2.20(60	1.57(6)	1.22(5)	-0.57(5)	-0.77(5)	1.81(5)
0.99(5)	2.09(6)	0.62(4)	0.43(5)	0.11(4)	1.71(5)
2.35(6)	2.45(8)	1.06(6)	-0.92(5)	-0.44(6)	2.21(6)
B_{11}	1.34(4)	$1/2B_{11}$	0	0	1.43(3)
B_{11}	14.4(2)	$1/2B_{11}$	0	0	7.8(1)
B_{11}	1.74(8)	$1/2B_{11}$	0	0	1.64(5)

Table 15. Important Distances and Angles in $CsLaZr_6Cl_{18}Fe$

Distances (Å)						
Zr-Fe		x 6	2.3943(5)	La-Cl3	x 6	2.801(2)
Zr-Zr		x 6	3.391(1)			
		x 6	3.3813(9)			
	$\bar{d}$		3.386	Cs-Cl1	x 6	4.025(2)
Zr-Cl[i]	Zr-Cl1	x 6	2.557(2)	Cs-Cl3	x 6	3.842(2)
		x 6	2.568(2)	$\bar{d}$		3.934(3)
	Zr-Cl2	x 6	2.545(2)			
		x 6	2.549(2)			
	$\bar{d}$		2.555			
Zr-Cl[a]	Zr-Cl3	x 6	2.671(2)			
Angles (°)						
Zr-Cl1-Zr1			82.85(5)			
Zr-Cl2-Zr1			83.19(5)			
Fe-Zr-Cl3	177.39(6)					
Zr-Cl3-La	129.87(6)					
Cl3-La-Cl3	162.94(6), 90.34(6), 78.99(7)					

Structure description As implied by the formula, the principal structural elements in $CsLaZr_6Cl_{18}Fe$ are the cluster unit, and the two countercations, La^{3+} and Cs^+ (Figure 12). The 18 e^- cluster unit $[Zr_6Cl_{18}Fe]^{4-}$ has S_6 point symmetry. Although a trigonal compression of the otherwise perfect octahedral cluster core is observed, this distortion is almost negligible (the two Zr-Zr distances differ by 0.0097 Å, 9σ, 0.3%). The average Zr-Zr distance as well as the Zr-Fe distance are the shortest among those known in Fe cluster compounds (Zr-Fe: $Zr_6Cl_{14}Fe$ (ave.) 2.423 Å; $LiZr_6Cl_{15}Fe$, 2.424(1) Å; $KZr_6Cl_{15}Fe$ (ave.), 2.424 Å and 2.422 Å). Nevertheless, such a difference of 0.03 Å has been observed before for other systems, e.g., 14 e^- carbon clusters,[37] and therefore is not considered abnormal. The averaged Zr-Cl^i distance is so far the upper limit observed for Fe clusters, and it can be explained by the higher coordination numbers of the Cl atoms in this compound. Also, as expected, among the two Cl^i atoms in $CsLaZr_6Cl_{18}Fe$, the one with higher coordination number (Cl1, CN= 2(Zr) + 1(Cs); Cl2, CN= 2(Zr)) has longer Zr-Cl distances. Comparing the Zr-Cl^a in this compound with other $M_xM'Zr_6Cl_{18}Z$ phases, one clearly observes the trend that as the charge on M′ increases, the Cl^a-M′ interaction becomes stronger, and the Zr-Cl^a distance becomes longer (Zr-Cl^a: $(K,Ba)_2BaZr_6Cl_{18}C$, 2.619(1) Å; $K_2Zr_7Cl_{18}(H)$,[22] 2.770(2) Å, here 2.671(2) Å).

In $CsLaZr_6Cl_{18}Fe$, the M′ position is occupied by La^{3+}. It is still six-coordinate and connects to six cluster units through Cl^a as in the original double salt structure; yet, the coordination polyhedron is no longer trigonal antiprism (Figure 13). The twisting of the top and

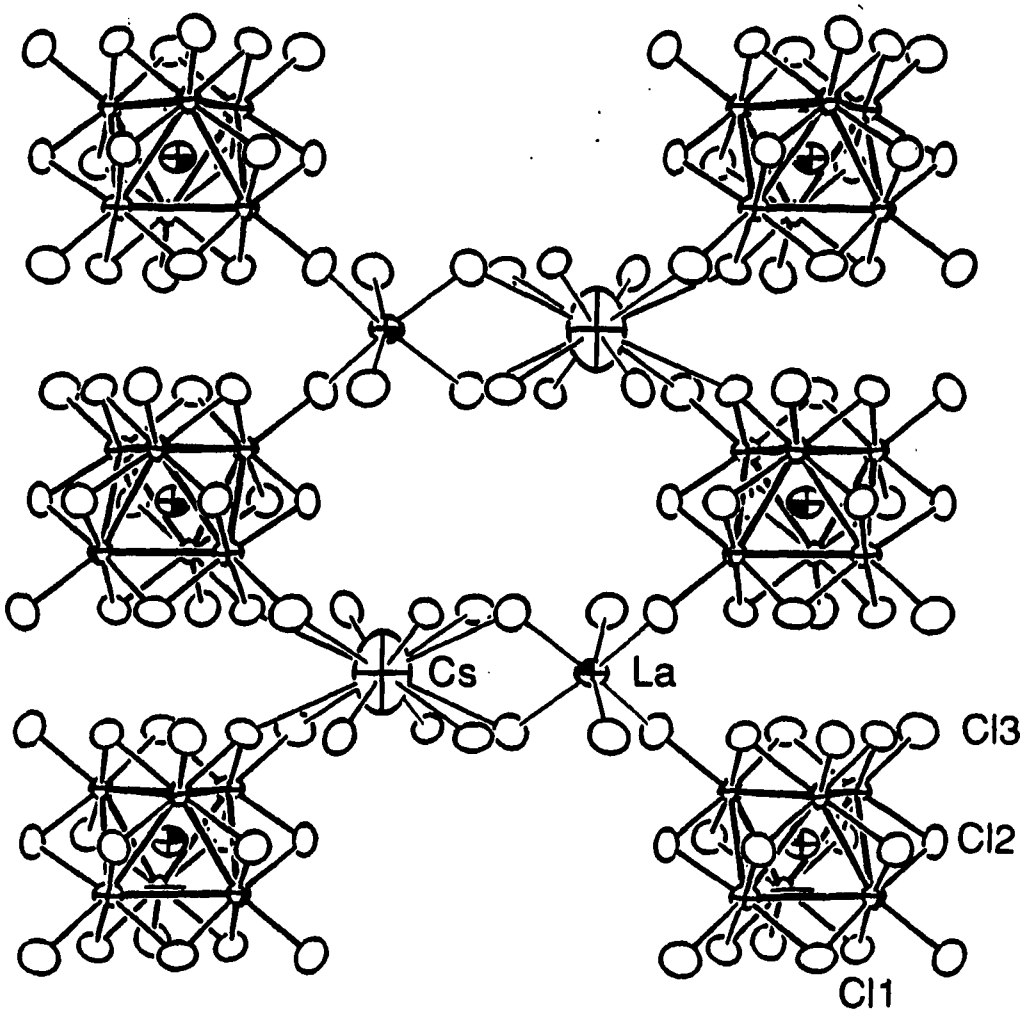

Figure 12. The [110] projection of $CsLaZr_6Cl_{18}Fe$ (90% probabilities, $\vec{c}$ vertical). The c-glide is perpendicular to the plane of the paper, passing through the center of each vertical column of clusters

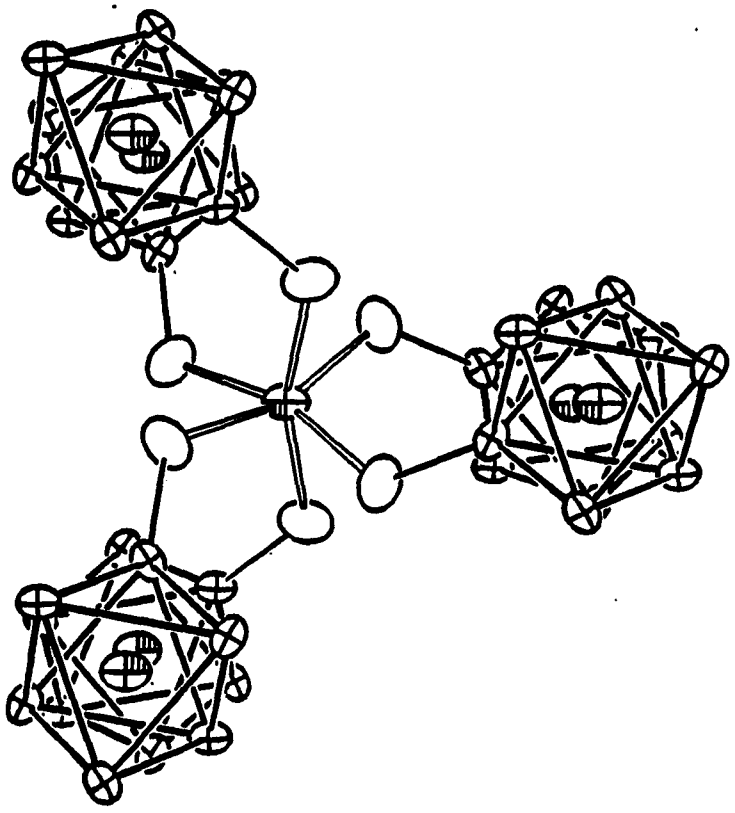

Figure 13. The La position in $CsLaZr_6Cl_{18}Fe$ and the cluster units around it (90% probabilities). It has D_3 symmetry with the principal axis perpendicular to the plane of the paper

bottom triangular faces around the 3-fold axis destroys the inversion center of the trigonal antiprism, and the point symmetry is reduced to D_3. The largest Cl3-La-Cl3 angle is now 162.92(6)° instead of 180° as in $(K,Ba)_2BaZr_6Cl_{18}C$; however, the La-Cl^a-Zr angle is changed only slightly and the Fe-Zr-Cl^a angle remains almost the same. These phenomena show that the structure changes from the $K_2Zr_7Cl_{18}(H)$ type to the $CsLuNb_6Cl_{18}$ type ($R\bar{3}$ to $P\bar{3}1c$) involve modifications of the M′ position, while leaving the cluster units intact and cluster connections preserved.

Contrary to the nature of the cluster unit and the M′ site, the coordination environment of M in the $P\bar{3}1c$ phase is completely different from that in $R\bar{3}$. Although the coordination number is still twelve, each Cs in $CsLaZr_6Cl_{18}Fe$ now has two 6-chlorine rings above and below it in its first coordination sphere, and the $CsCl_{12}$ group has D_3 point symmetry (Figure 14). The Cs atoms do not occupy positions within the close-packed layers as the K atoms did in the original double salt structure. Instead, they are now between layers of chlorines. The average Cs-Cl distance is over 0.2 Å larger than the sum of the crystal radii (Cs^+ CN=12, 2.02 Å; Cl^- 1.67 Å)[66] and this is because the structure framework does not allow the Cl atoms to arrange around Cs^+ freely. The size as well as shape of the Cs thermal ellipsoid reflects the size and anisotropy of this site. The two Cl_6 rings have a diameter of 7.17 Å, leaving large openings above and below the Cs atom. To complete its coordination sphere, Cs has two additional triangular fragments formed by Cl2 atoms at the Cs–Cl2 distances of 5.03 Å. As shown in Figure 14 these Cl2 atoms together with the two Cl_6 rings define the Cs

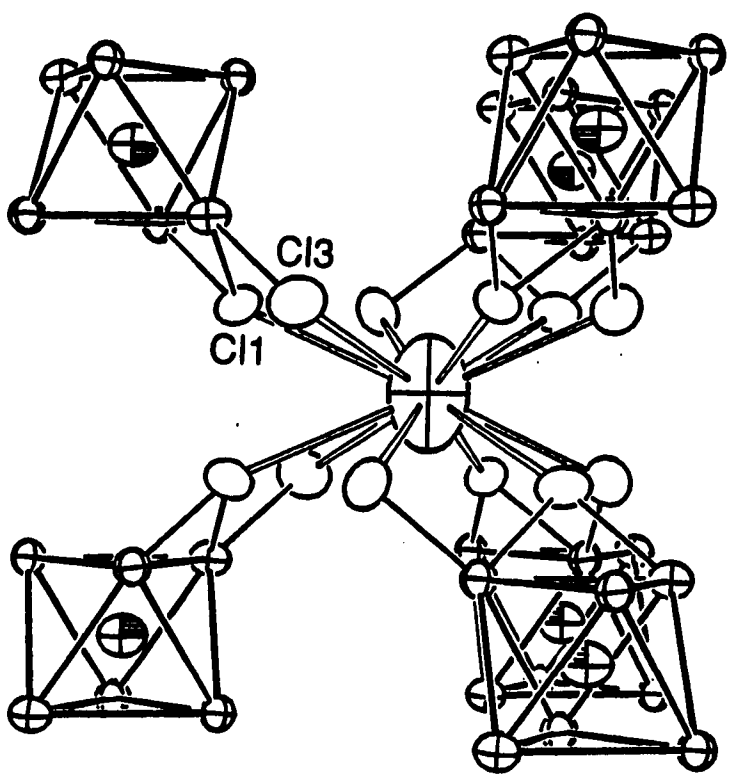

Figure 14. The Cs position in $CsLaZr_6Cl_{18}Fe$ (D_3 symmetry, 3-fold axis vertical) with the surrounding cluster units

coordination polyhedron that is elongated along the $\vec{c}$ axis. Taking these facts into consideration, the thermal parameters of Cs become acceptable.

As the structure transforms from $R\bar{3}$ to $P\bar{3}1c$ type, the close-packed layers are also changed. There are six close-packed layers perpendicular to $\vec{c}$ in each unit cell, while each cross-section still contains seven close-packing positions (7x6 per cell). Part of these positions are occupied by Cl atoms and Fe (2x(18Cl+Fe) per cell), and four sites located at the top and the bottom of each Cs atom are left empty. Comparing the six layers, it is found that the three layers around the clusters centered at z = 1/2 do not overlap with any layer around the clusters at z = 0. This is caused by the twisting of the cluster units around the 3-fold axis passing through La, which results in the misplacement by about 10° of the two sets of the close-packed layers that are now related by the c-glide. As a result, the layer sequence becomes (...CABC'A'B'...) where the prime denotes the 10° displacement. The spacing between the layers follows the same pattern (2.963 Å, 3.236 Å) as in $K_2BaZr_6Cl_{18}C$, except the cluster expansion pushes the layers around the same cluster slightly further apart. The closest chlorine neighbors in this structure are Cl1 and Cl3 (3.509(2) Å), which are pulled together by sharing the common Zr and Cs atoms.

$\underline{Ba_3Zr_6Cl_{18}Be}$

Previous research in area of synthesis and characterization of Zr-Cl clusters has led to the amazing discoveries of a family of compounds rich in solid state chemistry. These cluster phases exhibit diversities in chemical components, stoichiometries, and structure types.

Nevertheless, the earlier work was focused on the phases with alkali metals as the countercations, which was to a certain extent owing to the ease of obtaining crystals of reasonable quality from these systems for structure determinations. Expanding the variety of countercations naturally became one promising approach to the search for new cluster compounds. Efforts in this direction have been very fruitful, including the syntheses of two groups of 6-18 phases discussed in the above sections ($K_2ZrCl_6 \cdot Zr_6Cl_{12}H$ type and $CsLuNb_6Cl_{18}$ type) which contain alkali metals in addition to the alkaline-earth or rare-earth metal cations. However, when the alkali metal chlorides were completely excluded from the reaction systems, obstacles occurred which mainly arose from the technical difficulties in obtaining sizable single crystals for identifying unknown phases with new structure types. Similar problems seemed to affect the studies in the Nb-Cl systems, too, as the only available data on $Ba_2Nb_6Cl_{18}$, one of the first cluster compounds, is based on powder diffraction work.[69,70]

Compared with the alkali metal chlorides, the alkaline-earth metal chlorides have much higher melting points and lower vapor pressures under the chosen reaction conditions, which hinders crystallization via melts, fluxing, or vapor transport. To overcome these limitations, special procedures were taken to enhance crystal growth, for example, by increasing the reaction temperature (>900°C), applying a temperature gradient, or adding an extra component to the reaction system as a flux or a vapor transporting agent. Although their true mechanisms remain unverified, some of these treatments seem to be effective. To date, two new Ba-containing Zr-Cl cluster phases, $Ba_2Zr_6Cl_{17}B$[38] and $Ba_3Zr_6Cl_{18}Be$,

have been synthesized and structurally characterized via single crystal X-ray analyses. The significance of such successes is not only the identification of new compounds, but also the discovery of new structure types and specific structure features that reveal the relations behind the numerous cluster compounds. As for $Ba_3Zr_6Cl_{18}Be$, on one hand, it is a unique compound with a new 6-18 structure; on the other hand, it can be considered as a superstructure of the original double salt, $K_2ZrCl_6 \cdot Zr_6Cl_{18}H$, with a doubled $\vec{c}$ axis. With this additional example, the structural modifications obtained in connection with the size, charge and occupancy of the countercations may be systematically studied and better demonstrated.

Synthesis The existence of $Ba_3Zr_6Cl_{18}Be$ was first observed in the powder diffraction pattern of the product from a reaction designed to make $BaZr_6Cl_{14}Be$ (800°C, 20 days),[42] a 14-electron cluster phase that has not yet been synthesized. The presence of $Zr_6Cl_{12}Be$, the main product (~60%), and the absence of $BaCl_2$ indicated that the new and unidentified phase was rich in Ba. Therefore, efforts were made to increase the yield of the phase of interest, and it was observed that this phase became the dominant product when the $BaCl_2$:$Zr_6Cl_{12}Be$ ratio was higher that 2:1, in agreement with the stoichiometries of the two coexisting cluster compounds. The identity of this new phase remained unknown even though its yield could be increased. Its structure relationship with the double salt was at first not recognized from the powder pattern, because of numerous additional reflections caused by the doubling of the $\vec{c}$ axis, a shifting of the reflections resulted from lattice expansion, and a significant intensity redistribution due to

substituting K by a much heavier element, Ba. High temperature (900°C) or temperature gradient (800 - 900°C) reactions failed to provide single crystals. Yet, adding Hg_2Cl_2 to a reaction with starting stoichiometry of $BaZr_6Cl_{14}Be$ at 1:1 ratio greatly improved the crystallinity of the products. Considering the substantial vapor pressure of Hg_2Cl_2 or any other possible Hg-containing phases at elevated temperatures, the reaction temperature was chosen to be 700°C, and the reaction period was extended to 70 days. This showed that Hg_2Cl_2 or its derivatives are effective mineralizers for this system under study. From the powder pattern, neither a new phase nor any shift of the reflections from $Zr_6Cl_{12}Be$ or $Ba_3Zr_6Cl_{18}Be$ was observed, which allowed one to conclude that no Hg-containing cluster phases were formed. Instead, several drops of a metallic-looking melt were found in the product, possibly binary or ternary alloys between Hg and Zr or Ta. Besides the improved crystallization of the bulk product shown by the well defined lines of the cluster phases on the powder pattern, crystals with quality for single crystal X-ray diffraction were obtained.

Structure determination The structure of $Ba_3Zr_6Cl_{18}Be$ was determined via single crystal X-ray analysis using a crystal obtained as described above. The data collection was conducted on the RIGAKU diffractometer, and the structure refinement thereafter proceeded with the structure determination package TEXSAN.[60] The INDEX program gave a rhombohedral cell upon indexing 25 reflections located by SEARCH, and this cell was transferred by DELAUNAY to the hexagonal setting. The unusually large $\vec{c}$ axis of over 52 Å for the resulting R-center hexagonal cell seemed to be suspicious, since such phenomena could be caused by

including reflections from twin or multiple crystals. Yet, the singularity of the crystal was verified first by the profiles of the above 25 reflections, which were single peaks without splitting, and second by the clean axial photos that showed the expected spacings. Moreover, it was noticed that the dimensions of this unit cell could be related to those of the double salt $K_2ZrCl_6 \cdot Zr_6Cl_{12}H$ ($R\bar{3}$) by dividing its $\vec{c}$ axis by two. It was realized that this phase might have a superstructure of the double salt; however, to establish this structural relation and to determine the stoichiometry, a complete single crystal X-ray study was required.

The diffractometer was used to collect one quadrant of reflections in the obverse hexagonal setting after the Laue class, $R\bar{3}m$, was determined by program LAUE. Because of large cell dimensions of the hexagonal cell, the diffractometer was automatically switched from the ω-2θ scan to an ω scan for the better resolution of reflections that were close to each other in the reciprocal space. This required scan mode change was unnecessary because the extinction condition of R-centering eliminates two-thirds of the reflections ($-h+k+\ell \neq 3n$), leaving the rest well separated in the reciprocal space. Moreover, the ω scan mode seemed to cause error in intensity measurements, indicated by the failure of the standards refinement and the unreasonable intensity drop of these standard reflections that occurred after the beginning of the data collection. Re-centering the crystal as an effort to correct the asymmetrical profiles of the standards was a waste of time since the crystal was not moving. Apparently, this problem arose from the relatively narrow effective width of the ω scan, and the imperfect shape

of the diffraction spots from the crystal (the widths of the peaks were over 1°, about 0.2° larger than the typical value for similar crystal studies). Nevertheless, data collection in the primitive rhombohedral setting with an ω-2θ scan avoided these troubles, due to the particular scan direction and the increased scan width. One hemisphere of reflections was measured to assure full coverage of the reciprocal space and furnish sufficient unique reflections as well as redundant data for the standard hexagonal setting. Once the scan mode was changed, the data collection continued smoothly without abnormal observations.

The data were first processed by applying Lorentz and polarization corrections and an empirical absorption correction with three ψ-scan measurements. No decay correction was necessary. The data thus prepared were then transferred to the standard hexagonal setting for further studies. The additional extinction condition ($h\bar{h}0\ell$, ℓ=2n), in agreement with the Laue symmetry observed earlier, limited the possible space groups to $R\bar{3}c$ and R3c. $R\bar{3}c$ was chosen and later proven by successful refinement to be the correct space group. Following data averaging in the corresponding Laue class, SHELXS-86[58] was employed to provide the initial model. Successive refinements with least-square calculations and Fourier synthesis were successful, revealing all structural elements including the interstitial atom Be. The satisfactory refinements of the multiplicities of the two Ba sites and the Be position (Ba1, 101(4)%; Ba2, 99.5(4)%; Be, 110(9)%) suggested that there was no Hg in the lattice, consistent with the powder diffraction information. The final refinement was conducted on the model with fully occupied countercation and interstitial positions, resulting

in an essentially flat difference Fourier map, and an empirical formula of $Ba_3Zr_6Cl_{18}Be$ that gives a 14-electron count cluster. Other refinement parameters of importance are reported in Table 16, and the structure determination results are presented in Table 17 and Table 18, respectively.

Structure description According to their functions, there are three structure elements in $Ba_3Zr_6Cl_{18}Be$: the cluster unit $[Zr_6Cl_{18}Be]^{6-}$, the six-coordinate Ba1, and the 12-coordinate Ba2. The clusters arrange in a cubic close packed manner (Figure 15), with Ba1 and Ba2 occupying the octahedral and the tetrahedral vacancies between them, respectively.

The $[Zr_6Cl_{18}Be]^{6-}$ unit has the dimensions expected for a 14-electron Be-centered cluster.[37] The Zr_6 core possessing S_6 symmetry experiences a profound trigonal compression (Δ(Zr-Zr) = 0.045 Å, 45σ, 1%). The magnitude of this distortion is comparable to what is observed in $K_2ZrCl_6[Zr_6Cl_{12}H]$, but it is much more severe than those detected for the other cluster units with the same symmetry (Δ(Zr-Zr): $Li_6Zr_6CL_{18}H$, 0.012 Å; $(KBa)_2BaZr_6CL_{18}C$, 0.013 Å; $CsLaZr_6CL_{18}Fe$, 0.01 Å). A matrix effect is the only origin of this distortion as the cluster electron count is 14, and its amplitude is evidently associated with the strong field imposed by the Ba^{2+} ions on the cluster core. The repulsion between the Zr atoms and the Ba atoms (Ba1 and Ba2) that are located mainly on both sides of the cluster creates a constriction along the $\vec{c}$ axis (Figure 15), consequently leading to the observed cluster distortion. The Zr-Cl^i distances have the normal average for a 14-electron Be cluster. Although the two Cl^i atoms have the same number of cations in their first coordination sphere (2 Zr's and 1 Ba2), there is a sizable differ-

Table 16. Crystal Data for $Ba_3Zr_6Cl_{18}Be$

space group	$R\bar{3}c$ (No. 167)
Z	6
a, Å[a]	9.6852(9)
c, Å	52.52(1)
V, Å^3	4266(1)
crystal dimen, mm	0.16 x 0.16 x 0.16
data collection instrument	RIGAKU AFC6R
scan mode	ω-2θ
$2\theta_{max}$, deg	50
reflections	
measured	5197
observed ($I > 3\sigma$)	3281
observed independent	826
absorp coeff μ, cm^{-1} (Mo Kα)	79.2
range of transm coeff	0.83 - 1.00
R_{ave}, % ($I > 0$)	6.4
second ext coeff	1(2) x 10^{-9}
R,%	2.7
R_w,%	3.2
largest residue peak, e$^-$/Å^3	+1.0 (1 Å to Ba2); -1.3 (at Ba1)

[a]Guinier powder diffraction data (55 observations).

Table 17. Positional and Thermal Parameters for $Ba_3Zr_8Cl_{18}Be$

	x	y	z	B_{11}
Zr	0.20573(6)	0.01733(6)	0.02532(1)	0.78(2)
Cl1	0.2000(2)	0.2181(2)	0.05740(3)	1.56(6)
Cl2	0.1931(2)	0.4307(2)	0.00108(2)	0.85(6)
Cl3	0.4441(2)	0.0260(2)	0.05263(3)	1.70(6)
Ba1	0	0	1/4	1.52(2)
Ba2	0	0	0.38839(1)	1.95(2)
Be	0	0	0	0.9(4)

B_{22}	B_{33}	B_{12}	B_{13}	B_{23}	B_{eq}
0.99(2)	1.17(2)	0.47(2)	-0.13(2)	-0.01(2)	0.97(2)
1.53(6)	1.52(6)	0.75(5)	-0.07(4)	0.41(4)	1.55(5)
1.67(6)	2.19(6)	0.37(5)	-0.09(4)	0.39(4)	1.68(5)
2.04(6)	2.21(6)	1.11(6)	-0.78(5)	-0.40(5)	1.91(5)
B_{11}	2.44(4)	$1/2B_{11}$	0	0	1.82(2)
B_{11}	2.64(3)	$1/2B_{11}$	0	0	2.18(2)
B_{11}	1.0(6)	$1/2B_{11}$	0	0	0.9(4)

Table 18. Important Distances and Angles in $Ba_3Zr_6Cl_{18}Be$

Distances (Å)					
Zr-Be		x 6	2.3306(5)	Ba1-Cl3 x 6	3.113(1)
Zr-Zr		x 6	3.276(1)		
		x 6	3.3154(3)	Ba2-Cl1 x 3	3.497(2)
	$\bar{d}$		3.296	Ba2-Cl1 x 3	3.866(2)
Zr-Cl^i	Zr-Cl1	x 6	2.595(2)	Ba2-Cl2 x 3	3.464(2)
		x 6	2.598(1)	Ba2-Cl3 x 3	3.090(2)
	Zr-Cl2	x 6	2.549(1)	$\bar{d}$	3.479
		x 6	2.564(1)		
	$\bar{d}$		2.577		
Zr-Cl^a	Zr-Cl3	x 6	2.683(2)		
Angles (°)					
	Zr-Cl1-Zr		x 6	79.36(4)	
	Zr-Cl2-Zr		x 6	79.70(2)	
	Cl1-Zr-Cl2		x 6	168.52(5)	
			x 6	169.82(5)	

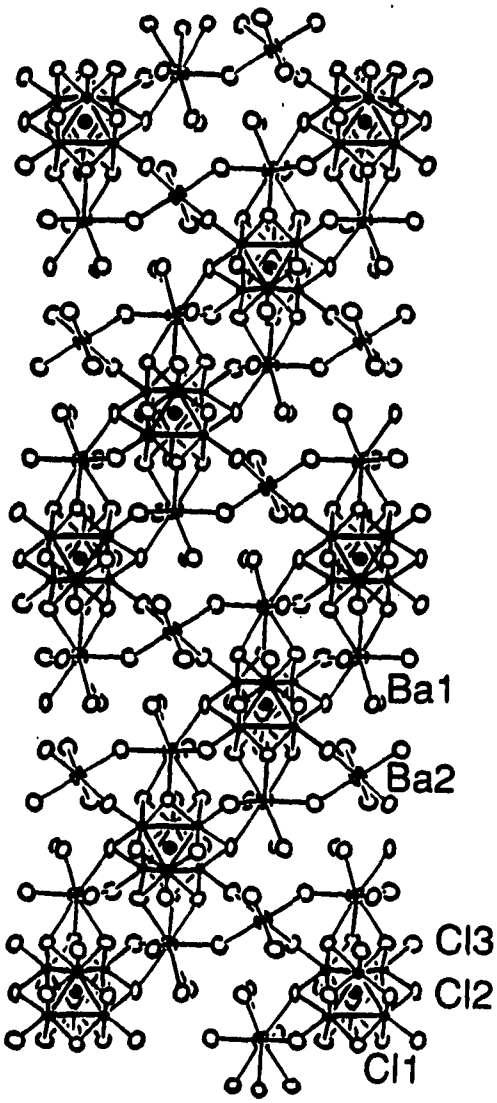

Figure 15. The [110] projection of $Ba_3Zr_6Cl_{18}Be$ with the $\vec{c}$ axis vertical (90% probability). The c-glide is in the plane of the paper, passing through the centers of the clusters

ence between Zr-Cl1 and Zr-Cl2, which is accounted for by the fact that Cl1 has two additional Ba^{2+} in its second coordination sphere (Cl1-Ba1 4.299(1) Å, Cl1-Ba2 3.866(2) Å), whereas the next nearest Ba neighbor of Cl2 is 4.860(2) Å away. Also, as the total field strength of the countercations increases, the Zr-Cl^a distance becomes relatively large in comparison to what is observed in $(K,Ba)_2BaZr_6Cl_{18}C$ (2.619(1) Å).

The second structure element Ba1 performs the same function as the Ba in $(K,Ba)_2BaZr_6Cl_{18}C$, i.e., connecting the cluster units into a three-dimensional network via their terminal Cl atoms. Although this Ba atom is still surrounded by six clusters in a pseudo octahedral manner, the $BaCl_8$ group distorts from a trigonal antiprism to a twisted trigonal prism (Figure 16). This fragment possesses D_3 symmetry, similar to the La position in $CsLaZr_6Cl_{18}Fe$. However, this distortion does not modify the packing of the clusters. In contrast to what observed in $CsLaZr_6Cl_{18}Fe$, the cubic close packing array of the cluster units in the double salt structure is preserved in $Ba_3Zr_6Cl_{18}Be$. When the twisting of the $BaCl_6$ unit occurs, each cluster unit rotates around the 3-fold axis passing through its center in fixed position. During this process, the cluster unit behaves as a rigid body. The Be-Zr-Cl3 angle remains close to 180° (176.77(5)°), whereas the largest Cl3-Ba1-Cl3 angle is reduced from 180° to 155.23(8)°. As the consequence of the twisting, the cluster units in two adjacent, close packed cluster layers that are parallel to the (110) plane no longer have the same orientation; instead, they are now related to each other by the c-glide along the $\vec{a} + \vec{b}$ direction. Also, because of the distortion of the coordination environment, the Ba-Cl distance (3.113(1) Å) becomes longer than that in

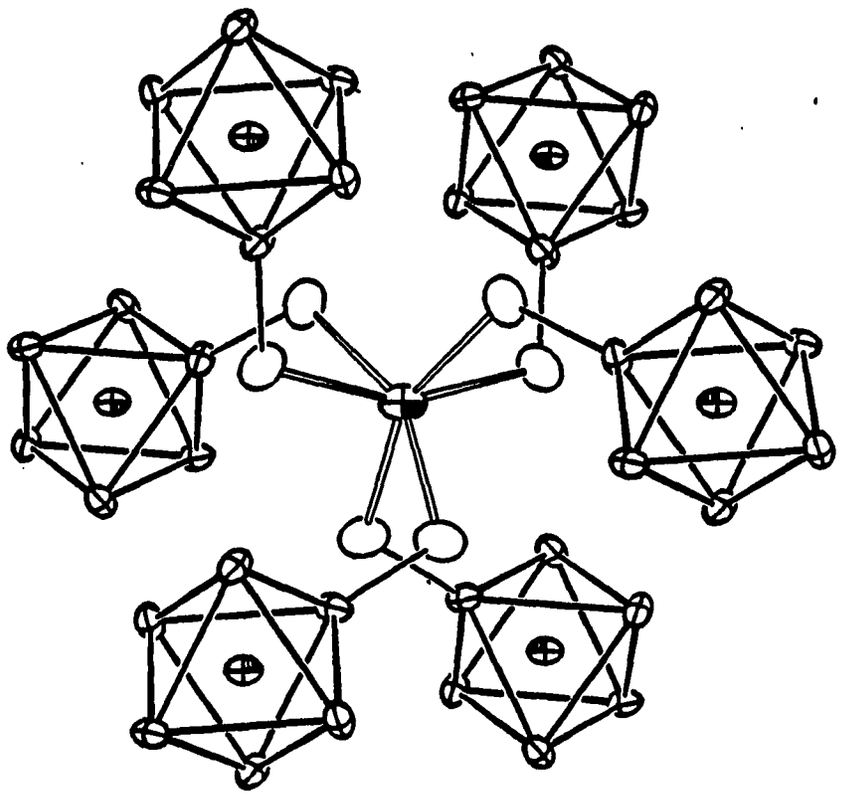

Figure 16. The coordination polyhedron of Ba1 in $Ba_3Zr_6Cl_{18}Be$ with the surrounding cluster units. Ba1 possesses D_3 symmetry (the 3-fold axis perpendicular to the plane of the paper, 90% probability)

$(K,Ba)_2BaZr_6Cl_{18}C$ (3.06512(6) Å), in better agreement with the summation of the crystal radii (Ba^{2+} CN=6 1.49 Å, Cl^- 1.67 Å).[66]

The other countercation position in this structure is occupied by Ba2 atom. It has very similar environment as the mixed cation in $(K,Ba)_2BaZr_6Cl_{18}C$. It is located within a close packed layer, surrounded by four cluster units in a pseudo tetrahedron fashion, and has C_3 point symmetry (Figure 17). Its coordination polyhedron involves three chlorine layers: two layers from the three clusters below it and one layer from the cluster above it. Because of the repulsions between the Ba and Zr atoms, Ba2 is 0.13 Å off the plane defined by the six chlorines atoms around its waist. Nevertheless, the increase of the cation field strength induces significant modification of this cation site. First of all, the strong attraction between Ba and Cl atoms causes contraction of the coordination polyhedron. Yet, if an isotropic contraction of the (K,Ba) site in $(K,Ba)_2BaZr_6Cl_{18}C$ occurred, the neighboring Cl atoms would be brought closer with a significantly stronger repulsion between them. To release this tension, the Cl1 atoms around the waist of Ba2 move away, while the Cl3-Ba2 distance becomes much shorter. This distortion makes the average Ba2-Cl distance (3.479 Å) deviate noticeably from the values estimated from crystal radii (Ba (CN=9) 1.61 Å, (CN=12) 1.75 Å; Cl 1.67 Å)[66] and also causes ambiguity in assigning the coordination number. The other consequence of the contraction is that, in comparison to the situation in $K_2ZrCl_6 \cdot Zr_6Cl_{12}H$, the Cl1 atoms from one cluster layer are rotated with respect to the other two Cl layers. This avoids the close contact between Cl1 and Cl3 which already has a close Cl neighbor (Cl3-Cl2, 3.404 Å). Although this

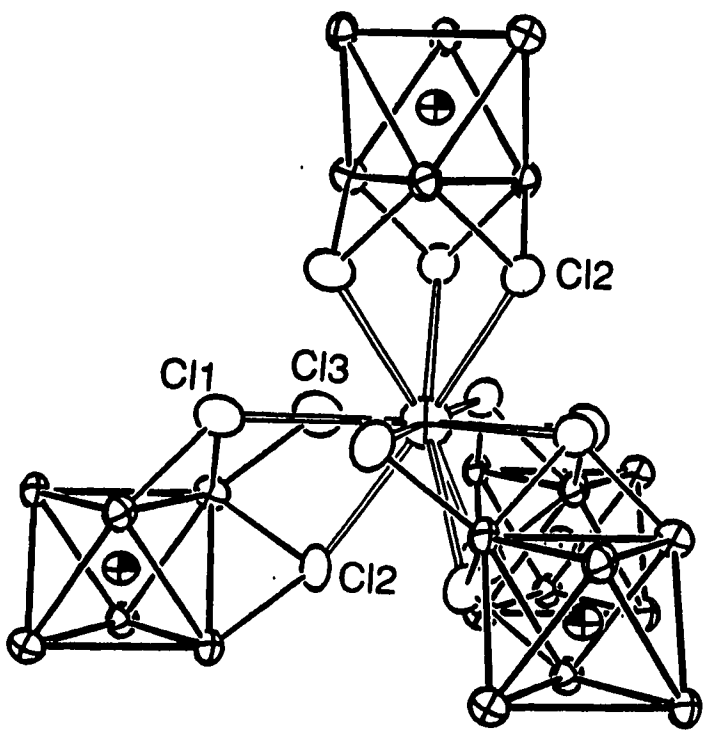

Figure 17. The coordination environment of Ba2 in $Ba_3Zr_6Cl_{18}Be$ with C_3 symmetry (3-fold axis vertical, 90% probability)

rotation occurs at the cost of bringing pairs of Cl1 atoms closer (Cl1-Cl1 3.340 Å), apparently it is more favorable in total lattice energy than simply adopting the original double salt structure, and the modifications of the Ba2 position are the main cause for the superstructure.

As with many other 6-18 clusters, the structure of $Ba_3Zr_6Cl_{18}Be$ is composed of close packed layers dominated by Cl atoms and also close packed cluster layers, both stacking along the $\vec{c}$ axis (Figure 15). Since the field strength of the countercation is greatly increased relative to $(K,Ba)_2BaZr_6Cl_{18}C$, the separations between the Cl layers approach equality (3.0(1) Å between two cluster layers vs 2.9(1) Å within a cluster layer). The packing sequence of the cluster units is still cubic close packed, except there are two repeating units in one unit cell (...ABCABC...). However, since the two adjacent cluster layers are not associated with each other by the R-centering, the cubic close packing pattern of the Cl sublattice is confined to only within one single cluster layer, as opposed to extending throughout the entire structure in the original double salt.[22]

The relations between the structure of $(K,Ba)_2BaZr_6Cl_{18}C$, $CsLaZr_6Cl_{18}Fe$ and $Ba_3Zr_6Cl_{18}Be$

The three 6-18 structures under discussion are closely related. They all can be represented by the general formula $M_xM'Zr_6Cl_{18}Z$, and the main structural framework is constructed with isolated $Zr_6Cl_{18}Z$ units linked via the countercation M'. A second countercation M fills the space left by the other two structural elements, at the same time

contributing electrons to stabilize the zirconium clusters. On the other hand, these structures are significantly different in terms of the packing of the cluster units and the coordination environment of the countercation positions. The structure variations are attributed to the modifications of the countercation M site. Without being directly involved in the main structure network, the coordination polyhedra of the countercation M are more flexible and more sensitive to the changes in its occupancy, size and charge.

The structure of $CsLaZr_6Cl_{18}Fe$ ($CsLuNb_6Cl_{18}$ type)[43] can be derived from that of $(K,Ba)_2BaZr_6Cl_{18}C$ ($K_2ZrCl_6 \cdot Zr_6Cl_{12}H$ type)[22] by merging the two adjacent M sites through a twisting of the cluster layers. The cause of this modification is the tendency for a large cation M (M = Rb, Cs) to occupy one large vacancy instead of being randomly distributed over two 50% occupied positions. With a three-dimensional framework and high efficiency of space filling, the entire structure responds to the adjustment of the M site. Figure 18 shows that while the two nearby M atoms line up along the $\vec{c}$ direction and eventually become one by moving toward each other, their neighboring Cl atoms have to be rearranged. This is accomplished by rotating the two cluster layers involved, and this rotation leads to the twisting of the other countercation coordination polyhedron. This structural transition from the $K_2ZrCl_6 \cdot Zr_6Cl_{12}H$ type to the $CsLuNb_6Cl_{18}$ type reduces the M/cluster ratio from 2 to 1, distorts the geometry of the MCl_6 group from trigonal antiprismatic to twisted trigonal prismatic, and changes the cluster packing sequence from (...ABC...) to (...AA...).

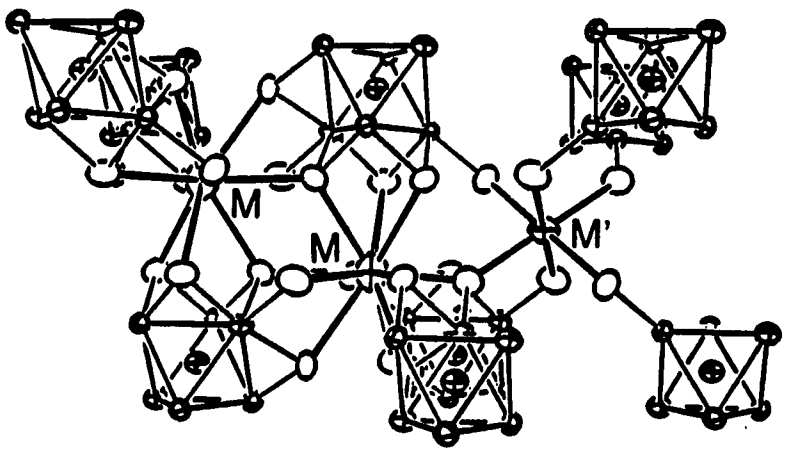

$R\bar{3}$ (M = (K,Ba), M' = La)

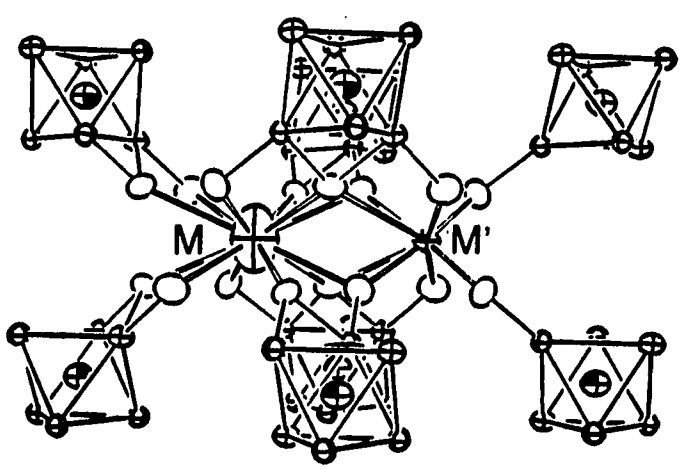

$P\bar{3}1c$ (M = Cs, M' = La)

Figure 18. The structure relation between the $K_2ZrCl_6 \cdot Zr_6Cl_{12}H$-type ($R\bar{3}$) and the $CsLuNb_6Cl_{18}$-type ($P\bar{3}1c$)

The charge of the countercation M is another source of structural modifications. For the structure types discussed above, the M position is occupied by alkali metals regardless of their size and occupancy. When the field strength of the cation on this position is increased by filling it with an alkaline-earth metal, another structure type in this series, the $Ba_3Zr_6Cl_{18}Be$ type, results. The structure modification also appears mainly around the countercation M, involving the three Cl layers. In response to the contraction of the coordination polyhedron, necessary modifications occur in order to reduce the repulsions between Cl atoms that come closer. In contrast to the structure change described above, the close packed cluster array is preserved in $Ba_3Zr_6Cl_{18}Be$. Therefore, the Cl atoms (Cl1) from a different cluster layer have greater degree of freedom to move than the other two Cl layers that are fixed to a certain extent by the common cluster layer in which they reside. Although the rotation of the Cl1 atoms with respect to the other two Cl layers does not reduce the total number of Cl close contacts around this position, it makes the repulsion become evenly distributed, contrary to being concentrated on one group of Cl atoms (Cl3) as it would happen if the original double salt structure were adopted (Figure 19, Table 19). This structure modification involves only the rotations of the cluster units with respect to their centers, and therefore most structure features of the double salt structure are preserved, including the packing sequence of the cluster units, the location and the number of the counter cations M. However, the orientations of the cluster units in the neighboring layers are no longer the same, and the range of the Cl close packing is now confined

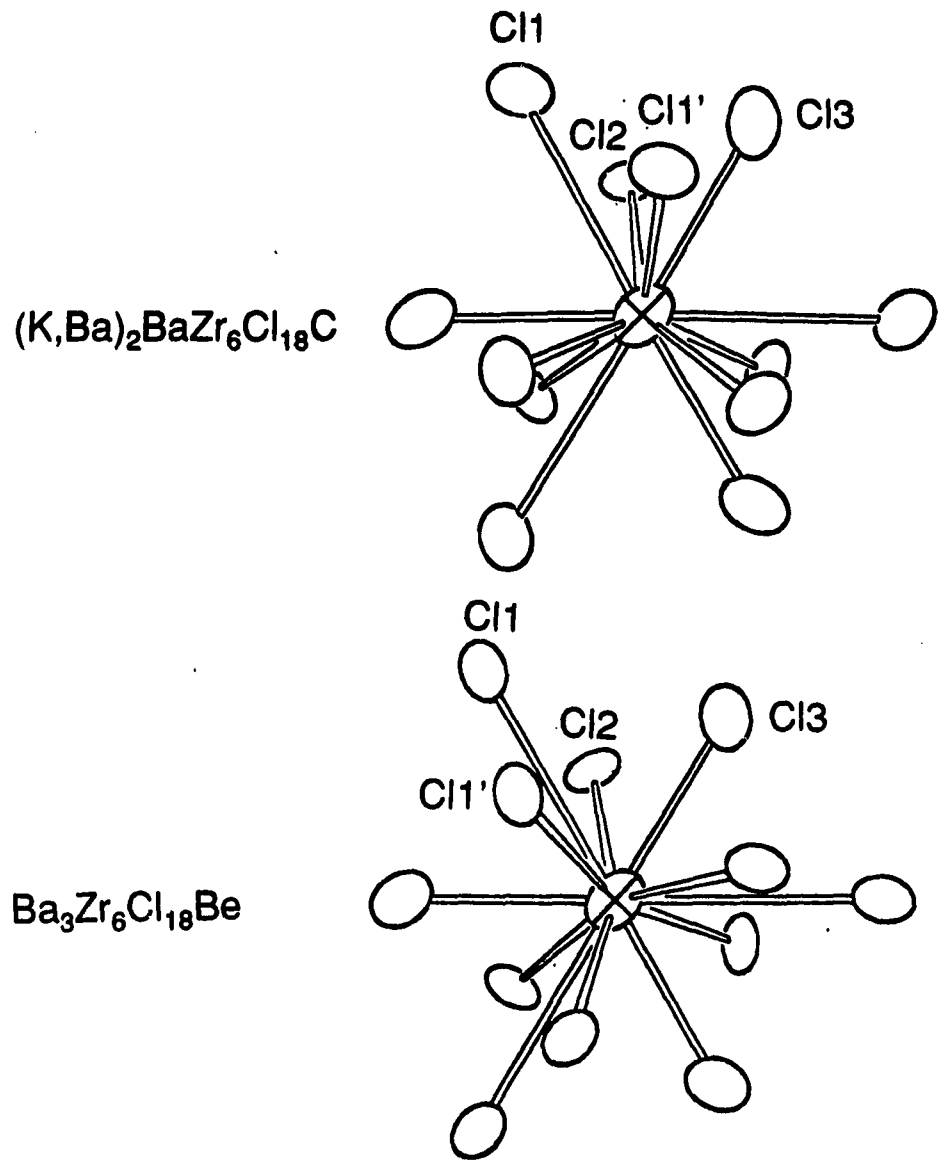

Figure 19. The comparison between the 12-coordinate positions in $(K,Ba)_2BaZr_6Cl_{18}C$ ($R\bar{3}$) and $Ba_3Zr_6Cl_{18}Be$ ($R\bar{3}c$) (the 3-fold axis perpendicular to the plane of the paper)

Table 19. The Comparison between the 12-coordinate Positions (M) in $(K,Ba)_2BaZr_6Cl_{18}C$ and $Ba_3Zr_6Cl_{18}Be$

	$(K,Ba)_2BaZr_6Cl_{18}C$	$Ba_3Zr_6Cl_{18}Be$
M	$K_{0.85}Ba_{0.13}$	Ba
M–Cl1	3.7624 (6)	3.866 (2)
M–Cl1′	3.632 (1)	3.497 (2)
M–Cl2	3.646 (1)	3.464 (2)
M–Cl3	3.2160 (6)	3.090 (2)
Cl1–Cl3	3.425 (2), 3.531 (2)	3.514 (3), 3.584 (2)
Cl1′–Cl1	3.940 (3)	3.340 (4)
Cl1′–Cl3	3.572 (2)	3.371 (2)
Cl2–Cl1	3.585 (2)	3.623 (2)
Cl2–Cl3	3.397 (2)	3.404 (2)

to one cluster layer. The instability thus introduced apparently is overcome by the increased lattice energy from the stronger interaction between the Ba and Cl atoms.

Since both $(K,Ba)_2BaZr_6Cl_{18}C$ ($R\bar{3}$) and $Ba_3Zr_6Cl_{18}Be$ ($R\bar{3}c$) are known, it seems plausible that another 14-electron cluster $KBa_2Zr_6Cl_{18}B$ should also exist. As a compound with an intermediate composition, the main structure framework of the above two phases should be preserved in this structure, and one of the two Ba would still be six-coordinate. The structure of $KBa_2Zr_6Cl_{18}$ will depend basically on the distribution and coordination of the rest of the countercations, one K^+ and one Ba^{2+}. There are three possibilities. First of all, because they have similar crystal radii (CN=12: K^+ 1.78 Å, Ba^{2+} 1.75 Å),[66] it is likely that K and Ba randomly occupy the same position, forming a mixed cation as observed in $(K,Ba)_2BaZr_6Cl_{18}C$. If this situation occurs, the phase should have either the $R\bar{3}$ structure or the $R\bar{3}c$ structure, depending on the relative field strengths of the mixed cations. Secondly, it is also possible that K^+ and Ba^{2+} choose separate sites due to the difference in their charges. If this happens, a new modification of the original double salt structure may be observed. Finally, combining the above two possibilities, the ordering of the K and Ba could be a function of the experiment conditions. The transition involving different degrees of such ordering could be first order, second order, or irreversible as in the case of $CsLaZr_6Cl_{18}Fe$. Although the investigation process might be complicated and technical problems might be encountered, it is worthwhile to examine a system that provides these intriguing

possibilities. The observations thus obtained will be valuable for understanding similar systems.

The above examples demonstrate one of the many factors that are responsible for the structure diversities in the centered Zr-Cl cluster systems. The ability of the cluster phase to accommodate a variety of countercations and the specific structural requirements of these cations may lead to many structurally related phenomenon, such as the formation of a new structure type, a transition between phases with different structures, or a slight modification that results in a superstructure. Unlike the other structure changes, the relationship between this group of structure types is very close. This also implies the unlimited possibilities of the structural chemistry of these systems when other factors and variables are taken into consideration.

Zr_6Cl_{17} Type

$Ba_2Zr_6Cl_{17}B$ and other compounds of this structure type[38]

Previous research in the centered Zr–Cl cluster systems provided numerous new cluster phases that exhibit wide stoichiometries and novel structure features. These discoveries marked the beginning of a new era when the systematic investigations of the structural cluster chemistry became possible. As knowledge about the cluster systems grew with each individual success of synthesis and characterization, it becomes clear that the cluster compounds could be classified according to the connectivities between the cluster units. Although the number of the known Zr–Cl cluster phases is exceptionally large, and their compositions and structures may appear to be very different, this

classification helps to organize them in a rational manner. More important, it also predicted compounds with specific structure characteristics that were yet to be discovered, namely, the $Zr_6Cl_{17}Z$ phases. In fact, the 6–17 compounds with the cluster connectivity of $[Zr_6Cl^i_{12}Z]Cl^a_4Cl^{a-a}_{2/2}$ were the missing link in the $[Zr_6Cl_{12}Z]Cl_n$ ($0 \leq n \leq 6$) series. Nevertheless, the establishment of this new structure type relied on the successful synthesis and characterization. Interestingly, $Ba_2Zr_6Cl_{17}B$ had been synthesized as early as the corresponding cluster connectivity was predicted, if not earlier. However, its identity remained unknown, again due to the technical difficulties of obtaining qualified single crystals for X-ray diffraction. As the first 6–17 cluster and the first Zr–Cl cluster phase containing only alkaline-earth-metal countercations, the final success in determining the structure and stoichiometry of $Ba_2Zr_6Cl_{17}B$ completed the $[Zr_6Cl_{12}Z]Cl_n$ series and opened new composition possibilities of Zr–Cl clusters. In addition, it emphasized the value of persistent efforts in synthetic chemistry, and also demonstrated the importance of the structure chemistry which reveals the relationships between the large number of cluster compounds.

Synthesis The first evidence of the existence of $Ba_2Zr_6Cl_{17}B$ can be dated back to June 1984, when the synthesis of the hypothetical $BaZr_6Cl_{15}B$ was attempted.[37] The powder diffraction pattern showed that the product contained $Zr_6Cl_{14}B$ and $Ba_2Zr_6Cl_{17}B$[42] which was unidentified. The same result was repeatedly observed later from similar reactions, and when extra $BaCl_2$ was added to the starting materials as an effort to enhance crystal growth ($BaCl_2$:$BaZr_6Cl_{15}B$, 1:1), $Zr_6Cl_{14}B$ was eliminated

from the product. Yet, it took almost three years to identify this new phase, simply because the lack of crystals adequate for single crystal X-ray structure determination. Although deep red transparent needles were often found in the products, they were either too small or grew together as loosely bound needles that were impossible to separate. As a desperate attempt to obtain crystals of higher quality after several failures, the products from foregoing reactions were resealed into a tantalum tube about 10 cm long, and heated at unusually high temperatures (1080 – 920°C gradient, 20 days), hoping the temperature and the large gradient might improve the crystallinity of the product. As expected, the selected conditions were too extreme, yielding a rather simple powder pattern that showed lines of $ZrClO_x$ and a few other unidentified lines without showing the presence of the desired phase. However, a few (<5%) well faceted crystals were indeed obtained, and despite the discouraging results from the powder diffraction, these crystals were saved for single crystal study which eventually led to the characterization of $Ba_2Zr_6Cl_{17}B$.

After the stoichiometry of the barium-containing compound was determined by single crystal study, reactions were loaded to synthesize more 6-17 phases. The output of the first attempt was somewhat unexpected, though not completely surprising. The only cause that could be related to the absence of $Ba_2Zr_6Cl_{17}B$ was the use of crystalline instead of amorphous boron as the interstitial source. Repeating this reaction (800–850°C, 30 days) with amorphous boron (particle size <1 μm) yielded $Ba_2Zr_6Cl_{17}B$ (>95%) in the form of a reddish black powder and a trace of $Zr_6Cl_{14}B$. Under similar conditions, two other 6-17 phases,

namely, $Ba_2Zr_6Cl_{17}Mn$ and $BaSrZr_6Cl_{17}B$, were produced in high yield (>95%). Comparing the cell parameters (Table 20), one observes on one hand the significant lattice expansion when Mn replaces B as the interstitial atom (28 $Å^3$ per cluster), which is similar to that known for the same change in the $MZr_6Cl_{14}Z$ series (27 $Å^3$ per cluster, $CsZr_6I_{14}C$ structure type,[16,24] M=K, Rb, Cs); on the other hand, the anisotropic cell parameter variation associated with the partial substitution of Ba by Sr seems puzzling. While the cell volume remains almost the same, $BaSrZr_6Cl_{17}B$ shows a slight expansion along $\vec{a}$ and a slight contraction along $\vec{c}$. The cell could not be better represented by a lattice with symmetries lower than tetragonal, and the high yield of the 6-17 phase implied that it was unlikely that the product is a phase with partial occupied cation site rather than the designed 14 e^- phase. It became acceptable later when the coordination environment of the cation position in $Ba_2Zr_6Cl_{17}B$ is examined (see structure description). In addition, the $\vec{c}$ parameters of the above three phases, which corresponding to the linear chain direction, agree with the value expected for linear cluster connectivity for B and Mn centered clusters [$CsKZr_6Cl_{15}B$, $\underline{c}$ = 9.731(2); $LiZr_6Cl_{15}Mn$, $\underline{a}$ = 10.3459(4)].

Complete substitution of Ba with Sr or Ca in 6–17 systems was not successful, presumably due to the small sizes of the cations, and replacing B with C to prepare $Ba_2Zr_6Cl_{17}C$ only led to the formation of the nonbarium-containing 14 e^- cluster phase, $Zr_6Cl_{14}C$. When one Ba was changed to a monovalent cation in order to balance the electron count ($KBaZr_6Cl_{17}C$, $CsBaZr_6Cl_{18}Fe$), 6–18 compounds of the $K_2ZrCl_6 \cdot Zr_6Cl_{18}(H)$ type were obtained for both C and Fe interstitials.

Table 20. Cell Parameters (Å) and Volumes (Å^3) for the $Ba_2Zr_6Cl_{17}B$-Types Compounds[a] (space group I4/m)

Compound	a	c	V
$Ba_2Zr_6Cl_{17}B$	11.4735(4)	9.8812(5)	1300.8(1)
$BaSrZr_6Cl_{17}B$	11.4944(4)	9.8534(4)	1301.85(8)
$Ba_2Zr_6Cl_{17}Mn$	11.6026(6)	10.0745(7)	1356.2(1)

[a]All values are Guinier powder diffraction data.

Structure determination The $Ba_2Zr_6Cl_{17}B$ crystal used for structure determination was obtained as described above. Although the yield of the desired product was no more than 5%, the quality of the crystals was exceptionally high. The crystals have rod-like shapes with regular faces, reasonable size, and are deep red under transmitted light which is characteristic for most zirconium chloride cluster compounds. A single crystal selected by preliminary oscillation photos was indexed on a CAD-4 diffractometer to have a body centered tetragonal cell, which had not been observed previously for zirconium chloride cluster systems. Axial photos about the three principal axes showed that only the $\vec{c}$ axis had a mirror plane perpendicular to it, and a photograph about the [111] direction confirmed the body centering. Hence, the Laue group was I4/m. Two octants of data were collected up to 2θ of 65° with the centering reflection condition applied ($h+k+\ell=2n$). Six ψ-scans were measured for the empirical absorption correction. Other important crystal data are listed in Table 21.

No additional extinction condition was observed after the intensities of the reflections were examined, which left I4, $I\bar{4}$ and I4/m as possible space groups. As no decay correction was necessary (net intensity change +0.3%), the two sets of redundant data were averaged for Laue class I4/m after the empirical absorption correction was applied. Then SHELXS-86 was employed to provide initial models for the three possible space groups, and since the solution for the centrosymmetric space group was clearly more reasonable in terms of distances and peak heights, space group I4/m and the corresponding solution were selected. The rough model from direct methods was refined toward

Table 21. Crystal Data for $Ba_2Zr_6Cl_{17}B$

space group	I4/m (No. 87)
Z	2
a, Å[a]	11.4735(4)
c, Å	8.8812(5)
V, Å^3	1300.8(1)
crystal dimen, mm	0.36 x 0.10 x 0.10
data collection instrument	ENRAF NONIUS CAD4
scan mode	ω-2θ
$2\theta_{max}$, deg	65
reflections	h, k, $\pm\ell$
measured	2566
observed	2280
observed independent	1247
absorp coeff μ, cm^{-1} (Mo Kα)	70.2
range of transm coeff	0.78 - 1.00
R_{ave}, %	2.0
second ext coeff	6.0(2) x 10^{-7}
R,%	1.7
R_w,%	2.5
largest residue peak, e$^-$/Å^3	+0.7 (0.7 Å, Ba) -1.4 (0 Å, Ba)

[a]Guinier powder diffraction data (72 observations).

completion by using standard least-square, full matrix calculations and Fourier syntheses, and as expected, an electron residue was found in the center of the Zr_6 unit after the heavier atoms were located. At the final stage of the structure determination, the occupancies of both Ba and B were studied by varying their multiplicities and thermal parameters simultaneously, leading to a 101.7(4)% occupied Ba position and 88(2)% occupied B position. Combining the fact that the Ba site is not significantly different from fully occupied and the cluster is expected to have 14 e^- count, these two positions were fixed at 100% occupancies in the final refinement, corresponding to the formula of $Ba_2Zr_6Cl_{17}B$. The positional and thermal parameters are listed in Table 22, and the important distances and angles calculated with lattice constants from powder diffraction data are reported in Table 23.

Structure description $Ba_2Zr_6Cl_{17}B$, as all other zirconium chloride cluster compounds, contains discrete $[Zr_6Cl_{12}B]$ cluster units. Represented by the formula $Ba_2[Zr_6Cl_{12}{}^iB]Cl_4{}^aCl_{2/2}{}^{a-a}$, the compound has infinitive one-dimensional cluster chains along $\vec{c}$ axis (Figure 20), and these chains are bound to each other via Ba^{2+} ions (Figure 21). Similar to that in Nb_6F_{15} structure,[17] the connections between clusters at Cl^{a-a} are linear, and the cluster chains along the cell edges (0,0,z) and those passing the centers (1/2,1/2,0) belong to two separate and identical networks. However, these linear connections are now one dimensional instead of three dimensional in Nb_6F_{15}. The loss of the cluster connectivities in $\vec{a}$ and $\vec{b}$ directions breaks down the cubic symmetry of Nb_6F_{15} to tetragonal, and each Cl^{a-a} atom formerly shared

Table 22. Positional and Thermal Parameters for $Ba_2Zr_6Cl_{17}B$

	x	y	z	B_{11}
Zr1	0.07181(2)	0.18658(2)	0	0.945(7)
Zr2	0	0	0.23442(3)	0.965(5)
Cl1	0.42077(4)	0.29165(4)	0.24444(4)	2.18(1)
Cl2	0.2862595)	0.12703(5)	0	0.97(2)
Cl3	0.14036(6)	0.40773(5)	0	1.90(2)
Cl4	0	0	1/2	3.31(4)
Ba	0	1/2	1/4	2.284(5)
B	0	0	0	0.86(8)

B_{22}	B_{33}	B_{12}	B_{13}	B_{23}	B_{eq}
0.703(6)	0.801(7)	-0.073(5)	0	0	0.816(3)
B_{11}	0.426(8)	0	0	0	0.785(3)
1.33(1)	0.92(1)	-0.35(1)	-0.15(1)	-0.27(1)	1.475(7)
1.28(2)	1.94(2)	-0.28(1)	0	0	1.397(9)
1.00(2)	1.76(2)	-0.39(2)	0	0	1.550(9)
B_{11}	0.51(3)	0	0	0	2.38(1)
B_{11}	1.233(7)	0	0	0	1.934(3)
B_{11}	0.5(1)	0	0	0	0.73(4)

Table 23. Important Distances and Angles in $Ba_2Zr_6Cl_{17}B$

Distances (Å)						
Zr-B	Zr1-B	x4	2.2938(2)	Ba-Cl1	x4	3.4680(5)
	Zr2-B	x2	2.3164(3)	Ba-CL2	x4	3.7738(4)
	$\bar{d}$		2.3013	Ba-CL3	x4	3.1332(4)
Zr-Zr	Zr1-Zr1	x4	3.2439(3)	$\bar{d}$(CN=8)		3.3006
	Zr1-Zr2	x8	3.2599(3)	$\bar{d}$(CN=12)		3.4583
	$\bar{d}$		3.2547			
Zr-Cl^{i}	Zr1-Cl1	x8	2.5389(4)			
	Zr1-Cl2	x4	2.5537(6)			
		x4	2.5519(6)			
	Zr2-Cl1	x8	2.5660(5)			
	$\bar{d}$		2.5526			
Zr-Cl^{a}	Zr1-Cl3	x4	2.6565(6)			
Zr-Cl^{a-a}	Zr2-Cl4	x2	2.6242(3)			
Angles (°)						
	Zr1-Cl1-Zr2	x8	79.37(2)			
	Zr1-Cl2-Zr1	x4	78.90(2)			
	Cl1-Zr1-Cl1	x4	168.07(2)			
	Cl2-Zr1-Cl2	x4	168.90(2)			
	Cl1-Zr2-Cl1	x4	170.67(2)			
	Cl3-Zr1-B	x4	176.17(2)			
	Cl1-Ba-Cl1	x2	178.19(1)			

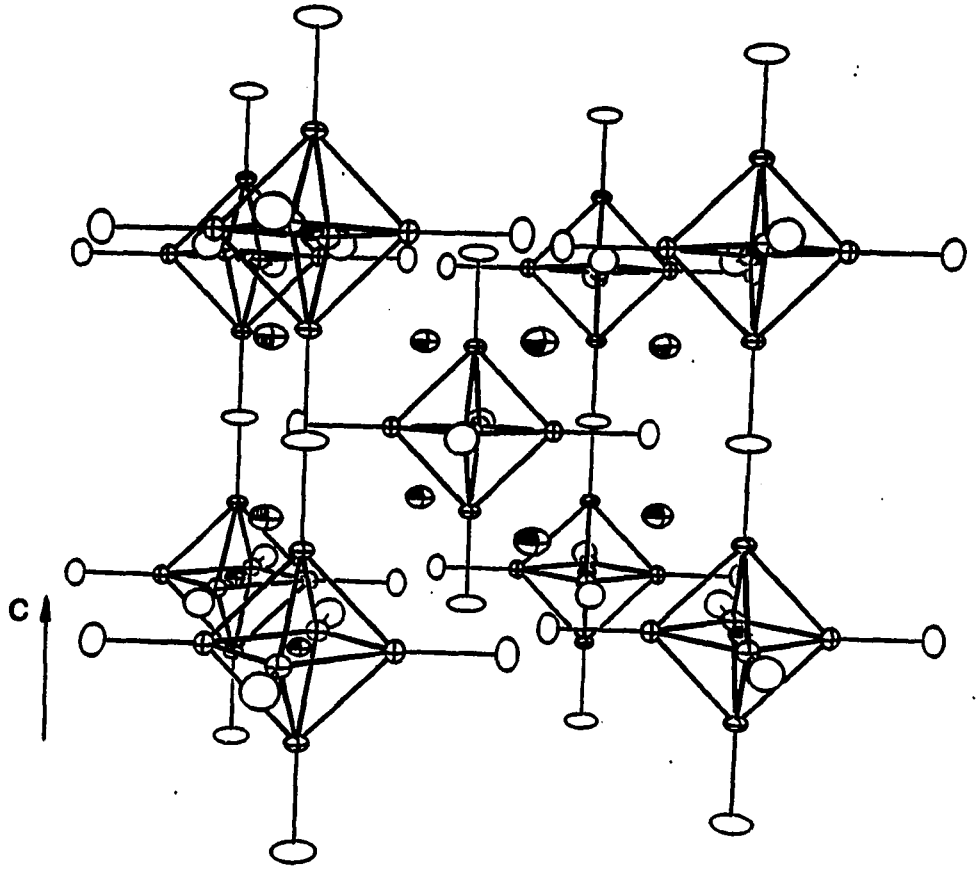

Figure 20. The unit cell view of $Ba_2Zr_6Cl_{17}B$ which shows the linear chains along c̄ axis (90% probability). The Cl^i atoms are omitted for clarity

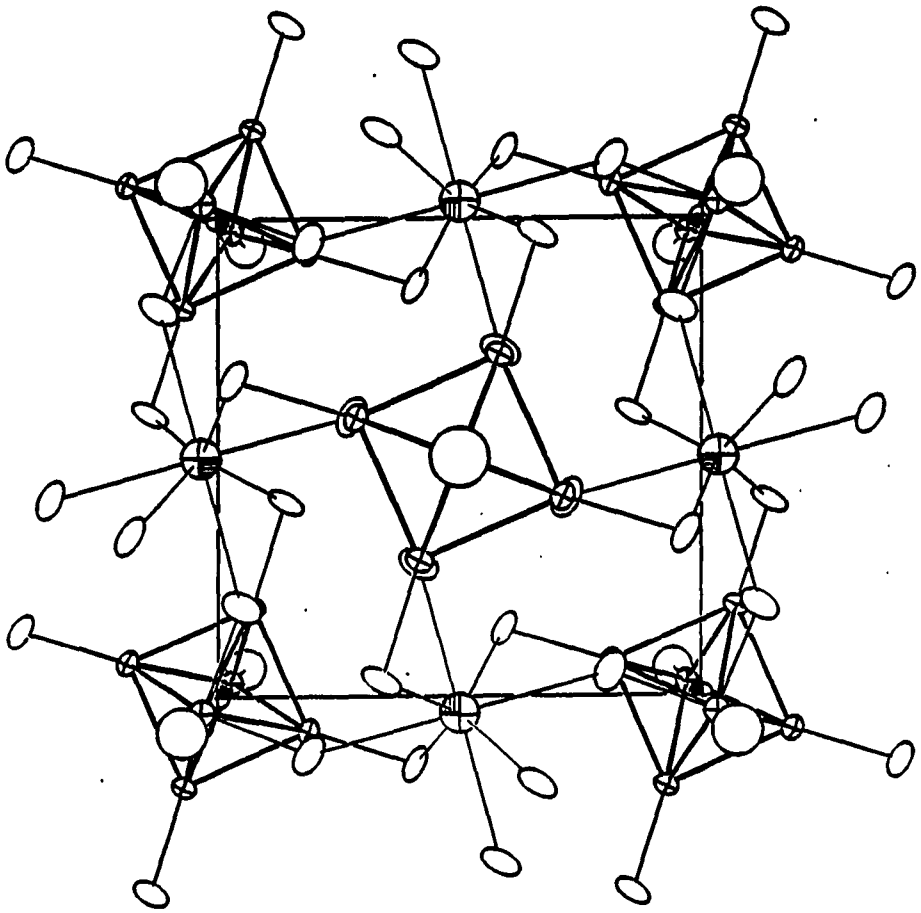

Figure 21. The [001] projection of $Ba_2Zr_6Cl_{17}B$ which shows the connections between cluster chains via Ba^{2+} ions (90% probability). The Cl^i atoms are omitted for clarity

between clusters along a and b directions in Nb_6F_{15} is now replaced by a pair of terminal Cl^a atoms normal to the chains.

The size of the $[Zr_6Cl_{12}B]Cl_6$ unit in $Ba_2Zr_6Cl_{17}B$ (Figure 22) is considered normal when compared with other boride clusters which have average Zr-B distances that range from 2.30 to 2.32 Å. It has C_{4h} point symmetry and undergoes slight tetragonal elongation (Zr-B distances differ by 0.0226(4) Å, 1%). Since it is a 14-electron cluster compound, this slight tetragonal distortion is considered as a result of the matrix effect associated with the incorporation of Ba^{2+}. While the apical Zr2 atoms are farther away from the Ba^{2+} (Zr2 – Ba, 5.7388(2) Å), each of the equatorial Zr1 atoms has two Ba^{2+} neighbors at a shorter distance (Zr1–Ba, 4.4399(2) Å). Therefore, the eight Ba cations around each cluster unit impose an anisotropic field which repels the Zr atoms on the waist of the cluster more effectively, resulting in the observed tetragonal elongation of the Zr_6 core. Also, because of the strong field of Ba^{2+}, the Zr-Cl^{a-a} distance is longer than that in the linear chains in $CsKZr_6Cl_{15}B$ (2.603 Å), which directly contributes to the larger c parameter of the barium salt than that in $CsKZr_6Cl_{15}B$ [9.812(5) Å vs 9.731(2) Å, both corresponding to twice the length of a (B–Zr–Cl^{a-a}) unit]. Another consequence of involving Ba^{2+} into the lattice is the unusual Zr–Cl^a distance which is over 0.03 Å longer than the Zr–Cl^{a-a} distance. This appears to be abnormal since for most of the known examples, Zr–Cl^a is shorter than Zr–Cl^{a-a}. However, by analyzing the environment of these two Cl's, one realizes that the longer Zr–Cl^a distance arises from the higher coordination number of Cl^a [1(Zr) + 2(Ba)] vs Cl^{a-a} [2(Zr)] and the stronger total effective field

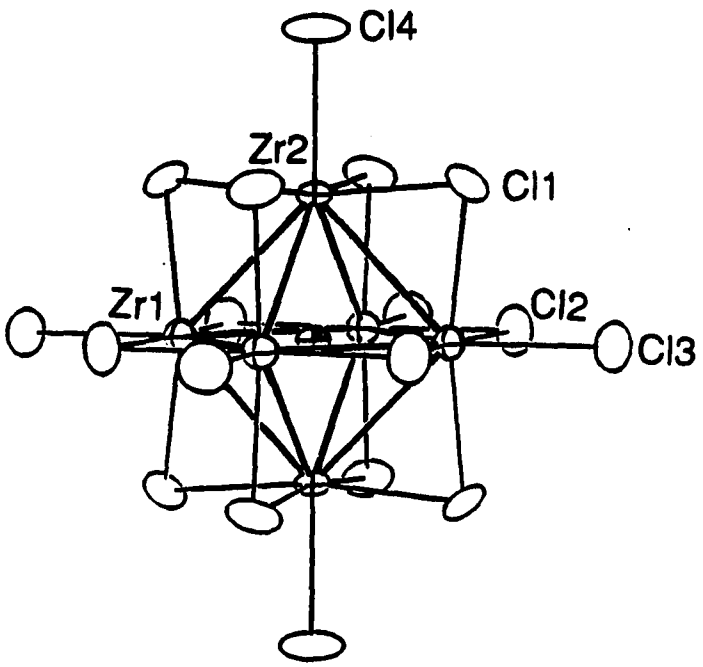

Figure 22. The cluster unit in $Ba_2Zr_6Cl_{17}B$ possesses C_{4h} symmetry with the 4-fold axis vertical (90% probability)

it experiences. The high field of the Ba^{2+} also cause the deviation of the Cl3-Zr1-B angle (176.17(2)°) away from 180° in the plane normal to the chain direction.

As mentioned above, the incorporation of a divalent cation in the lattice of a cluster phase is a particularly interesting aspect of $Ba_2Zr_6Cl_{17}B$. The Ba^{2+} sits on a position with S_4 local symmetry (Figure 23). It has three groups of crystallographically distinct Cl neighbors at rather different distances, which makes a nonambiguous assignment of the coordination number difficult. The four shortest Ba-Cl distances, 3.133 Å, agree well with the sum of crystal radii[66] of Ba^{2+} (CN = 4 not available; CN = 6, 1.47 Å) and Cl^- (1.67 Å). However, if the Ba^{2+} is considered having CN = 8 or 12, the average Ba-Cl distances are 0.09 Å or 0.04 Å longer than the corresponding summations of the crystal radii[66] (CN=8, 1.54 Å + 1.67 Å = 3.21 Å; CN=12, 1.75 Å +1.67 Å = 3.42 Å). The discrepancies can be well understand as the result of Ba^{2+} coordination environment, which deviates from an idealized polyhedron in which all the Cl atoms supposedly have equal distances from the Ba. These differences between the Ba-Cl interactions account for the anisotropic lattice parameter variation accompanying the partial substitution of Ba with Sr. Due to the smaller size of Sr^{2+} (crystal radii: CN=6, 1.32 Å; CN=8, 1.40 Å; CN=12 1.58 Å),[66] the mixed cation M^{2+} – Cl3 distance becomes shortest in order to obtain adequate interaction, while the interactions between M^{2+} with Cl atoms within the second and third coordination spheres may become less important so that M^{2+}-Cl distances are elongated. The possible enhancement of the shorter M^{2+}-Cl3 interaction and weakening of the longer M^{2+}-Cl1 and M^{2+}-Cl2 would

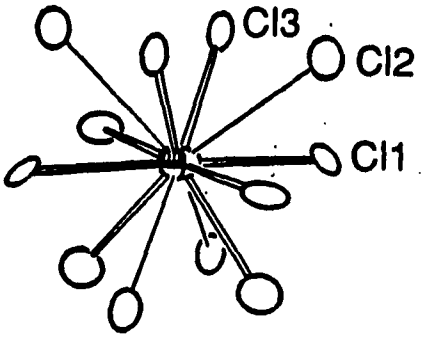

(i)

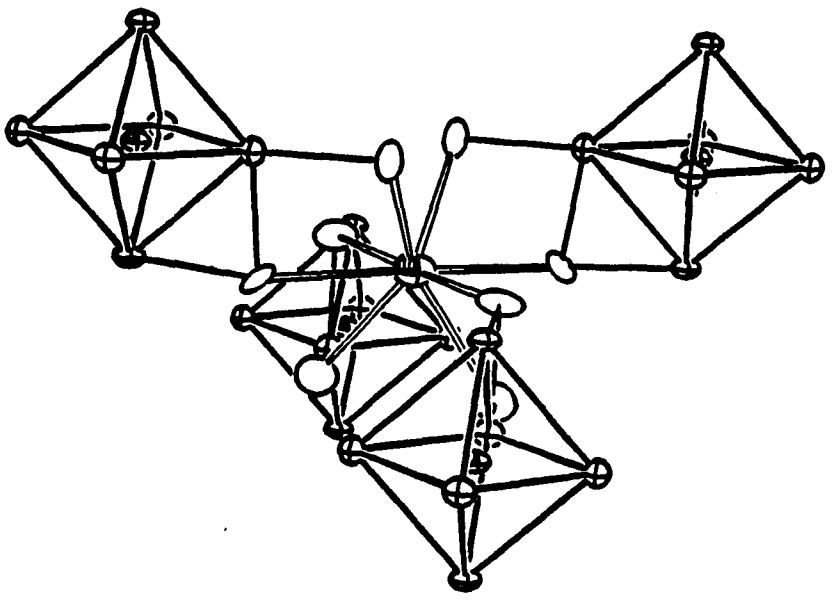

(ii)

Figure 23. The environment of Ba^{2+} in $Ba_2Zr_6Cl_{17}B$ showing (i) the coordination polyhedron (point symmetry S_4, 4-fold axis vertical) (ii) the eight closer Cl atoms together with the four cluster units

lead to the decrease of the c/a ratio because the M-Cli interaction exists only in the plane perpendicular to c. At the same time, this decrease of the c parameter is not likely to cause the bending of the linear cluster connections, since even now the c axis is still longer than that in $CsKZr_6Cl_{15}B$, allowing the linear chains to stretch comfortably.

Zr_6Cl_{15} Type

In the Zr-Cl cluster systems, the 6-15 stoichiometry has the greatest structural versatility. Sharing a common cluster connectivity, $[Zr_6Cl^i_{12}]Cl^{a-a}_{6/2}$, these structure types contain three-dimensional cluster networks. Earlier work in the Zr-Cl systems offered numerous cluster examples centered by main-group elements that belong to four 6–15 structure types, namely the Ta_6Cl_{15},[18] $CsNb_6Cl_{15}$,[46] $K_2Zr_6Cl_{15}B$[45] and the $K_3Zr_6Cl_{15}Be$[45] types. The first three contain unrelated frameworks, and $K_3Zr_6Cl_{15}Be$ is a modification of $K_2Zr_6Cl_{15}B$. With these structure types, the relationship between the structure types and countercations was well demonstrated.

The recent success of incorporating transition metals into the cluster cores has provided more unique cluster phases. Due to the significant expansion of the cluster cores associated with the interstitial change from a main-group element to a transition metal, many of these new clusters exhibit novel structure features. The differences in the structural behaviors of these two groups of Zr-Cl clusters are especially obvious in the Zr_6Cl_{15} systems. For instance, with the same stoichiometry but different interstitial elements,

$Zr_6Cl_{15}N$[74] adopts the Ta_6Cl_{16}[18] structure whereas $Zr_6Cl_{15}Co$ chooses the Nb_6F_{15}[17] structure. Similarly, $KZr_6Cl_{15}C$[47] has a modified $CsNb_6Cl_{15}$[46] structure which differs from the parent structure only in the choice of cation positions, while in its transition metal analogue $KZr_6Cl_{15}Fe$, the expansion of the cluster core causes the bending of the linear chain, resulting in a superstructure of the $CsNb_6Cl_{15}$ type. These observed structural differences between smaller main-group and larger transition-metal interstitials make it possible to examine the correlation between the structure type and cluster size.

To data, in the Zr_6Cl_{15} series, there are five distinctly different structure frameworks (Ta_6Cl_{15}, $CsNb_6Cl_{15}$, $K_2Zr_6Cl_{15}B$, Nb_6F_{15}, $Cs_3(ZrCl_5)Zr_6Cl_{15}Mn$), and five additional structure variations (Table 1). The first four of the above networks were clearly distinguished from each other in terms of the local geometries at the shared Cl^{a-a} atoms and the long range arrangement of the cluster frameworks.[45] In addition, the $Cs_3(ZrCl_5)Zr_6Cl_{15}Mn$ structure is related to the cubic Nb_6F_{15} type via a trigonal twist, and replacing the second cluster net with other structural elements. Besides these well established structure types, another unique 6–15 cluster framework was recently observed in a compound with carbon as the interstitial and cesium as the countercation (produced by a reaction with loaded stoichiometry of $Cs_3Zr_6Cl_{15}C$).[39] This structure is constructed with parallel cluster chains that are connected to each other in the plane normal to the chain direction, leaving channels along the cluster chains with the cross section as large as over 10 Å. The difficulty of resolving this structure mainly rises from locating the Cs^+ ions or other species inside these open

channels. Nevertheless, the existence of a new 6–15 structure type with novel structure features is evident.

The following sections will present the new cluster compounds centered by transition metals in the 6-15 series. They are divided into three groups according to their structure types.

Compounds with the Nb_6F_{15} structure

For over two decades after its discovery, Nb_6F_{15}[17] remained as a structural singularity. Meantime, solid state cluster chemistry became established and developed rapidly, which led to the characterization of numerous transition metal and rare-earth-metal cluster compounds in various structure types. Systematic investigations in the Zr-Cl cluster systems centered by main-group elements resulted in the discovery of cluster phases that not only covered most of the known structure types, but also provided over half-dozen new structure variations (Table 1). However, still no analogue of Nb_6F_{15} was found. Examining the unique structure of Nb_6F_{15} which is composed of two independent and interpenetrating cubic cluster networks, one notices that the small size of F is an important factor in forming this peculiar structure type. Although the cluster core of centered Zr-Cl phases is expanded substantially compared with niobium clusters, the main-group interstitials are apparently not large enough to overcome the counter effect of the anion change from F to Cl, and therefore, structure types other than Nb_6F_{15} are preferred. On the other hand, the incorporation of transition metals into the Zr-Cl cluster systems provides new structure possibilities. As the cluster units are further enlarged, compounds that exhibit novel structure characters have been discovered,

marked by the successful syntheses of a family of cluster phases with the Nb_6F_{15} structure, namely, $Li_xZr_6Cl_{15}M$ (M = Mn, Fe, Co, Ni). Shortly after this, the $Th_6Br_{15}Fe$ was also identified as a new member in the Nb_6F_{15} family.[75] As the only Zr–Cl system that has such a wide interstitial variety, one additional significance of this success is that it makes the direct comparison of different transition metal interstitials possible.

Synthesis The first compound discovered in this series was $Zr_6Cl_{15}Co$. With the 18-electron counting rule as the guide line, the reaction was aimed at making a 6-15 ternary phase, and was carried out at 850°C for 30 days. The powder pattern indicated the product was a 6-15 phase as expected, but with the cubic structure of Nb_6F_{15}[17] which had not been previously observed in Zr-Cl systems. Following the determination of the cell constants, the size of interstices which could be potential sites for cations were estimated. It was noticed that there were sites with coordination number six or four that were probably large enough to accommodate Li^+ ions. By combining this observation with the cluster electron counting rule, the existence of $Li_2Zr_6Cl_{15}Mn$[76] and $LiZr_6Cl_{15}Fe$ was predicted, and soon after proven by successful syntheses.

The presence of the Li in these two phases is supported by the optimal cluster electron count, the observed lattice expansion (Table 24), and the fact that a ternary 6-14 phase $Zr_6Cl_{14}Mn$ (17 e^-/cluster) or $Zr_6Cl_{14}Fe$ (18 e^-/cluster) was formed whenever Li was omitted from the reaction system, even if the Zr/Cl ratio was kept at 6/15. In addition, single crystal X-ray analyses and ^7Li solid state NMR provided

Table 24. Crystal Data for $Li_xZr_6Cl_{15}M$

Formula	$Li_2Zr_6Cl_{15}Mn$	$LiZr_6Cl_{15}Fe$	$Zr_6Cl_{15}Co$	$Zr_6Cl_{15}Ni$
space group	Im3m (No. 229)	Im3m (No. 229)	Im3m (No. 229)	Im3m (No. 229)
Z	2	2	2	2
a, Å[a]	10.3459 (4)	10.2645 (4)	10.186 (4)	10.1907 (4)
V, Å^3	1107.4 (1)	1081.6 (1)	1056.9 (1)	1058.3 (1)
crystal dimen, mm	0.20x0.18x0.14	0.18x0.18x0.12	0.18x0.16x0.16	0.18x0.16x0.10
data collection instrument	RIGAKU AFC6R	DATEX	RIGAKU AFC6R	ENRAF-NONIUS CAD-4
scan mode	ω-2θ	ω	ω-2θ	ω-2θ
$2\theta_{max}$, deg	60	60	50	55
reflections	h,k,ℓ	h,k,ℓ	h,k,ℓ	h,±k,ℓ
measured	935	999	564	1329
observed	900 (I>0)	808 (I>3σ_I)	549 (I>0)	1022 (I>3σ_I)
observed independent	215	177	119	109
absorp coeff μ, cm^{-1}	50.00	52.54	54.73	56.55
range of transm coeff	0.86–1.00	0.76–1.00	0.62–1.00	0.74-1.00
R_{ave}, %	6.4	2.0	11.2	3.3
second ext coeff	2(2)x10^{-7}	7(1)x10^{-7}	2.5(2) x10^{-7}	2.7(3)x10^{-7}
R, %	2.4	3.3	2.4	2.1
R_w, %	3.4	4.2	2.0	3.1
largest residue peak, e$^-$/Å^3	+0.79	+0.30 (near Cl2)	+0.98 (1.74 Å to Co)	+0.67 (near Ni)
	-1.32		-2.22 (at Co)	

[a]Guinier powder diffraction data (numbers of observations are 30 (Mn), 33 (Fe), 30 (Co) and 27 (Ni), respectively).

confirmation of the stoichiometries. Varying the Li/cluster ratio between 0.5/1 to 1.5/1 yielded $Li_xZr_6Cl_{15}Fe$ phases that had essentially the same lattice constants, which suggested that the composition with x = 1 is regulated by the electron counting rule but not by the initial stoichiometry of the reaction.

The above three 18-electron cluster compounds can be produced regularly in high yields (>95%) with the appropriate stoichiometries. However, to facilitate the crystal growth, temperature gradient reactions (950-800°C, 24 days, for $Li_2Zr_6Cl_{15}Mn$; 910-890°C, 25 days, for $LiZr_6Cl_{15}Fe$) were required. Large crystals of $Zr_6Cl_{15}Co$ were obtained from a reaction with a starting stoichiometry of $KBaZr_6Cl_{18}Co$ (750°C, 15 days). No 6-18 phases of known structure types were identified. Instead, the cubic $Zr_6Cl_{15}Co$ was formed as the main product in well crystallized form. An unknown phase (>20 lines, d_{max} ~ 10.15 Å) at about 40% yield was also observed, and since KCl and $BaCl_2$ were both absent from the powder pattern, the unidentified phase might be a cluster phase rich in K and Ba. Despite its unknown identity, this phase or other species evidently served as a minerallizer in the crystallization process of $Zr_6Cl_{15}Co$.

In contrast, $Zr_6Cl_{15}Ni$ was found after reactions were designed to obtain the hypothetical 18-electron compounds ($A_2Zr_6Cl_{18}Ni$, A=K,Cs; 850°C, 25 days and 750-650°C, 7 days). The yields of $Zr_6Cl_{15}Ni$ from these reactions were high (90% and 80%, respectively) with A_2ZrCl_6 as the side product, and nicely formed crystals were also obtained. Yet, efforts to produce $Zr_6Cl_{15}Ni$ from a reaction with the correct ternary stoichiometry failed to provide the expected result. Altering the

proportions of the starting materials with or without ACl and varying the reaction temperature did not solve the problem. These raised questions about the identity of the interstitial atom. The information given by X-ray studies, including cell constants and distances, implied that the compound under investigation was different from $Zr_6Cl_{15}Co$. Furthermore, the EDX spectra collected on several crystals from the above reactions clearly indicated that the elements in these crystals were Zr, Cl and Ni, and a semiquantitative analysis gave a composition of $Zr_{5.7}Cl_{14.8}Ni$, which was identical to $Zr_6Cl_{15}Ni$ within experimental error. No other element was detected by the above analyses. The puzzle remains unsolved. Oxygen contamination cannot be excluded, since the source of Ni in the two reactions that produced the desired compound was $NiCl_2$ from dehydration of the corresponding hydrate without succeeding sublimations. Sulfur from Ta cleaning solution might be another impurity source. These impurities at low concentration cannot be easily detected by the energy dispersive method. A random substitution of Cl by O or, especially, S may not generate distortions that are visible to X-ray analyses. If the contamination did occur, one composition of the Ni compound could be $Zr_6Cl_{14}ONi$ or $Zr_6Cl_{14}SNi$, both with 18 cluster electron counts. Although these do not seem plausible as no examples of zirconium clusters with mixed ligands have been synthesized via high temperature solid state reactions, it is not impossible that such compounds do exist under certain conditions. Nevertheless, this hypothesis needs to be proven by further studies.

Attempts to make the Cr analogue were not successful, leaving Mn as the lightest transition metal in this series and also in any Zr-Cl

cluster system. Substituting the countercation Li in the Mn and Fe compounds with Na led to the formation of an unidentified Mn phase and $Zr_6Cl_{14}Fe$, which implies that the Na is too large to fit into the lattice of the Nb_6F_{15} type. Reactions that were planned to generate compounds with mixed interstitial sites such as $LiZr_6Cl_{15}Mn_{0.5}Co_{0.5}$ or $LiZr_6Cl_{15}Mn_{0.5}Ni_{0.5}$ produced a mixture of two 6-15 phases in the former case and $Li_2Zr_6Cl_{15}Mn$ and an unknown phase in the latter case.

Structure determination The single crystal X-ray analyses of the complete series were conducted in order to acquire first hand information that would allow the direct comparison of different transition metal interstitials. As the structure type was known, the structure determination process was trivial. Nevertheless, precautions were taken to ensure the correct selection of the space group since symmetry changes are possible, especially when Li is incorporated in the Mn and Fe compounds, or since the Ni-centered cluster phase may have an electron count of 19. The cell parameters refined with the powder diffraction data suggested that these phases have the expected cubic symmetry. The body-centering of the unit cell was determined on the diffractometers with program INDEX and successful transformation of the primitive cell. Axial photos were taken to confirm the lattice type and symmetries. As no decay correction was necessary for any of these cases, the data processing included empirical absorption corrections based on ψ-scans and data averaging in the Laue class Im3m. The R_{ave} values for the data sets collected on the RIGAKU diffractometer were higher due to the inclusion of weak reflections with $0 < I < 3\sigma_I$ in the averaging process. The structure refinements were proceeded with

program packages furnished with each diffractometer, and the structure determinations with Nb_6F_{15} as the model were successful, which provided the ultimate evaluation of the choice of space group. Other relevant refinement parameters are tabulated in Table 24.

In all the four cases, the interstitial atoms emerged as large residues of about 20 e/Å^3 on the difference Fourier maps after the Zr and Cl atoms had been refined. Their occupancies were as expected for $LiZr_6Cl_{15}Fe$ (102(1)%) and $Zr_6Cl_{15}Co$ (98(1)%) within experimental errors. On the other hand, a decrease in the occupancies accompanied by a drop in thermal parameters of over 30% was observed for the other two compounds, and the refinements converged with a 92(1)% filled Mn site and a 87(1)% filled Ni site. The isotropic thermal parameters (B_{iso}) of Mn (0.557 Å^2) and Ni (0.552 Å^2) are the smallest in each compound, and also smaller than those of Fe (0.79 Å^2) and Co (0.6 Å^2) in the other two compounds. Although these models with partial occupancies seemed to fit the data measured better, their validity is in question as far as the chemical and physical meanings are concerned. Since a transition metal interstitial atom contributes a large portion of the electrons for the metal-metal bonding, it is very unlikely that certain percentage of the clusters are empty and hence with local cluster electron count far away from the optimal value of 18. Another possibility is that lighter interstitials, such as carbon, nitrogen or hydrogen, substitute for part of the transition metals, resulting in the lower total electron densities at these sites. Since a cluster phase containing more than one centering atom has never been observed, even in the cases where the centering atoms are similar in properties (e.g., Mn and Co), the mixed

interstitial model is not plausible either. Therefore, the problems were attributed to possible crystallographic errors, which are known to be responsible for troublesome refinements of the high symmetry positions. On the other hand, as the problem occurred only for the two extremes in this series, which have either high content of Li or a possible cluster electron count other than 18, the cause of this phenomenon could be distorted lattices with lower symmetries. However, such distortion, if it exists, did not seem significant enough to be detectable. Hence, with the information available, the models with fully occupied interstitial positions were chosen as the best solutions.

Effort was also made to locate and refine the Li atom in the Mn and Fe compounds. The low electron density and possible partial occupancy of Li sites made this task difficult. Starting with the refined main structure networks, the vacancies large enough to host Li atoms were located. These are the two six-coordinate positions [8c at (1/4,1/4,1/4); 12d at (1/4,0,1/2)] and one four-coordinate site [48k at (x,x,z) with x ~ 3/8, z ~ 1/8 and Li-Cl 2.26 Å]. Difference Fourier maps were calculated to examine the residue peaks at these possible positions. In the case of $LiZr_6Cl_{15}Fe$, no residues higher than 0.3 $e^-/Å^3$ were found on the difference map, and refinement with Li on any of these sites resulted in unreasonably large thermal ellipsoids, negative multiplicities, or both. The Li concentration increases in $Li_2Zr_6Cl_{15}Mn$, and the highest residue peak of 2.3 $e^-/Å^3$ was on the 12d position. Subsequent refinement of the Li on this position with fixed occupancy of 1/3, which corresponds to the formula of $Li_2Zr_6Cl_{15}Mn$, gave B_{iso} equal to 4(1) $Å^2$. As expected, this Li position can be refined neither

anisotropically nor with the multiplicity as an additional variable because of the low electron density associated with a light atom on a partially occupied site. Nevertheless, this refinement confirmed the existence of the Li in the lattice, and more important, provided symmetry information necessary for interpreting the ^{7}Li NMR spectrum. No additional residue peaks higher than the background ($\pm 1e^{-}/Å^{3}$) were found on the other two possible sites.

Although locating Li in $LiZr_6Cl_{15}Fe$ with X-ray diffraction data was unsuccessful, and a ^{7}Li NMR study was not done, it is believed that the Li is present in this phase. Direct evidence for this conclusion is the systematic variation of the cell volume from $Zr_6Cl_{15}Co$ to $LiZr_6Cl_{15}Fe$ to $Li_2Zr_6Cl_{15}Mn$ (Table 24). Considering the fact that for these three 18-electron clusters, the cluster cores contract as the lattice expands, the significant volume increases are attributable to the incorporation of the Li atom, which has an empirical molar volume increment of 12 to 13 $Å^3$ in these phases. The consistency of the volume changes also suggests that the Li in $LiZr_6Cl_{15}Fe$ should occupy the same position as it does in the Mn analogue, and if this is so, the Li-Cl distances would be 2.57 Å (Li-Cl1) and 2.58 Å (Li-Cl2) with the average of 2.578 Å, also acceptable for a six-coordinate Li.

The positional and thermal parameters of the final solutions are reported in Table 25, and important distances are listed in Table 26.

Structure description Each of the four transition-metal-centered cluster phases in the Nb_6F_{15} family contains two identical, independent, and interpenetrating cubic cluster nets as the main structure framework (Figure 24). This simple yet elegant arrangement

Table 25. Positional and Thermal Parameters for $Li_xZr_6Cl_{15}Z$

$Li_2Zr_6Cl_{15}Mn$	x	y	z	B_{11}
Zr	0.23311(5)	0	0	0.76(2)
Cl1	0	1/2	1/2	1.03(8)
Cl2	0	0.2480(2)	y	2.17(4)
Mn	0	0	0	0.7844(4)
Li[a]	1/4	0	1/2	–
$LiZr_6Cl_{15}Fe$				
Zr	0.2361(1)	0	0	1.29(4)
Cl1	0	1/2	1/2	0.7(1)
Cl2	0	0.2483 (1)	y	1.90(7)
Fe	0	0	0	0.79(9)
$Zr_6Cl_{15}Co$				
Zr	0.24094(4)	0	0	0.61(2)
Cl1	0	1/2	1/2	0.68(6)
Cl2	0	0.24883(6)	y	1.91(3)
Co	0	0	0	0.6076(4)
$Zr_6Cl_{15}Ni$				
Zr	0.2413 (1)	0	0	0.66(3)
Cl1	0	1/2	1/2	0.6(1)
Cl2	0	0.2485 (1)	y	1.57(7)
Ni	0	0	0	1.14(6)

[a]The occupancy of Li was fixed at 33%, corresponding to the formula of $Li_2Zr_6Cl_{15}Mn$.

B_{22}	B_{33}	B_{12}	B_{13}	B_{23}	B_{eq}
1.09(2)	B_{22}	0	0	0	0.98(2)
2.85(6)	B_{22}	0	0	0	2.24(5)
1.08(6)	B_{22}	0	0	−0.18(2)	1.46(3)
B_{11}	B_{11}	0	0	0	0.7844(4)
–	–	–	–	–	3(1)
1.61(3)	B_{22}	0	0	0	1.50(3)
2.3(1)	B_{22}	0	0	0	1.8(1)
0.99(4)	B_{22}	0	0	−0.23(5)	1.29(5)
B_{11}	B_{11}	0	0	0	0.79(9)
0.92(2)	B_{22}	0	0	0	0.82(2)
2.14(5)	B_{22}	0	0	0	1.66(4)
0.94(3)	B_{22}	0	0	−0.20(3)	1.26(2)
B_{11}	B_{11}	0	0	0	0.6076(4)
0.72(2)	B_{22}	0	0	0	0.70(2)
1.92(9)	B_{22}	0	0	0	1.5(1)
0.79(4)	B_{22}	0	0	−0.25(6)	1.05(5)
B_{11}	B_{11}	0	0	0	1.14(6)

Table 26. Important Interatomic Distances and Angles in $Li_xZr_6Cl_{15}Z$ (Z = Mn, Fe, Co, Ni, x = 2, 1, 0)

		$Li_2Zr_6Cl_{15}Mn$	$LiZr_6Cl_{15}Fe$	$Zr_6Cl_{15}Co$	$Zr_6Cl_{15}Ni$
Distances (Å)					
Zr–Zr	x12	3.4107(8)	3.428(2)	3.4708(6)	3.477(1)
Zr–Cl1	x6	2.7612(6)	2.709(1)	2.6388(4)	2.636(1)
Zr–Cl2	x12	2.5708(1)	2.552(2)	2.5359(7)	2.533(1)
Zr–Z	x6	2.4117(6)	2.424(1)	2.4542(4)	2.459(1)
Li–Cl1	x2	2.5864(1)	2.566(1)[a]	—	—
Li–Cl2	x4	2.607(2)	2.584(1)[a]	—	—
Angles (°)					
Cl2–Zr–Cl2	x12	173.13(4)	174.37(6)	176.36(3)	176.69(5)

[a]Calculated by assuming Li occupies the same position as it does in $Li_2Zr_6Cl_{15}Mn$.

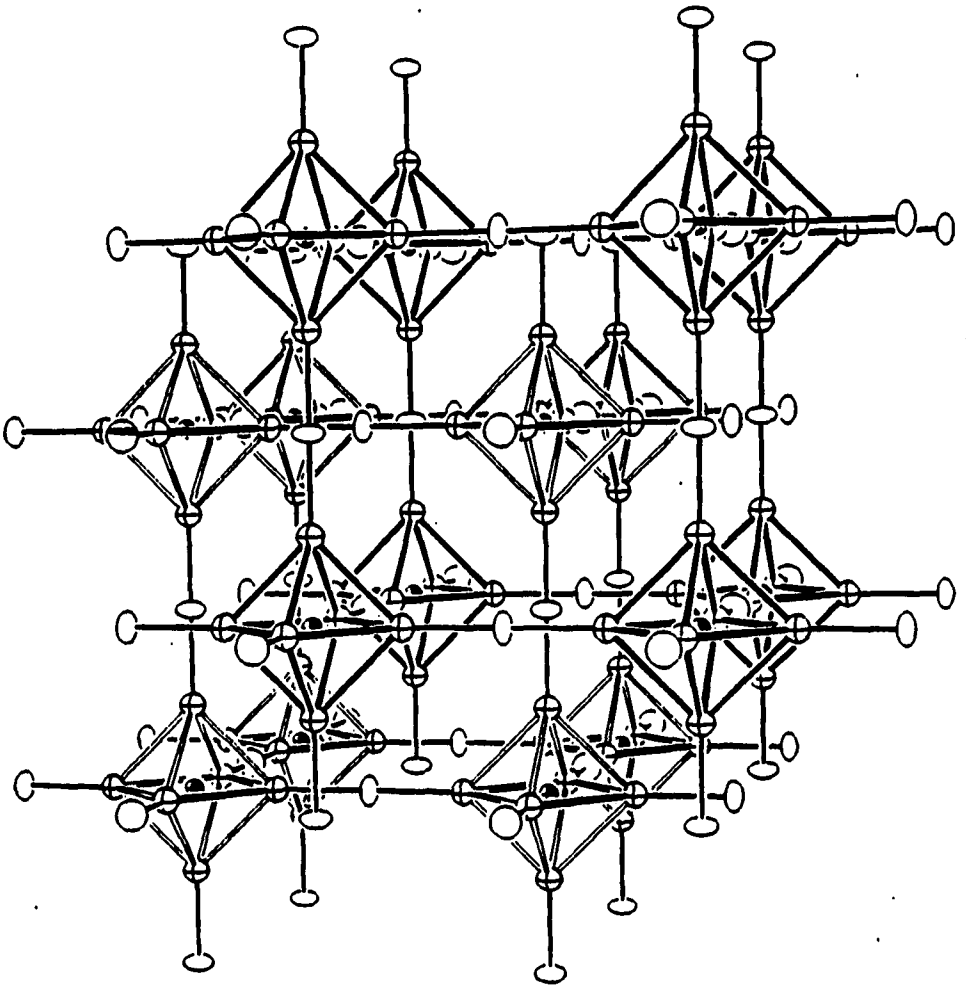

Figure 24. The two identical and interpenetrating $[Zr_6Cl^i_{12}Z]Cl^{a-a}_{6/2}$ networks in the compounds with the Nb_6F_{15} structure. They are distinguished by solid and open outlines of the zirconium octahedra. Cl^i atoms are omitted for clarity

demonstrates once again the sophistication of Nature in organizing solid state materials. The cluster cores in these phases are perfect octahedra with the high symmetry, O_h, imposed by the space group. The Zr–Cl^i (Zr–Cl2) distances are normal, showing a slight decrease as the cluster cores expand. On the other hand, the Zr–Cl^{a-a} (Zr–Cl1) distances are more sensitive to the cation content and the subsequent lattice expansion. As more Li is incorporated into the lattice, the Zr–Cl^{a-a} distance increases significantly. In addition, the thermal ellipsoids of all the Cl atoms appear to reflect the preferred thermal motions of each Cl, i.e., in the tangential direction of the metal core for Cl^i and in the plane normal to the Zr–Cl bonds for Cl^{a-a}. These are characteristic for the atoms that are confined by strong Zr–Cl interactions.

The units related by body centering belong to two separate networks. Each of these cluster nets is still constructed with linear linkage between clusters, similar to that observed in $Ba_2Zr_6Cl_{17}B$.[38] However, the connections are now extended to all three dimensions. Compared with the one dimensional cluster chains in $Ba_2Zr_6Cl_{17}B$, the cluster networks in the Nb_6F_{15} structure are less flexible. Consequently, much more restricted geometric requirements must be met in order to achieve the perfect fit of the lattice, which explains why the $Ba_2Zr_6Cl_{17}B$ types has both B and Mn analogues, whereas the Nb_6F_{15} type only exists among transition-metal-centered Zr–Cl clusters.

The size of the cluster cores is the most crucial condition for the existence of a Nb_6F_{15} type structure. The cluster cores centered by transition metal elements are expanded significantly, marked by M-Zr

distances closer to the values of the Zr-Cl^{i} distances, and the Cl-Zr-Cl angle across the square faces of the cuboctahedra approaches 180°. Imagine a lattice constructed with one cubic $[Zr_6Cl_{12}M]Cl_{6/2}$ network that has linear connections at Cl^{a-a}. When the cluster core contracts, the terminal Cl atoms are pulled toward the center of the cluster, Cl^{a-a} and Cl^{i} become closer, and the space left between the $[Zr_6Cl_{12}M]$ units is reduced. As a result, there will be less space left for the lattice to accommodate the second cluster network. Since high space filling efficiency is expected for a solid state material synthesized via a high temperature route, the cubic cluster net will not be preserved unless Nature can find other alternatives to fill the voids that used to be occupied by cluster units without disturbing the linear cluster connections. This is the reason why in the Zr-Cl systems, the analogues of Nb_6F_{15} were discovered only when transition metals were accommodated in the cluster cores. Although the known M_6X_{12}-based cluster phases are large in number, only those with the center to M distance near the M-X distances may exhibit the Nb_6F_{15} structure.

In the Co and Ni compounds, the two independent cluster networks may be considered as two giant neutral molecules that are entangled together with van der Waals interactions between them. When the size criterion of the cluster unit is fulfilled, the two cluster nets can coexist comfortably, without enough tension to bend or stretch the linear connections or to cause distortions of any other kinds. The nearest Cl contact in these two compounds is between two intracluster Cl2 atoms. With these Cl2-Cl2 distances (3.585 Å in $Zr_6Cl_{15}Co$, 3.581 Å in $Zr_6Cl_{15}Ni$) being the shortest and the rest larger than 3.60 Å, the

repulsions between the Cl atoms, especially between intercluster and internetwork Cl atoms, are negligible. When the cluster frameworks become charged in the Mn and Fe phases, they are held together by Li^+ ions. The Cl-Cl interactions are further minimized as the lattices expand upon the incorporation the countercation.

In this series one observes an expansion of the cluster cores as the interstitial atom becomes heavier. This expansion is more pronounced for the first three members, while it is less obvious, though still observable, between $Zr_6Cl_{15}Co$ and $Zr_6Cl_{15}Ni$. In general, it is opposite to the trend that the atomic radii decrease across the periodic table. For the three 18-electron clusters, the Zr–M distances are about 0.2 Å smaller than the corresponding sum of metal single-bond radii,[77] which may serve as one indication of the electronic state of these centering atoms. The incorporation of Li^+ into the lattice may have effects on the ZrCl interactions, resulting in the observed changes in cluster dimensions. The comparison between Zr–Co and Zr–Ni is more complicated. Since the size of Ni atom is supposedly smaller than that of Co (metal single-bond radii; Co 1.157 Å, Ni 1.149 Å), and an 19-electron cluster should be smaller than an 18-electron cluster based on the observation on $Cs_3Zr_6Cl_{16}C$, a 15-electron cluster, there is no obvious explanation why the distances vary in the opposite direction. On the other hand, although there is information available for iodide clusters centered by transition metals, since the data are for compounds from different structure types or clusters with various electron counts, the only conclusion that can be drawn from the direct comparison of the chlorides and iodides is the effective radii of the centering atoms are

larger for the iodide clusters, which again is a result of the matrix effect.

The locations of the Li atoms in $Li_2Zr_6Cl_{15}Mn$ are shown in Figure 25. Examining the three possible vacancies available in the lattice, one realizes that the radii of the empty four-coordinate positions (48k) are 0.2 Å too small to accept Li^+ ions. In addition, although the two six-coordinate sites, 12d and 8c, are similar in size, and both are on the zero potential surface that separate the two cluster networks,[78] the 12d positions are more favorable than the 8c sites since they have fewer closest Zr neighbors (four vs six). Hence, only one type of Li position, the 12d, is used, consistent with the ^7Li NMR spectrum of $Li_2Zr_6Cl_{15}Mn$ that shows one signal (below). The Li atom has four cluster units as neighbors (Figure 26). Each of them provides one Cl^i, and each pair that belongs to the same cluster network contributes one Cl^{a-a}. The average Li-Cl distance is in good agreement with the sum of the crystal radii (Li, CN=6, 0.90 Å; Cl 1.67 Å).[66] Thus replacing the Li with a larger cation will require the further expansion of the lattice. As observed in this structure series, the $Zr-Cl^{a-a}$ distance responds to a lattice expansion. With the longest known $Zr-Cl^{a-a}$ value of 2.78 Å in $Li_2Zr_6Cl_{15}Mn$, it is possible that any further stretching of this bond will destabilize the entire lattice.

The Li^+ volume increment of 12 $Å^3$ in these compounds is much greater than the literature value (1-2 Å).[79] However, it is acceptable since the incorporation of Li^+ into the cubic Zr_6Cl_{15} structure expands not only the Li site, but also many other vacancies in the lattice. When $Li_2Zr_6Cl_{15}Mn$ is compared against $Zr_6Cl_{15}Co$, a significant increase in the

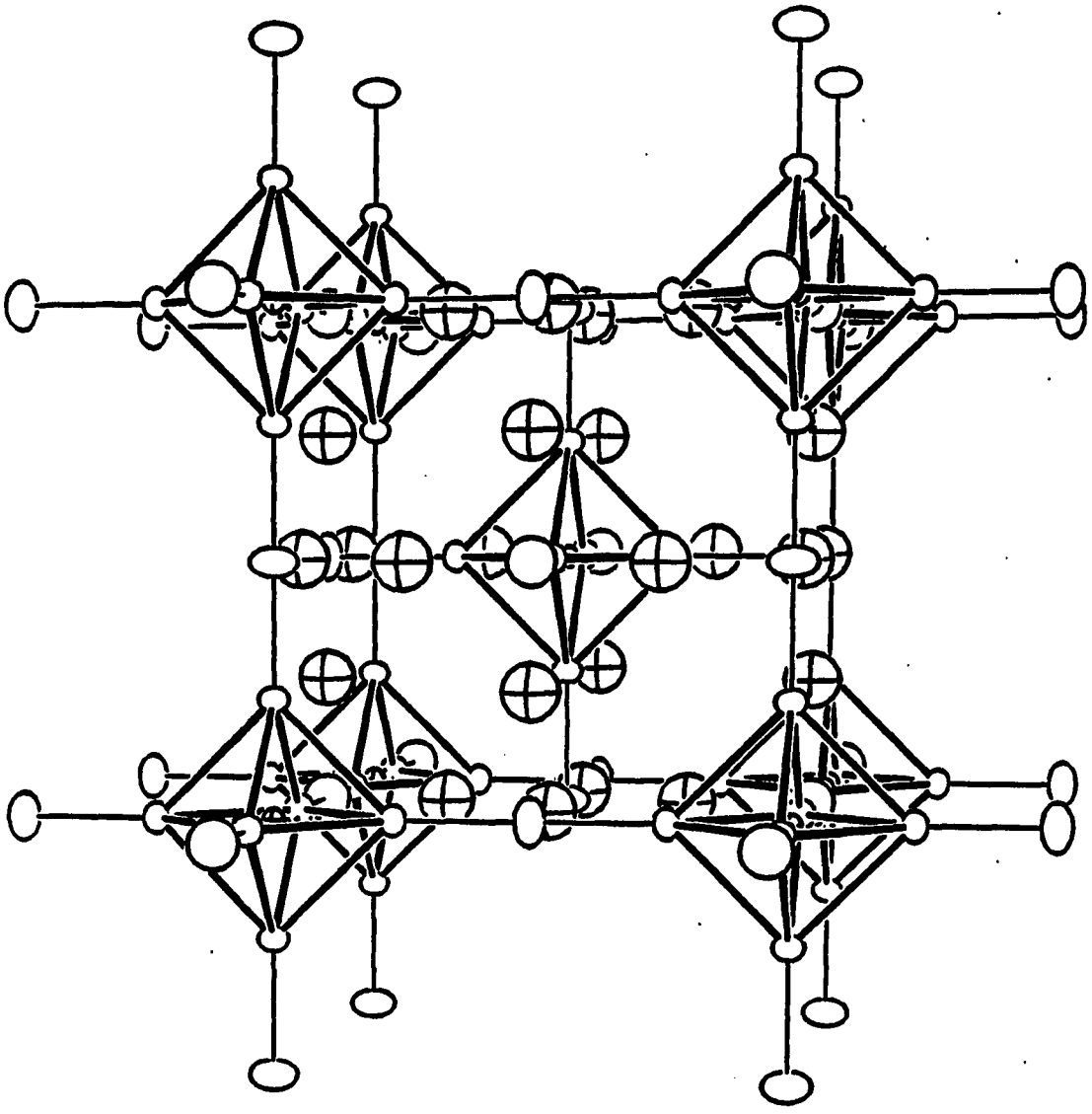

Figure 25. The locations of Li^+ ions in the unit cell of $Li_2Zr_6Cl_{15}Mn$ (90% probability). The crossed spheres are Li ions, and Cl atoms are not shown

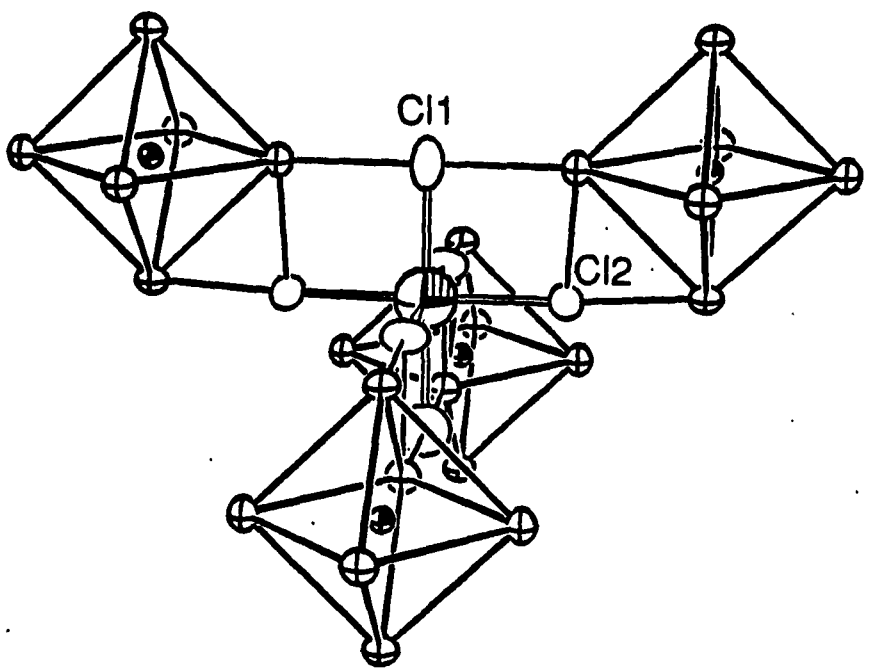

Figure 26. The Li and its surrounding cluster units in $Li_2Zr_6Cl_{15}Mn$. Li possesses D_{2d} symmetry with the S_4 axis vertical and one of the mirror planes in the plane of the paper (90% probability)

inter-network Cl–Cl distances (Cl2–Cl2, 3.686(1) Å vs 3.6182(9) Å; Cl1–Cl2, 3.686(1) Å vs 3.6181(9) Å) and a moderate increase in the intra-cluster Cl–Cl distances (Cl2–2, 3.630(1) Å vs 3.5845(9) Å; Cl–Cl2, 3.658(1) vs 3.6014(1) Å) are observed. This indicates that while Li enters these cluster phases, the entire lattice undergoes a uniform expansion, resulting in the observed large Li volume increment. On the other hand, the smaller literature value corresponds to simpler compounds, e.g., LiCl, where Li occupies all suitable vacancies in the chlorine lattice with a full occupancy.

<u>^{7}Li solid state NMR studies on $Li_2Zr_6Cl_{15}Mn$</u> Although it is believed that the presence of Li is essential in the syntheses processes, and Li plays important structural and electronic roles in forming $Li_2Zr_6Cl_{15}Fe$ and $Li_2Zr_6Cl_{15}Mn$, it seemed necessary to employ ^{7}Li NMR to confirm the results of the single crystal X-ray analysis.

The room temperature ^{7}Li solid state NMR spectrum of $Li_2Zr_6Cl_{15}Mn$ (Figure 27) shows a triplet centered at -0.4 ppm. Its peak profile is completely different from that of LiCl, a typical Gaussian singlet (Figure 4). This clearly indicates that the Li in the sample is not LiCl. The splitting of the signal corresponds to the noncubic symmetry ($Q_c \neq 0$), the symmetric arrangement of the two satellites implies that there is only one type Li site, and the small chemical shift with respect of LiCl suggests similarities between the chemical environment in LiCl (CN=6) and that in the sample under study. Considering the fact no other Li-containing phase was observed on the powder pattern, the Li signal is assigned to the Li in $Li_2Zr_6Cl_{15}Mn$.

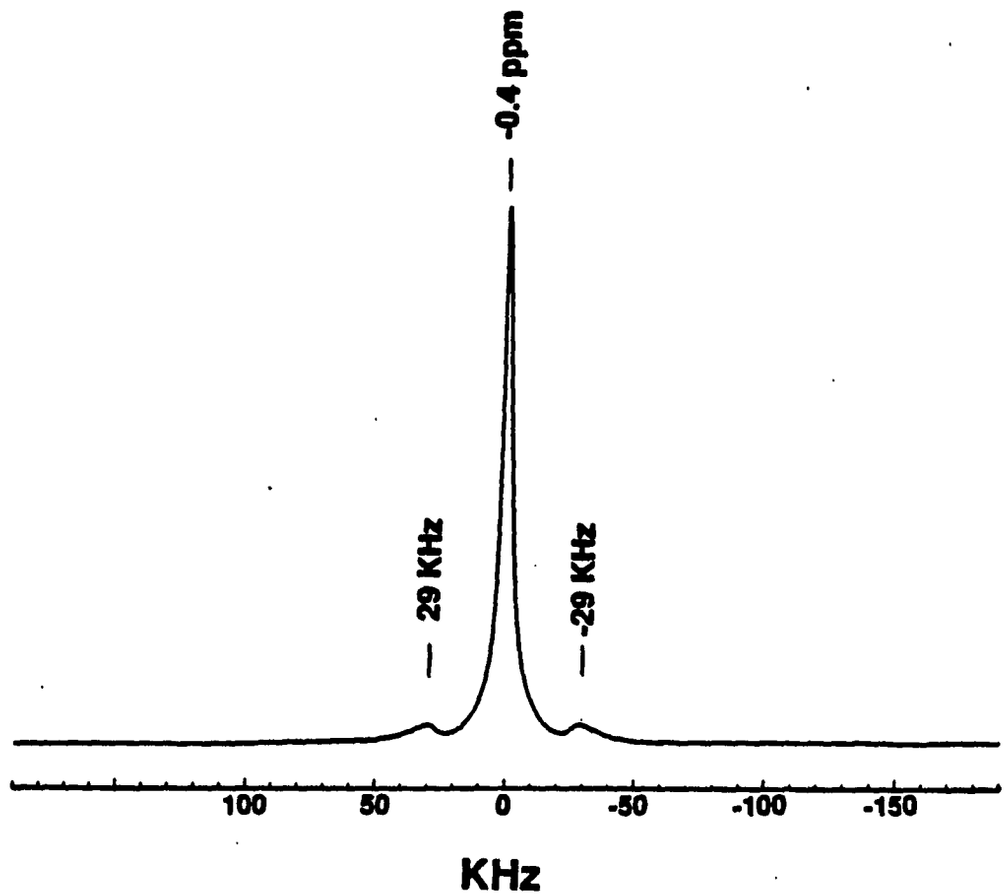

Figure 27. A room temperature solid state ^{7}Li NMR spectrum of $Li_2Zr_6Cl_{15}Mn$

However, the above observations are not sufficient to derive the exact Li location in the lattice. Among the three possible Li positions in the 6-15 structure, all of them have noncubic symmetries ($Q_c \neq 0$). The two sites with CN=6 have axial symmetries and hence have zero asymmetry parameters ($\eta=0$), while the distorted tetrahedron site (CN=4) has $\eta \neq 0$. Yet, comparing the spectrum with the idealized line shapes[80,81] of a nucleus with I = 3/2 only rules out the possibility of $\eta=1$. Identification of another pair of satellites is necessary to solve the equations containing two unknowns, Q_c and η. Attempts were made without success to locate additional peaks, including increasing scan time, increasing the sample amount, and cooling the sample. Manipulations of the data, such as artificial enhancement of the signal height, or taking the derivative of the spectrum, did not help either. It is very likely that the shoulders and steps are lost in the background due to the line broadening. One of the possible solutions to this problem, spinning the sample, is not available.

Nevertheless, the study was concluded by combining the results of NMR studies and the X-ray analysis. The structure solution indicates that Li occupies a position with D_{2d} point symmetry, and therefore the asymmetry parameter η associated with this Li should be zero. With this additional information, the quadrupole coupling constant is determined to be 58 KHz. The available information about Li NMR was based on studies of ^6Li (I = 1) in organolithium solution species.[82] Since the quadrupole moment of ^6Li is only about one hundredth of that of ^7Li, and these studies avoided dealing with quadrupole coupling, no direct comparison can be made. However, the magnitude of this quadrupole

coupling constant may be associated with a moderate electric quadrupole coupling interaction when it is compared with that of ^{9}Be in beryllium metal ($I = 3/2$, $Q_c = 60$ kHz)[83] and of ^{11}B in a series of transition metal monoborides ($I = 3/2$, $Q_c \sim 100$ kHz).[81]

Because the Li atoms are located on the zero potential surface in the lattice,[78] similar to the situation of Ag^+ ions in α-AgI (Im3m, Z = 2),[84] it is possible that the Li^+ ions have a relatively high mobility. In order to study the thermal motion of Li atoms in the lattice, a low temperature (173 K) NMR study on a $Li_2Zr_6Cl_{15}Mn$ sample was carried. However, no significant change in line shape was observed. The fact that the peak width did not increase with the decrease in temperature suggests that the thermal motion of Li at room temperature is comparable to that at 173 K. Considering that AgI becomes a solid electrolyte above 419 K, it is logical that experiments above room temperature are necessary to detect the changes in the mobility of Li in $Li_2Zr_6Cl_{15}Mn$. The Li atoms stay on the 12d positions at room temperature consistent with the single crystal X-ray analysis. An increase in temperature may provide energy required for thermal motion of Li.

The ^{7}Li solid state NMR could not be conducted on $LiZr_6Cl_{15}Fe$ because of the minor ferromagnetic impurities, supposedly Fe or $ZrFe_2$, were present in the sample. Although no impurity was detectable by X-rays, it caused the sample to respond to a strong magnetic field, and this may not only interfere with the experiment but also be potentially hazardous to the equipment.

A ^{55}Mn (I=5/2) solid state NMR study on $Li_2Zr_6Cl_{15}Mn$ did not show any signal in the expected region. In addition, no magnetic susceptibility

measurement is available on the four compounds in this group, or any other transition-metal-centered cluster phase, due to the complications raised by the impurities containing the interstitial elements which also contribute to the magnetic signals measured.

<u>$Cs_3ZrCl_5Zr_6Cl_{15}Mn$</u>

The search for transition-metal-centered clusters has not only given a family of clusters with Nb_6F_{15} structure and a group of compounds with the modified $CsNb_6Cl_{15}$ structure, but it has also led to the characterization of a new Mn-stabilized cluster phase with a novel structure type, namely, $Cs_3(ZrCl_5)Zr_6Cl_{15}Mn$ (= $Cs_3Zr_7Cl_{20}Mn$). As the lightest transition-metal that has been incorporated into the Zr-Cl cluster systems, Mn seems to behave differently from Fe and Co where 6-15 phases are concerned. On one hand, no Mn analogue with a structure related to that of $CsNb_6Cl_{15}$ has been observed; on the other hand, $Cs_3(ZrCl_5)Zr_6Cl_{15}Mn$ is still the only known 18-electron cluster compound of this type. Although it is possible that these phenomena are coincidental, or false observations due to the limited number of experiments conducted, it at present appears puzzling. Since $Li_2Zr_6Cl_{15}Mn$ does exist, it is difficult to imagine that the electronic state or the size of Mn prevents Mn compounds from choosing the same structure types as the rest of the transition-metal centered clusters under study. Nevertheless, the characterization of $Cs_3(ZrCl_5)Zr_6Cl_{15}Mn$ contributed to the further understanding of the structural chemistry of cluster compounds. It also showed that the Nb_6F_{15} structure is related to the $Cs_3(ZrCl_5)Zr_6Cl_{15}Mn$ structure through a trigonal twist, which parallels the structure relation between ReO_3 and RhF_3.[85] This

observation again emphasizes the structural resemblance between the complex cluster systems and the simple salt systems, despite their obvious differences in chemical compositions and bonding features. It also demonstrates the sophisticated ways that Nature chooses to organize matter in the solid state.

Synthesis

$Cs_3(ZrCl_5)Zr_6Cl_{15}Mn$ was first observed as an unknown phase produced from a reaction (850°C, 4 weeks, and 800–750°C, 2 weeks) that was designed to synthesize "$Cs_2Zr_6Cl_{15}Mn$",[76] a hypothetical 18-electron cluster compound supposedly with a structure related to $KCsZr_6Cl_{15}B$ and $KZr_6Cl_{15}Fe$ (modifications of the $CsNb_6Cl_{15}$ type) or $K_2Zr_6Cl_{15}B$. This new compound was obtained as the major phase (>50%) together with $CsZr_6Cl_{14}Mn$ and other side products, ZrCl and Cs_2ZrCl_6. In order to acquire single crystals, this reaction was repeated at higher temperatures. The experiments showed that the Mn cluster phases all decompose at temperatures higher than 920°C, yielding only simple compounds such as Cs_2ZrCl_6, $ZrCl_4$ and ZrCl. On the other hand, when a temperature gradient was applied (900 – 850°C, zone furnace, 6 weeks), the reaction gave well crystallized products. Crystals of both $CsZr_6Cl_{14}Mn$ and $Cs_3Zr_7Cl_{20}Mn$ were obtained from the same reaction, saved, and used for the structure determination of the latter.

Following the single crystal X-ray study, efforts were made to improve the yield of $Cs_3(ZrCl_5)Zr_6Cl_{15}Mn$. However, starting with the appropriate stoichiometry, the reactions failed to provide the single phase product. At the temperature around 850°C (6 weeks), $CsZr_6Cl_{14}Mn$ and Cs_2ZrCl_6 were obtained as the main products, and no

$Cs_3(ZrCl_5)Zr_6Cl_{15}Mn$ were observed in the powder pattern. Lowering the temperature to 800°C (2 weeks) made the desired phase the major phase, yet it still coexisted with $CsZr_6Cl_{14}Mn$ and Cs_2ZrCl_6. These facts suggested that in the vicinity of the chosen reaction conditions, there is an equilibrium between the new 6–15 double salt $Cs_3(ZrCl_5)Zr_6Cl_{15}Mn$ and the simpler compounds $CsZr_6Cl_{14}Mn$ and Cs_2ZrCl_6. As the reaction temperature is raised, the equilibration shifts to the side of the simpler phases, leading to the decomposition of $Cs_3(ZrCl_5)Zr_6Cl_{15}Mn$.

Expanding the chemical composition of compounds in this structure type was attempted with very limited success. To date, the only isostructural cluster phase is the 14-electron boron analogue, which was obtained earlier as an unidentified phase in reactions aimed at $Cs_3Zr_6Cl_{16}B$ (850°C, 20 days).[44] It was noticed that $Cs_3(ZrCl_5)Zr_6Cl_{15}B$ obtained from these reactions has very low contamination from the corresponding 6–14 phase and Cs_2ZrCl_6 (<10%), in contrast to the observations in the Mn system. Since the result from a reaction with the appropriate stoichiometry is not available, it is not known whether the $Cs_3Zr_7Cl_{20}B$ exhibits a thermal stability similar to that of $Cs_3Zr_7Cl_{20}Mn$. However, it would not be too surprising to see that the yield of $Cs_3(ZrCl_5)Zr_6Cl_{15}B$ decreases as the starting stoichiometry is changed to more oxidizing. Similar phenomena have been observed in previous research, which concluded that the best yields of certain Zr–Cl cluster phases can only be obtained with slightly altered, not exact, stoichiometries. As a good example, $Cs_3Zr_6Cl_{16}B$ (14 e^-/cluster) is made when the reaction is carried to give $Cs_3Zr_6Cl_{15}B$; a reaction designed to

make $Cs_3Zr_6Cl_{16}B$ will instead produce $Cs_3(ZrCl_5)Zr_6Cl_{15}B$ in over 90% yield.[44]

No other compounds with $Cs_3(ZrCl_5)Zr_6Cl_{15}Mn$ structure have been observed, which might be because the optimal conditions have not been found. Nevertheless, under the reaction conditions that produced $Cs_3(ZrCl_5)Zr_6Cl_{15}Mn$ and $Cs_3(ZrCl_5)Zr_6Cl_{15}B$, substitution of Cs^+ with Rb^+ only resulted in $RbZr_6Cl_{14}Mn$, an unknown phase in the boron case, and Rb_2ZrCl_6, presumably due to the smaller size of Rb (CN=12, 1.86 Å), which further decreases the thermal stability of 6–15 phase with respect to the observed cluster compound. Similarly, a reaction aimed at $K_3Zr_7Cl_{20}B$ yielded $KZr_6Cl_{14}B$ as the main product.

The results of changing the interstitial to Cr ($M_3Zr_7Cl_{20}Cr$, 17 e^-/cluster, M = Cs, Rb) or Fe ($M_3Zr_7Cl_{20}Fe$, 19 e^-/cluster M = Cs, K) were also negative, yielding unidentified phases in the former case (d_{max} < 6 Å) and $MZr_6Cl_{15}Fe$ ($CsNb_5Cl_{15}$ type) for the Fe reactions. Replacing Zr^{4+} with cations of similar size to make 18-electron cluster phases $Cs_3CuZr_6Cl_{20}Co$ and $Cs_3NbZr_6Cl_{20}Cr$ also ended with unknown phases with d_{max} < 6 Å, probably noncluster compounds. In conclusion, $Cs_3(ZrCl_5)Zr_6Cl_{15}Mn$ and its boron analogues are at present the only examples in this structure type.

Structure determination The crystal used for single crystal X-ray study had roughly a rod shape. It appeared black under reflected light, and deep purplish red under transmitted light. The data collection was conducted on an ENRAF NONIUS CAD-4 diffractometer. The primitive cell based upon indexing 25 reflections (θ = 8.83 - 17.25°) located by program SEARCH appeared to be triclinic [12.878(3) Å,

12.886(2) Å, 13.868(3) Å; 90.08(2)°, 117.59(2)°, 119.95(2)°]; however, it was a nonstandard setting of a cell with trigonal symmetry and could be transferred to a R-centering hexagonal cell by TRANS. The axial photos revealed two mirror planes perpendicular to $\vec{a}$ and $\vec{b}$ axes, respectively. The Laue class thus determined is $R\bar{3}m$. The diffractometer was set to collect one quadrant of data ($hk\ell$, $-hk\ell$), including those supposedly missing due to the R-centering. During the period of over ten hours, 1200 reflections were collected, and the reflection condition ($-h+k+\ell=3n$) clearly confirmed the R-centering as well as the obverse setting of the unit cell. Data collection was then continued with this absence condition. At the end of the data collection, six psi-scans were measured. Other important data collection information is listed in Table 27.

The data preparation started with analyzing the intensities of the three standard reflections, and since the net change was +0.1% at the end of 38 hours of X-ray exposure, no decay correction was necessary. The processed data provided one additional reflection condition ($h\bar{h}0\ell$, $h+\ell=3n$, $\ell=2n$); therefore R3c and $R\bar{3}c$ were the only two possible space groups. The systematic absences as well as weak reflections (3σ cutoff) were then rejected from the data set, and data were averaged for the Laue class $R\bar{3}m$ with R_{ave} of 3.3%.

The first step toward the structure solution was performing the direct method search SHELXS-86.[58] Considering the fact that most known solid state cluster compounds are centric, $R\bar{3}c$ was taken as the first choice. However, the solution in this space group did not seem plausible for the top few peaks with the highest electron densities

Table 27. Crystal Data for $Cs_3(ZrCl_5)Zr_6Cl_{15}Mn$

space group	$R\bar{3}c$ (No. 167)
Z	6
a, Å[a]	12.8924 (1)
c, Å	35.187 (6)
V, Å^3	5067 (1)
crystal dimen, mm	0.10 x 0.12 x 0.26
data collection instrument	ENRAF NONIUS CAD4
scan mode	ω-2θ
$2\theta_{max}$, deg	60
reflections	$\pm h,k,\ell$
measured	5165
observed	3204
observed independent	920
absorp coeff μ, cm^{-1} (Mo Kα)	71.7
range of transm coeff	0.916 – 1.00
R_{ave}, %	3.3
second ext coeff	7.9 (4) x 10^{-8}
R, %	1.9
R_w, %	2.3
largest residue peak, e$^-$/Å^3	+0.6 at (0.0, 0.0, 0.43)
	-0.6 at (0.0, 0.0, 0.33)

were unreasonably close to each other. On the other hand, the solution for R3c was very promising. Subsequent structure refinement of this incomplete initial model with standard least-square full matrix calculations and Fourier syntheses (difference Fourier maps) was successful, resulting in the empirical formula of $Cs_3Zr_7Cl_{20}Mn$, fair thermal parameters for each atom, and an essentially flat final difference map (both positive and negative peaks were below 1 $e^-/Å^3$).

A rough ORTEP[84] picture was drawn in order to clarify the connectivity of the clusters and functionalities of different atoms. It showed that the compound was a 6-15 double salt, $Cs_3(ZrCl_5)Zr_6Cl_{15}Mn$. In addition, this picture revealed the possibility of the structure being centrosymmetric. This suspicion was supported by two other observations. First, the positions of a few atoms seemed to be peculiar as they were on special positions in a space group of higher symmetry. Secondly, the thermal parameters of several pairs of atoms were coupled, especially in the early stages of refinement. Taking these phenomena into account, the structure model was then refined in $R\bar{3}c$. The satisfactory refinement proved that $R\bar{3}c$ was indeed the correct space group, despite the previous failure of obtaining a reasonable initial model. The increase of symmetry and hence the decrease of the number of variables did not lower the quality of the structure solution, which preserved the low agreement factors, small residue peaks on the final difference Fourier map, as well as thermal ellipsoids with fair sizes and reasonable shapes. After the final selection of the space group and adjustment of the parameters for $R\bar{3}c$ accordingly, the secondary extinction coefficient[63] was refined. The occupancies of the two cation

sites and that of the interstitial atom were also examined. Lacking significant deviations from 100% occupancy (Zr2 99.8(3)%, Cs^+ 100.8(1)%, Mn 98.6(4)%) after both multiplicities and thermal parameters were allowed to vary, these positions are reported as fully occupied. Other important refinement parameters are listed in Table 27.

Structure description The positional and thermal parameters for $Cs_3(ZrCl_5)Zr_6Cl_{15}Mn$ are listed in Table 28. Due to the fact that the cell constants from an X-ray powder diffraction analysis generally have higher accuracy, these were employed to calculate the distances and angles (Table 29).

The formula, the functions of each structural element, and the distances indicate $Cs_3(ZrCl_5)Zr_6Cl_{15}Mn$ is an 18 e^- cluster. Its structure is composed of three main fragments, the cluster network, the counter-anion complex $ZrCl_5^-$, and the cations Cs^+ (Figure 28). Another way to analyze the structure is to dissect it into close packed layers.

$Cs_3(ZrCl_5)Zr_6Cl_{15}Mn$ contains $[Zr_6Cl^i_{12}Mn]Cl^a_6$ cluster units which are very similar to single crystal work results of the other two Mn cluster compounds ($LiZr_6Cl_{14}Mn$, $Li_2Zr_6Cl_{15}Mn$) in terms of the Zr-Zr, Zr-Mn as well as Zr-Cl^i (Zr-Cl1, Zr-Cl2) distances. The distortion of the Zr_6 core occurs in such a way that the resultant trigonal antiprism is elongated along $\vec{c}$. This trigonal distortion is not severe in the sense that Zr-Zr distances differ by only 0.8% (0.0277 Å, 35σ), and the discrepancy of the angles at Mn from those for an ideal octahedron is small (180° and 89.57(1)° vs 180°and 90°). Since the cluster has 18 electrons, the cause of the observed distortion is likely to be a matrix effect. Considering the cluster core without the chlorine atoms, each

Table 28. Positional and Thermal Parameters for $Cs_3(ZrCl_5)Zr_6Cl_{15}Mn$

	x	y	z	B_{11}
Zr1	0.00605(3)	0.15526(3)	0.03995(1)	1.100(9)
Zr2	0	0	1/4	1.67(2)
Mn	0	0	0	0.86(3)
Cs	1/2	0	0	2.89(1)
Cl1	0.16505(8)	0.15871(8)	0.08461(3)	1.91(3)
Cl2	0.32545(80	0.15362(9)	0.00001(3)	1.01(2)
Cl3	0.6553(1)	0	1/4	1.67(4)
Cl4	0.1831(1)	0	1/4	2.05(4)
Cl5	0	0	0.18048(5)	3.13(5)

B_{22}	B_{33}	B_{12}	B_{13}	B_{23}	B_{eq}
0.934(8)	0.95(1)	0.527(6)	-0.03(1)	-0.13(1)	0.988(6)
B_{11}	1.63(3)	$1/2B_{11}$	0	0	1.66(1)
B_{11}	0.75(4)	$1/2B_{11}$	0	0	0.83(2)
2.89(1)	1.90(1)	1.785(9)	-0.01(1)	0.03(1)	2.408(8)
1.95(3)	1.48(3)	1.19(2)	-0.74(3)	-0.69(3)	1.68(2)
1.90(3)	1.70(3)	0.60(2)	-0.01(3)	0.32(3)	1.60(2)
1.48(5)	1.82(5)	$1/2B_{22}$	-0.30(2)	B_{13}	1.68(3)
3.00(8)	2.57(6)	$1/2B_{22}$	0.08(3)	B_{13}	2.44(4)
B_{11}	1.67(6)	$1/2B_{11}$	0	0	2.64(3)

Table 29. Important Distances and Angles in $Cs_3(ZrCl_5)Zr_6Cl_{15}Mn$

Distances (Å)						
Zr-Mn	Zr1-Mn	x6	2.4153(4)	Zr2-Cl4(eq)	x3	2.361(1)
Zr-Zr	Zr1-Zr1	x6	3.4019(8)	Zr2-Cl5(ax)	x2	2.446(2)
		x6	3.4296(7)	$\bar{d}$		2.395
	$\bar{d}$		3.4156			
Zr-Cl^{i}	Zr-Cl1	x6	2.566(1)			
		x6	2.567(1)			
	Zr-Cl2	x6	2.583(1)	Cs-Cl1	x2	3.582(1)
		x6	2.588(1)	Cs-Cl2	x2	3.667(1)
	$\bar{d}$		2.576		x2	3.868(1)
Zr-Cl^{a-a}	Zr-Cl3	x6	2.7294(7)	Cs-Cl3	x2	3.6814(6)
				Cs-Cl4	x2	3.5785(5)
				Cs-Cl5	x2	3.7538(4)
				$\bar{d}$		3.688
Angles (°)						
Zr1-Mn-Zr1		x3	180			
		x6	89.54(1)			
		x6	90.46(1)			

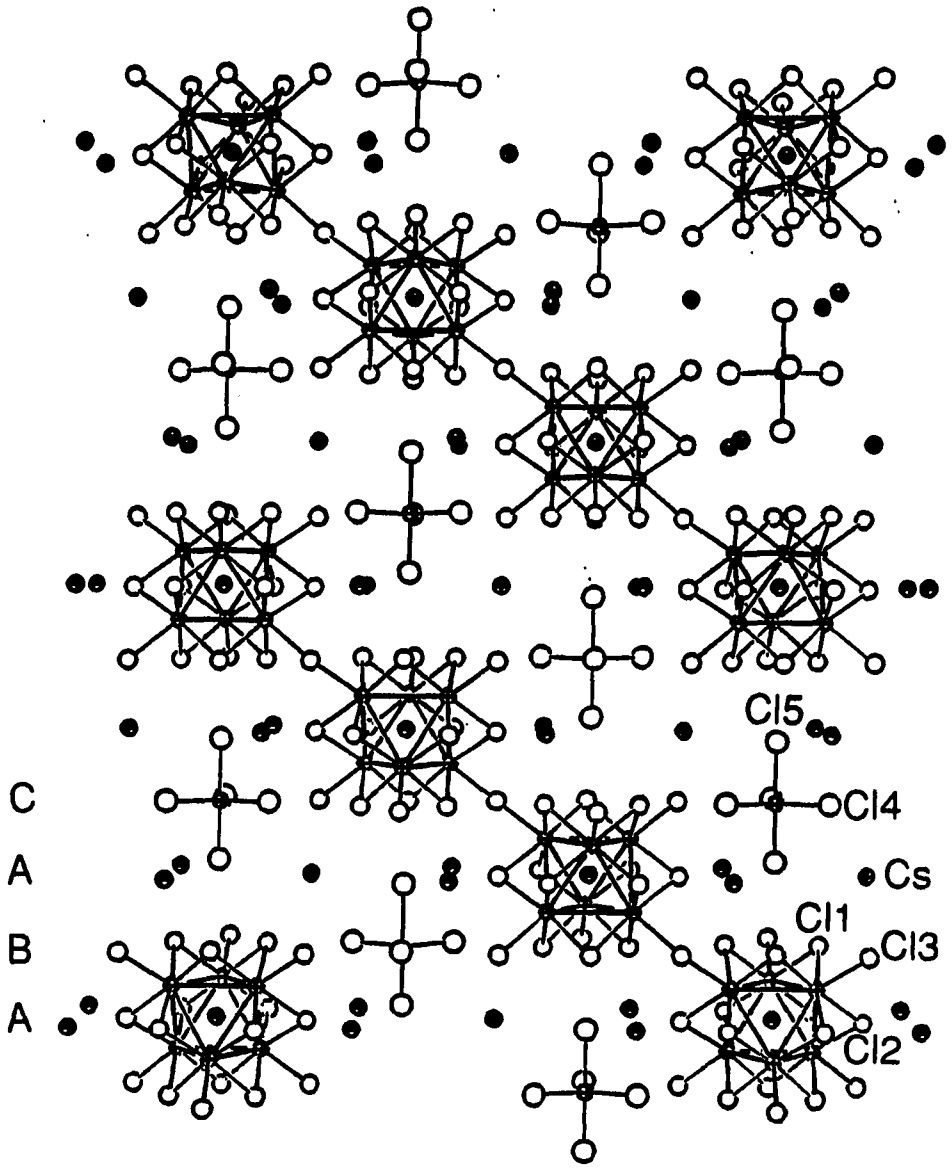

Figure 28. The [110] projection of $Cs_3(ZrCl_5)Zr_6Cl_{15}Mn$ (90% probability, $\vec{c}$ vertical) showing the structural elements and the close packing sequence

cluster unit has six Cs^+ ions around its waist capping the triangular faces (Zr1-Cs 4.70 Å, 5.83 Å, 5.96 Å), and six additional Cs^+ ions at greater distances (5.02 Å, 6.09 Å) bridging the edges of the other two triangular faces normal to the $\vec{c}$ axis. The arrangement of these 12 Cs^+ ions with respect to the cluster core creates an anisotropic electric field that is stronger around the waist of the cluster, resulting in a trigonal elongation of the Zr_6 fragment. Although each cluster also has two Zr2 atoms at a Zr1-Zr2 distance of 6.07 Å capping the two faces normal to the $\vec{c}$ axis, the effect of these Zr atoms on the observed cluster distortion appears to be secondary or even negligible, not only because of the greater distance, but also due to the fact that the Zr2 atom is well shielded by its surrounding Cl's so that $ZrCl_5$ should be considered as a whole structural element that carries a negative charge.

The backbone of the structure is the $[Zr_6Cl^i_{12}Mn]Cl^{a-a}_{6/2}$ network. The connectivity between clusters is essentially the same as that in Nb_6F_{15}.[17] Yet, two major differences are noticed when the two structure types are compared. First, there are two identical interpenetrating cluster nets in Nb_6F_{15} while in $Cs_3(ZrCl_5)Zr_6Cl_{15}Mn$, the second one is missing, leaving large voids in the structure that are now propped open with $ZrCl_5^-$ and Cs^+ ions. Second, the connections between clusters are bent at Cl^{a-a} [Zr1-Cl3-Zr1 133.39(6)°] whereas those in Nb_6F_{15} are linear (Figure 29). The formation of this type of lattice can be rationalized as follows. Due to the specific requirements of the stoichiometry, the large size and high content of the countercation Cs^+, an open network is preferred. Since Cs^+ is too large to fit into a lattice of the Nb_6F_{15} type, distortions of the cluster framework occur. With the other

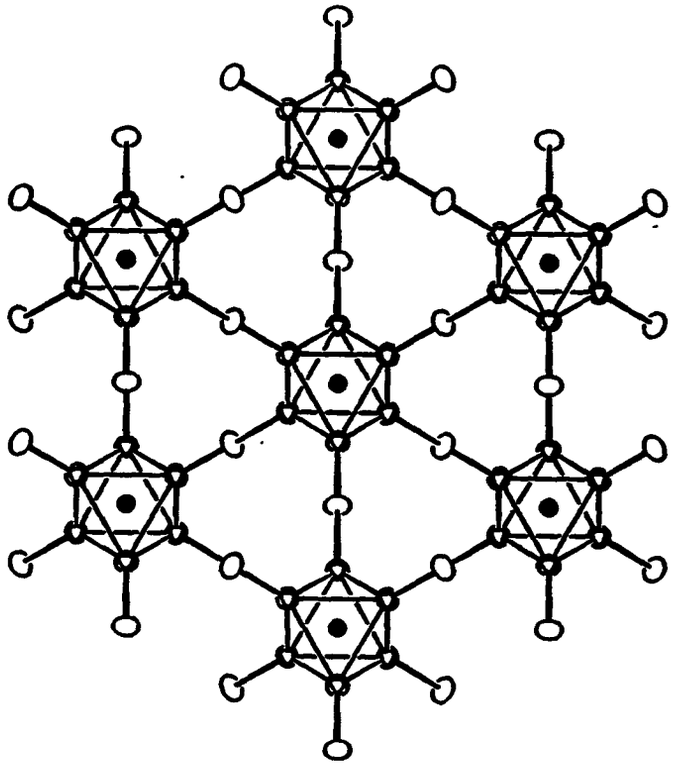

Nb_6F_{15}

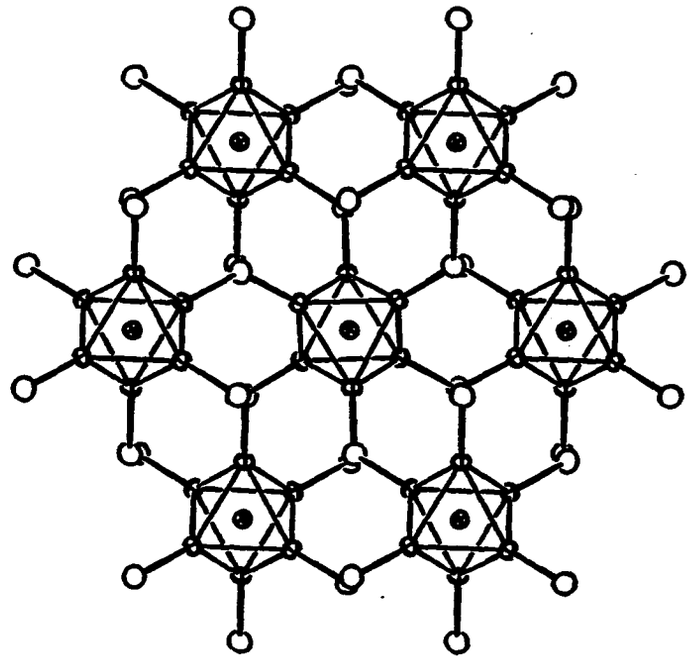

$Cs_3(ZrCl_5)Zr_6Cl_{15}Mn$

Figure 29. The comparison of the cluster linkages at the Cl^{a-a} atom. The view is along the [111] direction for Nb_6F_{15} and along the [001] direction for $Cs_3(ZrCl_5)Zr_6Cl_{15}Mn$

structural fragments available, the lattice preserves one cluster net and replaces the other one with counter ions. The loss of linearity at Cl^{a-a} can be understood as a requirement of a higher space-filling efficiency. The volume of each formula of $Cs_3ZrCl_5Zr_6Cl_{15}Mn$ with one cluster and counter ions is 843 $Å^3$, while the volume of two formulas of $Li_2Zr_6Cl_{15}Mn$ is 1107 $Å^3$. This comparison indicates that the three Cs^+ and a $ZrCl_5^-$ group can not make up the space otherwise occupied by a cluster, and this leads to the collapse or rearrangement of the cluster network. In this process, the connectivity between clusters in one of the networks is preserved without compressing the Zr-Cl^{a-a} bonds [Zr1-Cl3 2.7281(7) Å vs 2.7618(6) Å in $Li_2Zr_6Cl_{15}Mn$]. However, the cluster network is twisted and the Zr-Cl^{a-a}-Zr bond is bent (Figure 30) so that both the space filling and symmetry requirements of a close packed lattice are fulfilled.

As mentioned earlier, this trigonal twist is equivalent to the structure relation between ReO_3 (space group Pm3m) and PdF_3 (space group $R\bar{3}c$),[85] except that the latter structure transition starts with ReO_3 that has a single cubic network, half of Nb_6F_{15}, and ends at RhF_3 which does not contain any other fragments besides $RhF_{6/2}$ octahedra. Due to the size increase of the structure element from one atom (Re or Rh) to a cluster ($[Nb_6F^i_{12}]$ or $[Zr_6Cl^i_{12}Mn]$), the space left by the main networks also expands, and this is filled with either the second cluster net or counter ions in the cluster compounds. An additional difference between these two pairs of structure variations is the doubling of the $\vec{c}$ axis accompanying the twist in the cluster systems, because the structural element is no longer spherical. Since the orientations of the clusters

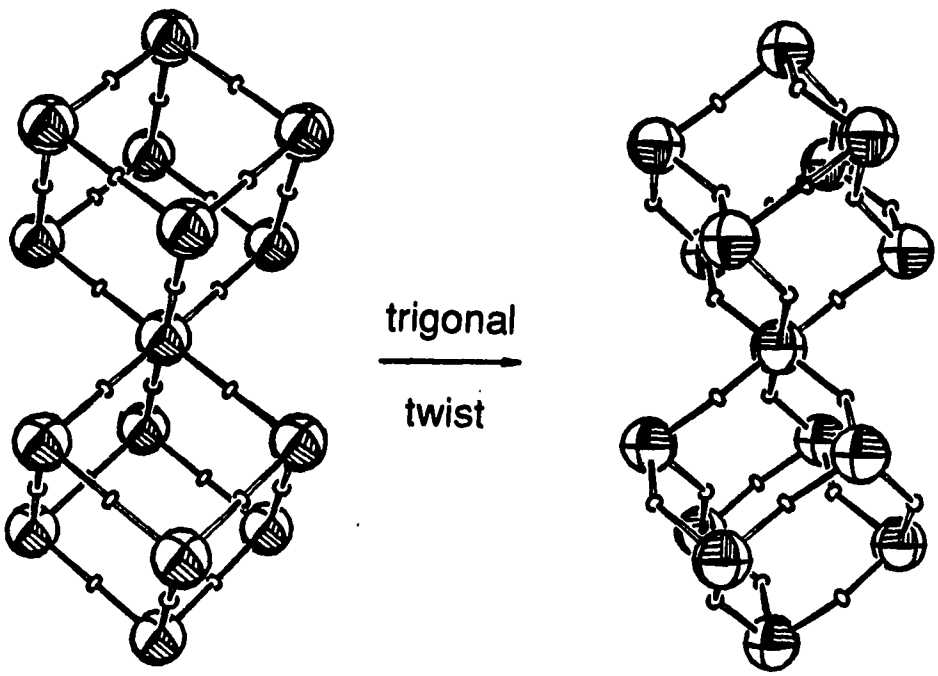

Figure 30. The effect of the trigonal twist on the cluster network (3-fold axes vertical). The larger spheres represent the cluster core $[Zr_6Cl^{i}_{12}Z]$, and the smaller ones are Cl^{a-a} atoms

are changed after the trigonal twist, the repeating unit normal to the close packed layers (the [111] direction in Nb_6F_{15}, $(ABC)_2$; the $\vec{c}$ axis in $Cs_3ZrCl_5Zr_6Cl_{15}Mn$, $(ABAC)_3$) is doubled.

The presence of the $ZrCl_5^-$ unit in $Cs_3ZrCl_5Zr_6Cl_{15}Mn$ (Figure 31) is the most intriguing feature of this structure, as it is believed to be the first example of Zr^{4+} with trigonal bipyramidal configuration. Generally speaking, coordination numbers of five are less common than four and six. Zirconium is considered having very little chemistry of CN=5. On the other hand, one of well known example of trigonal bipyramidal complex ions in the literatures is a group of compounds with the formula $[M(NH_3)_6][M'Cl_5]$ (M trivalent cations, M'=Cu, Hg, Cd),[86] in which the presence of a large cation, $[M(NH_3)_6]^{3+}$, is required. In a way, the $ZrCl_5^-$ units found in $Cs_3ZrCl_5Zr_6Cl_{15}Mn$ are similar to this group for they are also well shielded by Cs^+ cations and separated from each other by clusters.

The complex ion $ZrCl_5^-$ has D_{3h} point symmetry that is higher than the symmetry of the central atom Zr2 (D_3), which also takes the arrangement of cluster units in space into consideration. The Zr to apical Cl distances agrees with the sum of crystal radii[66] of Cl^- (1.67 Å) and five-coordinate Zr^{4+} (0.80 Å) which was obtained from Zr^{4+} in a square pyramidal environment in K_2ZrO_3, the only Zr^{4+} example of coordination number of five cited in Shannon's table of crystal radii.[66] On the contrary, the Zr to equatorial Cl distances are slightly shorter, which is acceptable because the lack of reliable values to compare with and, moreover, the symmetry change of the coordination polyhedron. The small size of Zr^{4+} is essential to the existence of this $ZrCl_5^-$ unit and

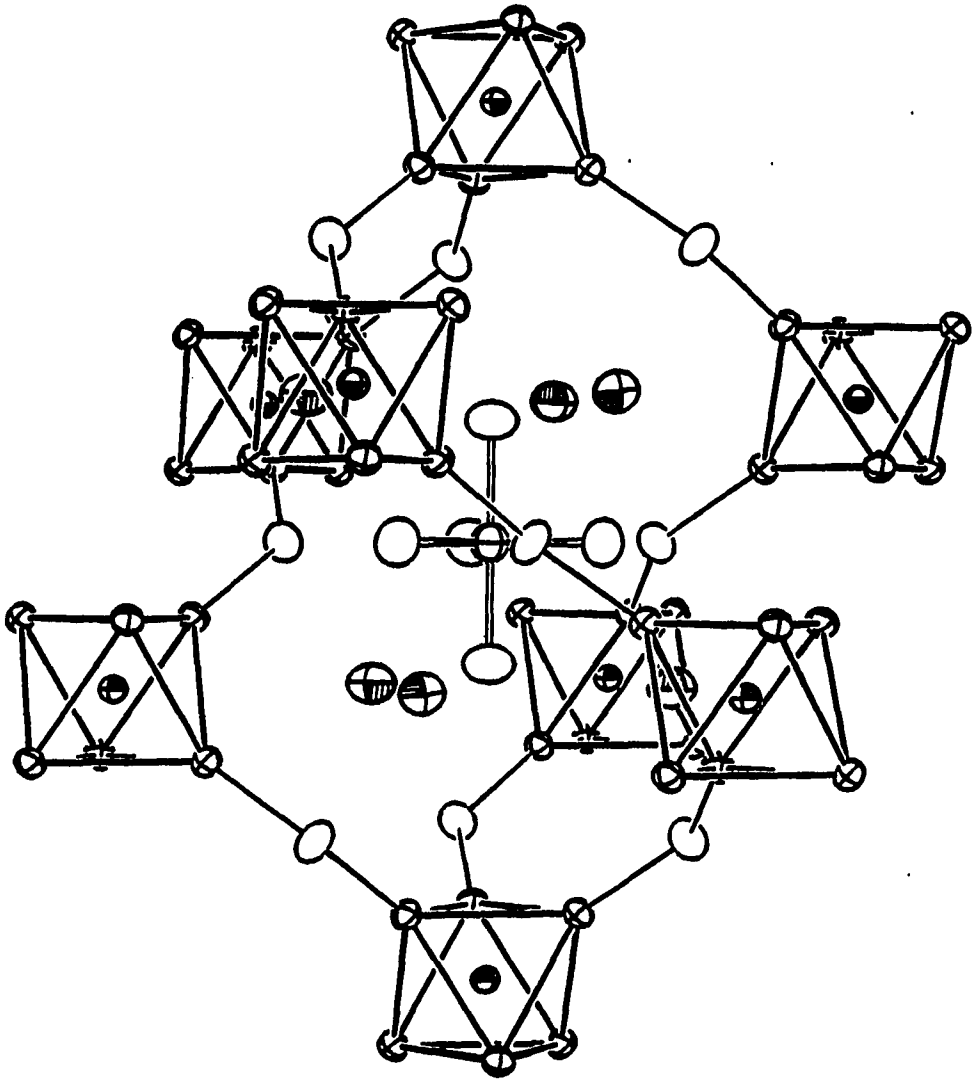

Figure 31. The $ZrCl_5^-$ anion (D_{3h} symmetry) and Cs^+ cations prop the cluster network in $Cs_3(ZrCl_5)Zr_6Cl_{15}Mn$ open (90% probability, 3-fold axis vertical). The shaded ellipsoids are Cs atoms

to the formation of this structure type, since this Zr is not between the close packed layers, but in a small triangular interstice within a close packed layer. This criterion was used as a guideline when other cations such as Cu^{2+} (CN=5, 0.71 Å) or Nb^{5+} (CN=6, 0.78 Å) were chosen to replace the Zr^{4+} at this position. Another interesting feature of this $ZrCl_5$ group is the fact that it does not share any Cl atoms with the cluster network. This observation is at present unique, since in the rest of the Zr-Cl cluster phases, the Cl atoms around a countercation also take part in the cluster formation. For instance, the Cl atoms around the Zr^{4+} ion in the double salt structure ($K_2ZrCl_6 \cdot Zr_6Cl_{12}H$) serve as the terminal Cl^a of the cluster at the same time. From this point of view, $Cs_3(ZrCl_5)Zr_6Cl_{15}Mn$ is a double salt containing two complex anions that are truly independent of each other.

The countercation Cs^+ in this structure behaves rather normally, yet it is still indispensable. It takes a position as a member of the close packed lattice, and it has 12 Cl atoms in its first coordination sphere (Figure 32). The averaged Cs-Cl distance is almost ideal for a 12-coordinate Cs^+ [crystal radii: Cl^- 1.67 Å, Cs^+(CN=12) 2.02 Å].[66] Cs^+ possesses C_1 symmetry and has a regular coordination polyhedron with the surrounding Cl's in a cubic-close-packing pattern. Its thermal ellipsoids is nearly spherical. There are 12 Cs^+ around each cluster and six around each $ZrCl_5^-$ unit. The large size of Cs^+ helps to expand the lattice which might play an important role in forming this structure type.

The structure of $Cs_3(ZrCl_5)Zr_6Cl_{15}Mn$ consists of close packed layers as many other Zr-Cl cluster compounds. Its $\vec{c}$ parameters corresponds to

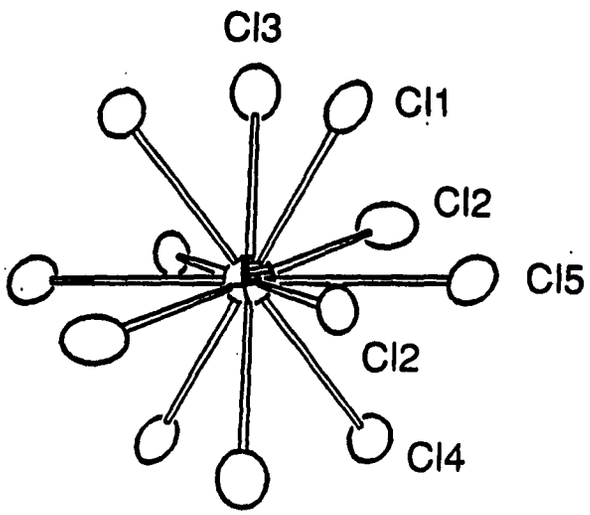

Figure 32. The coordination environment of Cs^+ in $Cs_3(ZrCl_5)Zr_6Cl_{15}Mn$. Cs^+ sits on an inversion center (90% probability)

12 close packed layers (Figure 24), which can be labeled as $...(ABAC)_3...$ or as $(ch)_6$. Within a unit cell, each layer has 12 close packing positions. Half of the layers (B or C) are occupied only by Cl atoms, and the other half (A) are occupied by 1 Mn, 3 Cs and 8 Cl atoms. The layers are related to each other either by R-centering ($\Delta z = 1/3$ c) or by c-glides ($\Delta z = 1/2$ c) perpendicular to $\vec{a}$ or $\vec{b}$. All of the layers are saturated without leaving a single close-packing site vacant; moreover, the layers labeled as B or C also have an extra Zr (Zr2) sitting in some of the trigonal interstices. These layers are essentially flat except the apical Cl in the $ZrCl_5$ group (Cl5) is 0.49 Å off of the center of its layer due to the strong interaction with the Zr^{4+} (Zr2). In contrast to what observed for the 6-18 phases that have significantly different spacing between close packed layers, the distances from any close packed layer to its neighboring layers in $Cs_3(ZrCl_5)Zr_6Cl_{15}Mn$ are approximately equal as the result of the direct cluster linkage and, therefore, the same distribution of cluster forming Zr atoms between each pair of layers. Finally, if the structure elements are defined as $[Zr_6Cl_{15}Mn]^{2-}$ and $[Cs_3ZrCl_5^-]^{2+}$ units while ignoring their geometry details, the structure follow the cubic close packing manner.

<u>$KZr_6Cl_{15}Fe$ and other compounds with structures related to the $CsNb_6Cl_{15}$-type</u>

A large number of centered Zr-Cl cluster phases have structures related to the $CsNb_6Cl_{15}$-type.[46] Accompanying the wide range of chemical compositions, several structure variations of the original type were observed, namely, the $KZr_6Cl_{15}C$,[47] $KCsZr_6Cl_{15}B$,[47] and $KZr_6Cl_{15}Fe$ types.

Besides the fact that the Nb cluster is empty, the basic difference between $KZr_6Cl_{15}C$ and $CsNb_6Cl_{15}$ ($\sim CsZr_6Cl_{15}C$)[47] is the locations of the countercations, and in $KCsZr_6Cl_{15}B$ the cation positions of different sizes in both parent structures are inherited. The above structure variations involve modifications of the cation sites while leaving the cluster framework intact. On the contrary, when the transition metals are introduced into the Zr-Cl cluster systems, the expansion of the cluster cores may result in a third type of structure modification in which the linear cluster chains in the $CsNb_6Cl_{15}$ structure are bent and a superstructure of the parent lattice is observed. The single crystal work on $KZr_6Cl_{15}Fe$ established this new structure modification and provided examples to rationalize a correlation between structure and cluster size.

Synthesis The compounds presented in Table 30 were made via stoichiometric reactions that carried out between 800 to 850°C for about 20 days. The yields of the desired 6-15 phases were over 90%, and small amounts of ZrCl and $ZrCl_4$ were sometimes observed as impurities. Characteristic of this group of compounds, the cluster phases were always obtained in the well crystallized form. Crystals with nicely defined facets, rod or hexagonal prism shapes, and sizes suitable for X-ray analyses were easily obtained without special efforts. In addition, many of these compounds were often observed as crystalline minor phases or alternative products from reactions that were originally designed to synthesize other cluster phases.

The centering elements of this group of new compounds are at present limited to Fe and Co. Attempts to synthesize Mn analogues with

Table 30. Cell Parameters (Å) and Volumes (Å^3) for Compounds with Structures Related to the $CsNb_6Cl_{15}$-Type[a]

	a	b	c	V	Space group
$KZr_6Cl_{15}Fe$	18.928(2)	14.170(2)(x2)	9.946(1)(x2)	2667.6(6)(x4)	Amma[b]
$RbZr_6Cl_{15}Fe$	18.872(2)	14.176(2)(x2)	9.915(2)(x2)	2652.7(8)(x4)	Amma[b]
$CsZr_6Cl_{15}Fe$	18.899(5)	14.197(5)	9.890(3)	2653(1)	Pmma
$Cs_xZr_6Cl_{15}Co$	18.824(3)	14.186(2)	9.882(2)	2638.9(9)	Pmma

[a]All values are from Guinier powder diffraction data.

[b]A nonstandard setting of Cmcm (No. 63) for better comparison.

structures related to $CsNb_6Cl_{15}$ were not successful. Reactions planned to make $M_2Zr_6Cl_{15}Mn$ yielded the corresponding $MZr_6Cl_{14}Mn$ phases (M = K, Rb), or a mixture of $Cs_3(ZrCl_5)Zr_6Cl_{15}Mn$[10] and $CsZr_6Cl_{14}Mn$ when Cs was employed as the countercation. In the Fe-centered cluster systems, the smallest alkali metal that forms a compound of this type is K. A reaction aimed at $NaZr_6Cl_{15}Fe$ produced the ternary cluster phase $Zr_6Cl_{14}Fe$, (Nb_6Cl_{14} type)[48] while $LiZr_6Cl_{15}Fe$ has the Nb_6F_{15} structure.[7] As no experiment was conducted using Rb^+ or K^+ as the countercation, the only known example of Co-centered cluster in this family is $Cs_xZr_6Cl_{15}Co$. Since this Co phase has a cluster electron count of 18 + x, attempts were made to change the Cs content by varying the ratio of the starting materials. However, reactions started with x = 1/4, 1/2, or 3/4 all yielded $Zr_6Cl_{15}Co$ and $Cs_xZr_6Cl_{15}Co$ as the major phases, and the proportion of $Zr_6Cl_{15}Co$ increased as the Cs content was reduced. This implies that the quaternary Co cluster might has a fixed composition with x close to 1. On the basis of the lattice constants refined from powder diffraction data, no conclusive statement can be made to verify this judgement, mainly because of the difficulties to obtain precise cell parameters from a powder pattern showing multiple phases. Similar to what was observed in the Fe series, reactions starting with $NaZr_6Cl_{15}Co$ and $LiZr_6Cl_{15}Co$ produced the cubic $Zr_6Cl_{15}Co$ phase.

The observed powder patterns of the above compounds can be indexed with $CsNb_6Cl_{15}$[46] as the model. The only noticeable difference between the calculated pattern for the superstructure and that for the parent structure is that the former has one additional reflection corresponding to the doubling of the axes (Cmcm 1,1,0; 2θ = 5.4°, d = 16.4 Å, relative

intensity 6%). It is very difficult to judge the structure type based on the Guinier powder diffraction, due to the low intensity of this reflection and the increasing background in the low angle region. Therefore, the structure assignment of each compound in Table 30 was established by an X-ray single crystal analysis ($KZr_6Cl_{15}Fe$), axial photos taken on a diffractometer ($RbZr_6Cl_{15}Fe$), Weissenberg photos ($CsZr_6Cl_{15}Fe$), or precession photos ($Cs_xZr_6Cl_{15}Co$). Besides the K and Rb compounds, the film studies on $(K,Rb)Zr_6Cl_{15}Fe$ indicated that the cluster phase with mixed cations also has the superstructure. On the other hand, no modifications of any kind have been detected for the cesium salts. An interpretation of these observations will be given after the structure of $KZr_6Cl_{15}Fe$ is presented.

Structure determination The crystals of $KZr_6Cl_{15}Fe$ were obtained from a reaction of stoichiometric amounts of starting materials that was heated at 850°C for 10 days and then annealed at 750°C for 3 days. The yield of the main product which was above 95% contained many black rod-like crystals. The powder pattern that provided over 30 reflections could be indexed with either $CsNb_6Cl_{15}$[46] or $KZr_6Cl_{15}C$[47] as the model, which generate essentially the same calculated powder patterns with subtle differences in intensities. The corresponding subcell was obtained on a SYNTEX diffractometer based on 15 reflections input from a rotation photo. However, axial photos indicated two of the axes were doubled with respect to the values expected for a normal $CsNb_6Cl_{15}$ structure. A set of data was collected on SYNTEX, yet the refinement could not be completed due to the poor working condition of the diffractometer, mainly the insufficient intensity of the incident beam.

Another data set was collected on CAD4, and the supercell was established by indexing 25 reflections located by the SEARCH routine and the succeeding transformation to the C-centered cell. Axial photos were taken to confirm the cell parameters and the lattice type, and to determine the Laue class (mmm). Two octants of data (hkℓ, hk$\bar{\ell}$) of 4° <2θ <50° were collected for the C-centered cell (Table 31).

Considering the large number of variables involved in the refinement, the limited data available, and a reasonable accuracy of the intensity measurements, the criterion for observed reflections was lowered from $3\sigma_I$ to $2\sigma_I$. An empirical absorption correction with four ψ-scan measurements was conducted, and the redundant data were averaged in Laue class mmm, giving $R_{ave.}$ = 3.2%. Based on the reflection conditions (hkℓ, h+k = 2n; h0ℓ, ℓ = 2n), the choices of space group were Cmcm, C2cm and $Cmc2_1$. However, the initial model provided by SHELXS-86 for the most promising space group, the central symmetric Cmcm, was not acceptable in terms of interatomic distances and electron densities. A subgroup of Cmcm, $C222_1$, for which a plausible SHELXS-86 solution was obtained, was chosen as the next candidate with part of the extinction condition lifted. The isotropic refinement of the twelve Zr, two Fe and thirty one Cl atoms gave R = 6.7% and R_w = 9.3%, respectively. Three of the K atoms with full or partial occupancies (K1 = 18(1)%, K2 = 57.6(7)%, K2′ = 100%) were located on the calculated difference Fourier map, while the other fully occupied position (K3) emerged after an empirical numerical absorption (DIFABS)[62] was applied. The sum of these K positions with different multiplicities (8 K1, 4 K2, 4 K2′, and 8 K3) and occupancies gave a total number of 15.76 (8) K for each cell, in

Table 31. Crystal Data for $KZr_6Cl_{15}Fe$

space group	Cmcm (No. 63)
Z	16
a, Å[a]	28.340(4)
b, Å	19.892(2)
c, Å	18.928(2)
V, Å^3	10670(2)
crystal dimen, mm	0.3 x 0.1 x 0.1
data collection instrument	ENRAF NONIUS CAD4
scan mode	ω-2θ
$2\theta_{max}$, deg	50
reflections	$\pm h,k,\ell$
measured	9876
observed ($I>2\sigma_I$)	3677
observed independent	1977
absorp coeff μ, cm^{-1} (Mo Kα)	44.3
range of transm coeff	0.95 - 1.00
R_{ave}, %	3.2
second ext coeff	–
R, %	3.1
R_w, %	3.5
largest residue peak, e$^-$/Å^3	±1.2 (0.4 Å, K2′)

[a]Guinier powder diffraction data (61 observations).

agreement with the formula $KZr_6Cl_{15}Fe$ (Z = 16). Although the isotropic refinement of all atoms resulted in R = 4.9%, the shifting of the parameters was significant and no satisfying convergence could be reached. Anisotropic refinement of all atoms was impossible because the limited number of observed reflections.

Examining the structure solution in space group $C222_1$, one noticed that many of the atoms seemed to be on special positions in a higher symmetry space group, and the ORTEP[64] picture also implied the structure could be centrosymmetric. Taking the observed systematic extinction conditions into consideration, the solution was transformed into the supergroup of $C222_1$, Cmcm. Refinement with the proper symmetry constraints were successful and, because of the reduction of the atom numbers, anisotropic refinement of all of the atoms became possible. As a combined result of the anisotropic refinement and elimination of the coupling between atoms observed in $C222_1$, the quality of the solution was improved significantly. Although the number of total variables was reduced from 290 (anisotropic refinement for Zr and Fe) to 250 (anisotropic for all atoms), R and R_w decreased by 0.5%, and slightly smaller residue peaks on the final difference Fourier map and the thermal parameters of similar sizes for all the atoms were produced. The more direct evidence supporting the centrosymmetric space group was the significant decrease of the standard deviations of the positional and thermal parameters by factors of two to four. In addition, the solution in space group Cmcm is reasonable in terms of distances and provides reasonable explanations for the formation of the superstructure.

The refined multiplicities of Fe1 and Fe2 were not significantly different from full occupancy [Fe1 100.4(4)%, Fe2 97.8(4)%], and therefore these positions are reported as fully occupied. With the additional symmetry elements in Cmcm, K1 now is sitting on a mirror plane, and a pair of equivalent K3 positions are generated by the nearby inversion center. The two symmetry-related K3 sites are 3.01 Å apart and as the multiplicity increased from eight in $C222_1$ to sixteen in Cmcm, the occupancy is dropped to 54(1)%. Examining the location of K3 atoms, it was noticed that they were derived from the Cs2 position in $CsNb_6Cl_{15}$, which is a cation position with $C_{2/h}$ symmetry. Because of the lattice distortion and expansion, the former cation site on the symmetry element is now split into two general positions, each 50% occupied in Cmcm. As expected, refining the K3 position on the inversion center with full occupancy resulted in huge thermal parameters corresponding to mean-square amplitudes of vibration of over two Ångstroms, accompanied by an increase of residue peaks and agreement factors. Re-examining the situation in $C222_1$, where K3 was refined as a 100% occupied general position, it was noticed that the K3 and its empty counterpart sites were about the same size. This raised questions about this model as there is no obvious reason for K3 to select one of the two positions with the same chemical environment. The K3 refinement in $C222_1$ could be the result of the strong coupling between a pair of atoms that are related by pseudo symmetries, especially as they are close to each other and undergo substantial thermal motions as in this case. Based on the satisfactory refinement of the entire structure in Cmcm, it is clear that the contribution from K3 was not sufficient to allow refinement of

the lower symmetry structure even if there were indeed one fully occupied position in $C222_1$. Therefore, the solution with split K3 atoms was accepted. The multiplicities of the four positions sum up to give K:cluster ratio of 16.5(6):16 (8 K1/cell, occupancy 19(1)%; 4 K2/cell, occupancy 64(1)%, 4 K2′/cell, occupancy 100%; 16 split K3/cell, occupancy 54(1)% each), which agrees with the 18 e^- rule.

The final difference Fourier map showed only ghost peaks of ±1.2 $e^-/Å^3$ that are 0.4 Å away from K2′. The structure solution is presented in Table 32 in the standard setting of Cmcm. It may be converted to a nonstandard setting in Amma through a rotation of the axes (a′ = c, b′ = a, c′ = a) and a shift of the origin by -1/4b. The atom coordinates thus obtained can be compared with the pseudo parent structure in Pmma. For the purpose of emphasizing the structure relationships between this superstructure and the $CsNb_6Cl_{15}$ structure, the atoms that are split from one position in the original structure are listed in pairs (Table 32).

Structure description The structure of $KZr_6Cl_{15}Fe$ may be derived from that of $CsKZr_6Cl_{15}B$,[47] which has one additional cation position, K, than $CsNb_6Cl_{15}$.[46] The modifications of the local geometry around the Cl^{a-a} atoms, the shifting of the cluster chains, and the selective filling of the cation positions lead to the loss of symmetry and the formation of the superstructure.

Similar to those in all the other related structures, there are two crystallographically distinctive clusters in $KZr_6Cl_{15}Fe$ that form two different chains, namely, the zigzag chain along $\vec{c}$ and the bent chain along $\vec{b}$ (Figure 33). As Fe is encaptured as the centering atom, the

Table 32. Positional and Thermal Parameters for $KZr_6Cl_{15}Fe$

Atom	x	y	z	B_{11}
Zr1	0.06046(4)	0.18219(6)	0.03066(6)	1.35(4)
Zr1′	0.43940(4)	0.15496(6)	0.03003(6)	1.43(4)
Zr2	0	0.22229(9)	0.61959(9)	1.37(6)
Zr2′	0	0.30598(8)	0.37991(9)	1.39(6)
Zr3	0.18750(4)	0.07834(6)	0.15899(7)	1.46(4)
Zr3′	0.30846(4)	0.06636(6)	0.15912(7)	1.44(4)
Zr4	0.25326(6)	0.19271(8)	1/4	1.54(6)
Zr5	0.25759(6)	0.45188(9)	1/4	1.55(7)
Fe1	0.000	0.2637(1)	0.4996(2)	1.20(8)
Fe2	0.24795(9)	0.07221)	1/4	1.18(8)
Cl1	0.1239(1)	0.0880(2)	0.0586(2)	3.4(1)
Cl1′	0.3745(1)	0.0653(2)	0.0626(2)	2.7(1)
Cl2	0.2653(2)	0.3225(3)	1/4	6.1(3)
Cl3	0	0.8266(4)	1/4	5.2(4)
Cl3′	0	0.3580(4)	1/4	3.9(3)
Cl4	0.12717(9)	0.2635(2)	0.0020(2)	1.1(1)
Cl5	0	0.0923(2)	0.0663(3)	3.3(2)
Cl5′	0	0.5655(2)	0.0668(3)	2.5(2)
Cl6	0.4360(1)	0.3651(2)	0.0949(2)	2.8(1)
Cl6′	0.0639(1)	0.3939(2)	0.0950(2)	2.7(1)
Cl7	0.0632(1)	0.2217(2)	0.1596(2)	2.4(1)
Cl7′	0.4375(1)	0.1935(2)	0.1590(2)	2.1(1)
Cl8	0.1207(2)	0.0834(2)	1/4	1.7(2)
Cl8′	0.1244(2)	0.5583(2)	1/4	1.1(2)
Cl9	0.2485(1)	0.0722(2)	0.0587(2)	2.6(1)
Cl10	0.1904(1)	0.2072(2)	0.1551(2)	2.6(1)
Cl10′	0.3161(1)	0.1942(1)	0.1546(2)	2.5(1)
Cl11	0.3220(2)	0.4500(2)	0.1540(2)	2.7(1)
Cl11′	0.1950(1)	0.4381(2)	0.1534(2)	2.5(1)
K1	0.379(1)	0.322(2)	1/4	2(1)
K2	0	0.1063(6)	1/4	3.3(5)
K2′	0	0.550(1)	1/4	13(1)
K3	0.2659(6)	0.3064(7)	0.0486(7)	29(1)

B_{22}	B_{33}	B_{12}	B_{13}	B_{23}	B_{eq}
2.30(4)	1.40(4)	0.38(5)	−0.14(5)	0.10(5)	1.69(2)
2.23(5)	1.12(4)	−0.31(4)	0.11(5)	0.09(4)	1.59(2)
2.15(7)	0.95(7)	0	0	−0.03(7)	1.49(3)
2.29(8)	0.75(6)	0	0	−0.11(6)	1.48(3)
1.61(5)	1.77(5)	0.04(4)	−0.43(4)	−0.08(5)	1.61(2)
1.49(4)	1.56(5)	0.02(4)	0.25(4)	−0.11(4)	1.50(2)
0.95(8)	1.65(6)	0.01(6)	0	0	1.38(3)
1.02(7)	2.25(7)	−0.02(6)	0	0	1.61(4)
1.7(1)	0.92(8)	0	0	−0.20(9)	1.29(4)
0.94(9)	1.50(8)	0.01(8)	0	0	1.21(4)
3.1(1)	3.7(2)	1.4(1)	−2.2(1)	−1.1(1)	3.40(8)
2.8(1)	3.3(1)	−0.9(1)	1.7(1)	−0.9(1)	2.94(7)
0.8(2)	7.0(4)	0.4(2)	0	0	4.6(1)
2.5(3)	0.7(2)	0	0	0	2.8(2)
3.9(3)	1.0(3)	0	0	0	2.9(2)
3.8(1)	2.3(1)	−0.1(1)	0.0(2)	0.7(1)	2.40(6)
2.4(2)	2.8(2)	0	0	0.8(2)	2.8(1)
2.1(2)	2.7(2)	0	0	0.6(2)	2.4(1)
3.5(1)	1.9(1)	1.2(1)	−0.1(1)	−0.4(1)	2.75(7)
3.3(1)	1.6(1)	−1.3(1)	0.3(1)	−0.5(1)	2.52(6)
3.2(1)	1.3(1)	0.5(1)	−0.4(1)	0.0(1)	2.31(6)
3.4(2)	1.4(1)	−0.8(1)	0.2(1)	−0.1(1)	2.28(6)
2.8(2)	3.1(2)	0.3(2)	0	0	2.5(1)
3.5(2)	2.1(2)	−0.0(2)	0	0	2.2(1)
3.5(1)	1.4(1)	0.0(1)	−0.1(2)	−0.3(1)	2.52(6)
1.9(1)	2.7(1)	0.5(1)	−0.9(1)	0.2(1)	2.40(7)
1.6(1)	2.8(1)	−0.1(1)	1.1(1)	0.4(1)	2.31(7)
2.0(1)	3.7(2)	0.4(1)	1.3(1)	−0.3(1)	2.80(7)
1.9(1)	3.1(2)	−0.2(1)	−0.7(1)	−0.6(1)	2.51(7)
13(3)	8(2)	−0(2)	0	0	7(1)
3.7(5)	2.7(5)	0	0	0	3.3(2)
33(2)	9(1)	0	0	0	18.2(8)
23.8(8)	20.6(8)	16.6(8)	15(1)	19.2(5)	24.5(5)

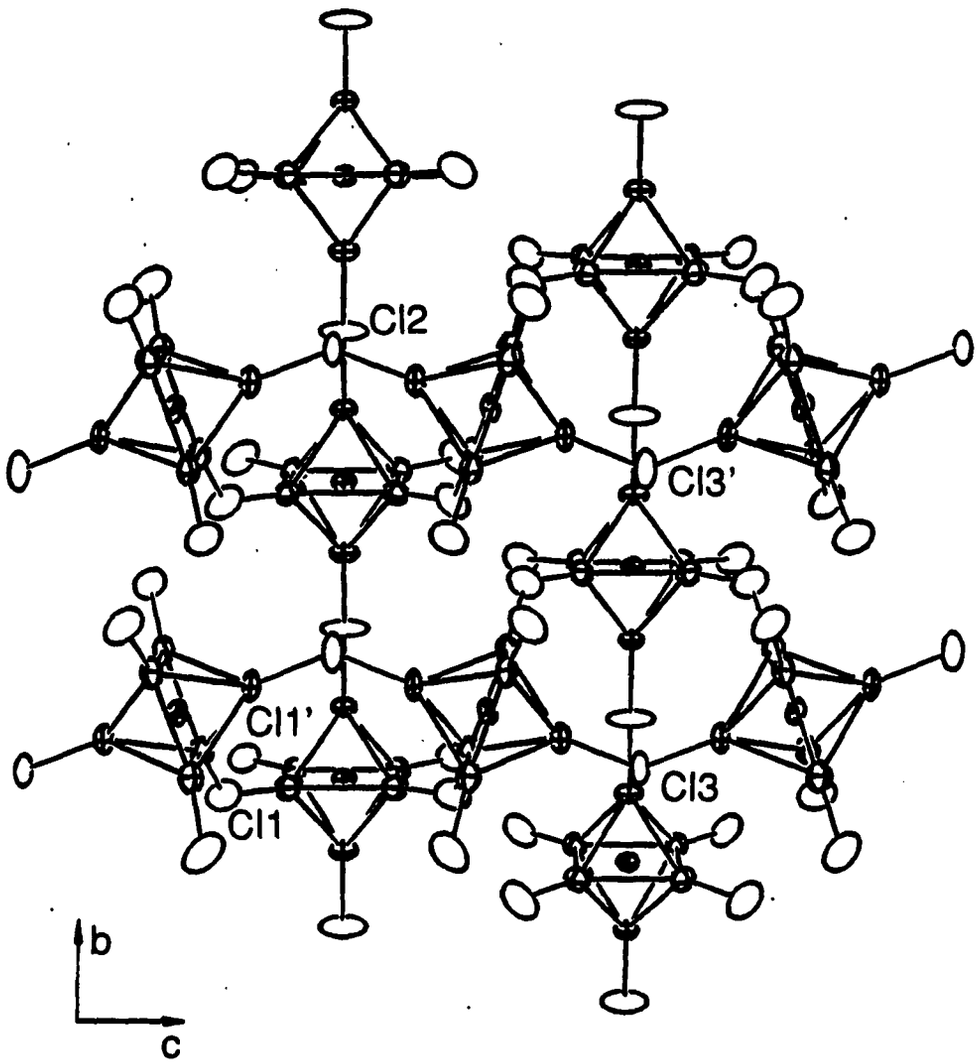

Figure 33. The [T00] projection of $KZr_6Cl_{15}Fe$ showing the two interconnected cluster chains. There are two mirror planes, one parallel to the plane of paper passing through the center of the zig-zag cluster chain, and the other normal to the plane of the paper containing the center of the vertical chains. The cluster chains along the b̄ direction are bent at Cl2 into and out of the plane of the paper. The Cl^i and K atoms are omitted for clarity (90% probability)

cluster cores expand significantly compared with the boron and carbon analogues. An increase of 0.2 Å in Zr-Zr distances is observed, accompanied by a less pronounced increase of Zr-Cl^i distances of 0.02 Å, consistent with the changes known for other Fe centering clusters. The point symmetries of the cluster units in $CsKZr_6Cl_{15}B$ (B1 C_{2h}, B2 C_{2v}) are reduced in $KZr_6Cl_{15}Fe$, saving only the mirror planes. Yet, even without the symmetry imposed by the space group, the cluster units contain the above pseudo symmetries within experimental errors (Table 33). Both clusters deviate from ideal octahedra with the same pattern and similar magnitudes as was observed in $CsKZr_6Cl_{15}B$,[47] which is marked by a compression of the cluster cores along the chain directions. This implies that the distortion of the individual clusters is not the main cause of the formation of the supercell.

On the other hand, comparing $KZr_6Cl_{15}C$[47] and $KZr_6Cl_{15}Fe$ which have the same cation yet a slightly different cluster network, it is obvious that the increasing size of the clusters is responsible for the observed structure modification. Due to the expansion of the cluster core, the terminal chlorines are pushed outward; meanwhile, the Zr-Cl^{a-a} distances are kept almost unchanged. In order to retain the unique inter-chain linkages between the two perpendicular cluster chains that hinder the free expansion of the cluster networks and to provide suitable cation sites for K, the cluster expansion results in the bending of the former linear cluster chains in $KZr_6Cl_{15}Fe$ (Zr4–Cl2–Zr5, 167.6 (3)°). In addition, the zigzag chain becomes more buckled, indicated by a reduction of the angles at Cl^{a-a} from 140° to 137°. The angles at the terminal chlorines that connect the two cluster chains also drop by about 1°.

Table 33. Important Distances and Angles in $KZr_6Cl_{15}Fe$: the Cluster Framework

Distances (Å)	Cluster chain along $\vec{c}$ axis			Cluster chain along $\vec{b}$ axis		
Fe-Zr	Fe1-Zr1	x2	2.428(2)	Fe2-Zr3	x2	2.433(2)
	Fe1-Zr1′	x2	2.428(2)	Fe2-Zr3′	x2	2.432(2)
	Fe1-Zr2	x1	2.416(3)	Fe2-Zr4z	x1	2.401(3)
	Fe1-Zr2′	x1	2.416(3)	Fe2-Zr5	x1	2.399(3)
	$\bar{d}$		2.424	$\bar{d}$		2.422
Zr-Zr	Zr1-Zr1	x1	3.427(2)	Zr3-Zr3	x1	3.445(2)
	Zr1′-Zr1′	x1	3.435(2)	Zr3′-Zr3′	x1	3.441(2)
	Zr1-Zr1′	x2	3.437(2)	Zr3-Zr3′	x2	3.436(2)
	Zr1-Zr2	x2	3.415(2)	Zr3-Zr4	x2	3.408(2)
	Zr1-Zr2′	x2	3.445(2)	Zr3-Zr5	x2	3.423(2)
	Zr1′-Zr2	x2	3.433(2)	Zr3′-Zr4	x2	3.424(2)
	Zr1′-Zr2′	x2	3.410(2)	Zr3′-Zr5	x2	3.413(2)
	$\bar{d}$		3.429	$\bar{d}$		3.425
Zr-Cl[i]	Zr1-Cl4	x2	2.547(3)	Zr3-Cl8	x2	2.562(4)
	Zr1-Cl5	x2	2.567(4)	Zr3-Cl9	x2	2.570(4)
	Zr1-Cl6	x2	2.558(3)	Zr3-Cl10	x2	2.566(3)
	Zr1-Cl7	x2	2.565(3)	Zr3-Cl11	x2	2.568(3)
	Zr1′-Cl4	x2	2.561(3)	Zr3′-Cl8′	x2	2.571(3)
	Zr1′-Cl5′	x2	2.570(4)	Zr3′-Cl9	x2	2.562(3)
	Zr1′-Cl6′	x2	2.559(3)	Zr3′-Cl10′	x2	2.553(3)
	Zr1′-Cl7′	x2	2.559(3)	Zr3′-Cl11′	x2	2.556(3)

	Zr2-Cl6	x2	2.555(4)	Zr4-Cl10	x2	2.546(4)
	Zr2-Cl7′	x2	2.550(3)	Zr4-Cl10′	x2	2.537(4)
	Zr2′-Cl6′	x2	2.562(4)	Zr5-Cl11	x2	2.575(4)
	Zr2′-Cl7	x2	2.565(4)	Zr5-Cl11′	x2	2.568(4)
	$\bar{d}$		2.560	$\bar{d}$		2.561
Zr–Cl[a-a]	Zr1-Cl1	x2	2.649(4)	Zr3-Cl1	x2	2.627(4)
	Zr1′-Cl1′	x2	2.636(4)	Zr3′-Cl1′	x2	2.615(4)
	Zr2-Cl3	x1	2.653(3)	Zr4-Cl2	x1	2.604(5)
	Zr2′-Cl3′	x1	2.668(4)	Zr5-Cl2	x1	2.584(5)
Angles (°)	Cl4-Zr1-Cl5	x2	173.8(1)	Cl8-Zr3-Cl9	x2	174.6(1)
	Cl6-Zr1-Cl7	x2	174.61)	Cl10-Zr3-Cl11	x2	174.4(1)
	Cl4′-Zr1′-Cl5′	x2	174.4(1)	Cl8′-Zr3′-Cl9	x2	173.8(1)
	Cl6′-Zr1′-Cl7′	x2	174.1(1)	Cl10′-Zr3-Cl11′	x2	174.9(1)
	Cl6-Zr2-Cl7′	x2	173.5(1)	Cl10-Zr4-Cl10′	x2	172.8(1)
	Cl6′-Zr2′-Cl7	x2	173.7(1)	Cl11-Zr5-Cl11′	x2	173.0(1)
	ave		174.0	ave	x2	173.9
	Zr2-Cl3-Zr2	x1	137.0(3)	Zr4-Cl2-Zr5	x2	167.6(3)
	Zr2′-Cl3′-Zr2′	x1	137.4(3)			
	Zr1-Cl1-Zr3	x2	131.4(1)	Zr1′-Cl1′-Zr3′	x2	131.1(1)

Shown in Figure 34 is the result of the observed modification of the cluster chains; the repeating unit along the bent chain (b direction) is doubled and contains four (Fe-Zr-Cl2) units. The two chains that used to be linear and parallel to each other now become wavy and paired up by the mirror planes between them, causing the doubling of the second cell dimension [a(Cmcm) = 2b(Pmma)].

When $KZr_6Cl_{15}Fe$ is compared with another 6-15 phase, $LiZr_6Cl_{15}Fe$ (Nb_6F_{15} type), profound differences in the average Zr-Cl^{a-a} distances are noticed. Although its lattice is more expanded, as indicated by the difference in the formula volume of 126 $Å^3$, averaged Zr-Cl^{a-a} distances in $KZr_6Cl_{15}Fe$ (2.661 Å along the zigzag chain, 2.594 Å along the bent chain) are considerably shorter than the value in $LiZr_6Cl_{15}Fe$ [2.709(1) Å], although in both cases the Cl^{a-a} atoms have nearby cation neighbors. If they are compared against $Zr_6Cl_{15}Co$, which does not contain countercations (529 $Å^3$ per cluster, Zr-Cl^{a-a} 2.624(1) Å), one may realize that the lattice expansions required by the incorporation of countercations are accomplished via different routes in $LiZr_6Cl_{15}Fe$ and $KZr_6Cl_{15}Fe$. In the Li containing cubic 6-15 structure, it is achieved by elongating Zr-Cl^{a-a} bonds while the linear chains are retained, because the two independent and interpenetrating cluster nets allow some free expansion, and the cation Li does not interfere with the main framework. In $KZr_6Cl_{15}Fe$, since the two types cluster chains are interconnected, elongation of Zr-Cl^{a-a} will cause stress on the chains. Under this circumstance, the lattice modifies itself by bending the chains.

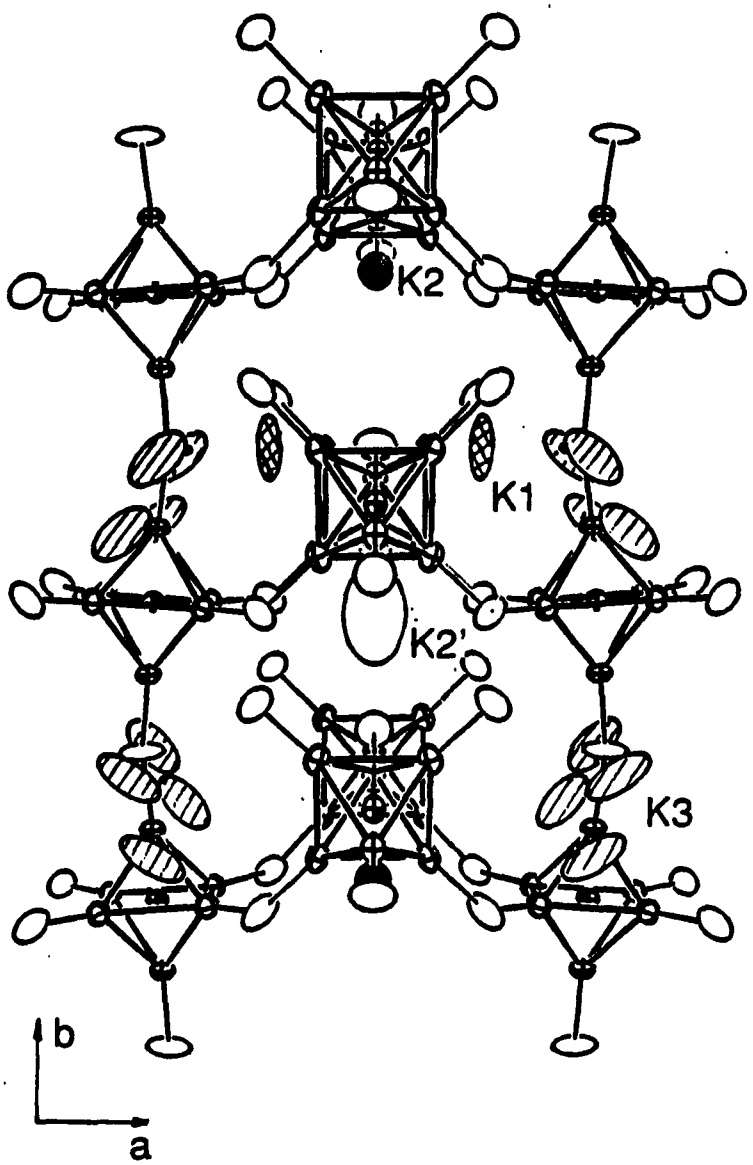

Figure 34. The [001] projection of $KZr_6Cl_{15}Fe$ showing the distortions of the cluster framework and the cation locations. Atoms are shown with their anisotropic thermal ellipsoids of 90% probability except the K3 ions which are represented with 30% probability. Cl^i atoms are omitted

The expansion of the cluster cores not only forces the individual chains to bend, but it also has effects on the packing of the chains. These are observed in the company of the distortions of the chlorine sublattice and modifications of the K positions. Based on the refined model, there are four crystallographically independent K sites. As this superstructure is only observed for $KZr_6Cl_{15}Fe$ and $RbZr_6Cl_{15}Fe$ but not for the corresponding Cs salt, it is evident that the countercations play important roles in the establishment of the lattice distortion. Their locations (Figure 34) and their coordination polyhedra (Figure 35) adopt to the change in the main structure framework and facilitate the modifications of the cluster chains.

The cation K1 in $KZr_6Cl_{15}Fe$ is related to the K site in $KCsZr_6Cl_{15}B$, and the latter is split into two positions in the supercell of $KZr_6Cl_{15}Fe$. While K1 fills one of these sites with occupancy of 19(1)%, its counterpart is left empty. Examining these two possible positions which are located between a pair of terminal Cl atoms, namely, Cl2 in the bent chain, and Cl3 or Cl3′ in the zigzag chain, one notices that the selected occupation of these sites creates an unbalanced force around the Cl2 atoms which pulls the cluster chains along the $\vec{b}$ axis toward the zigzag chains. As the K1 location changes along the $\vec{b}$ axis, the Cl2 atoms move to alternative directions in the plane perpendicular to the $\vec{c}$ axis, replacing the linear chains in the parent structure with wavy chains that have bent joints at the Cl^{a-a} (Cl2) atoms. K1 has coordination number of ten, and average K1-Cl distance of 3.48 Å (Table 34, the range is 3.23 Å to 3.60 Å). Its chemical environment is very similar to that of K in $KCsZr_6Cl_{15}B$ (average K-Cl distance 3.438 Å,

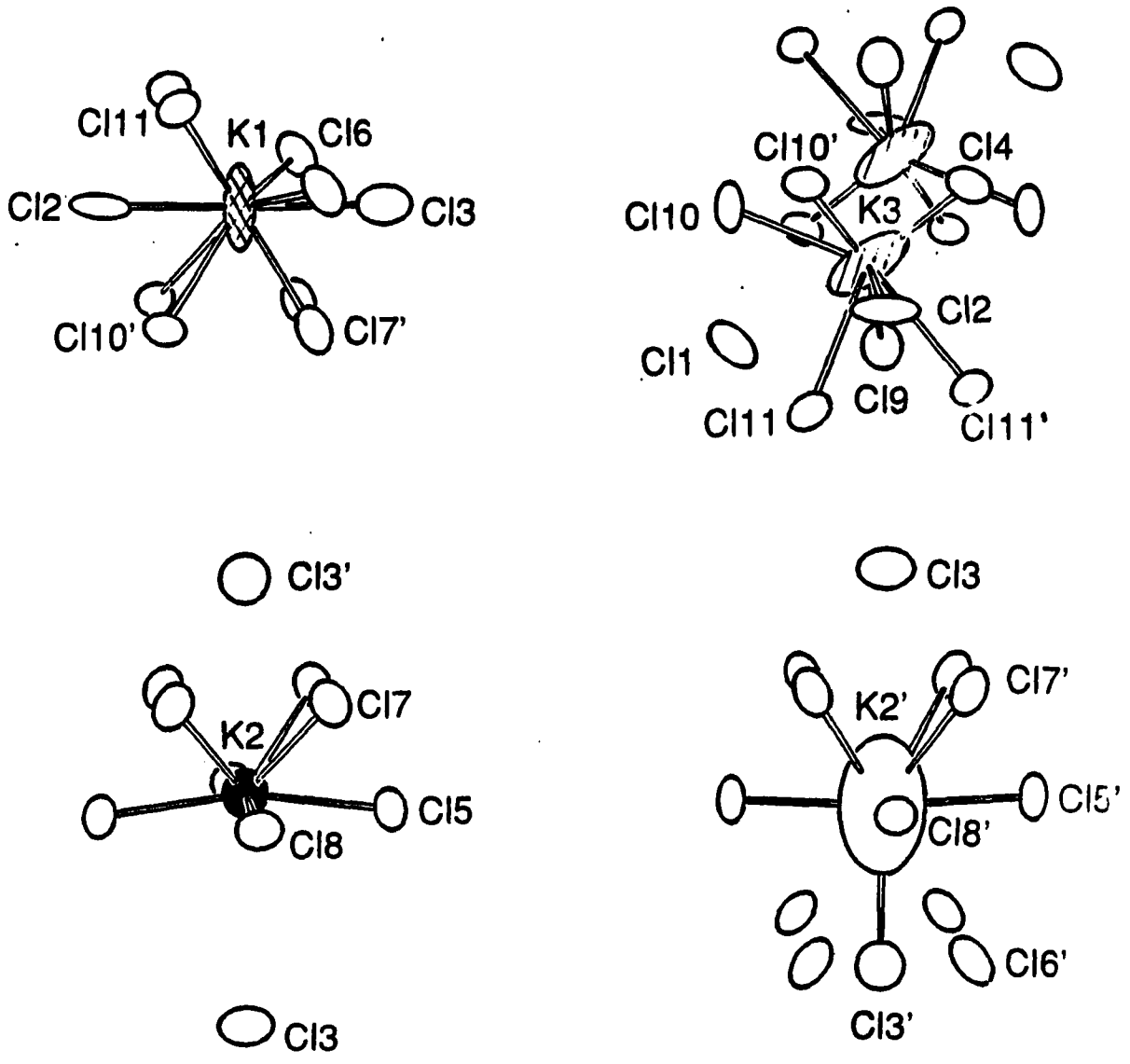

Figure 35. The coordination environments of the four K sites in $KZr_6Cl_{15}Fe$ (30% for K3, 90% probability for the rest of the atoms). Cl atoms with Cl–K distances smaller than 4 Å are connected to the K ions. The symmetries of these positions are: C_s at K1, mirror in the plane of the paper; C_{2v} for K2 and K2′, 2-fold axis vertical and one mirror in the plane of the paper; C_i between the two K3 ions. The views are identical to the one in Figure 34 with a horizontal and b vertical

Table 34. Important Distances (Å) in $KZr_6Cl_{15}Fe$: the Cations

K1-Cl2	x1	3.23(3)	K3-Cl1	x1	4.28(2)
K1-Cl3	x1	3.42(3)	K3-Cl2	x1	3.83(1)
K1-Cl6	x2	3.45(2)	K3-Cl4	x1	4.12(2)
K1-Cl7′	x2	3.50(3)	K3-Cl4	x1	3.46(2)
K1-Cl10′	x2	3.60(3)	K3-Cl9	x1	3.18(1)
K1-Cl11	x2	3.52(3)	K3-Cl10	x1	3.54(2)
$\bar{d}$	CN=10	3.48	K3-Cl10	x1	4.06(1)
			K3-Cl10′	x1	3.32(1)
			K3-Cl10′	x1	4.49(2)
			K3-Cl11	x1	3.85(2)
			K3-Cl11′	x1	3.83(1)
K2-Cl5	x2	3.488(6)	K2′-Cl5′	x2	3.481(6)
K2-Cl7	x4	3.375(8)	K2′-Cl7′	x4	3.77(2)
K2-Cl8	x2	3.450(5)	K2′-Cl8′	x2	3.528(4)
K2-Cl3′	x1	5.01(1)	K2′-Cl3′	x1	3.82(3)
K2-Cl3	x1	5.57(1)	K1′-Cl3	x1	5.50(3)
K2–Cl6	x4	5.909(9)	K1′–Cl6′	x4	4.64 (2)

range 3.347 to 3.529 Å).[47] The coordination polyhedron possesses the same symmetry, C_s, as in the parent structure and the Zr-Cl^i distances increase as the results of the lattice expansion and the tilting of the cluster units in the bent chain with respect to the $\vec{b}$ direction. The other effect of the bending of the cluster chain toward the K1 atoms is that the K1-Cl2 and K1-Cl3 become closer. As a consequence, the coordination environment is less isotropical, reflected by the thermal ellipsoid which is flat in the $\vec{a}$ direction. A K1-Cl2 distance that is significantly shorter than the sum of the crystal radii of K^+ and Cl^- (1.64 + 1.76 = 3.40 Å)[66] might be responsible for the low occupancy (19(1)%) of this position.

The empty counterpart of K1 has an average distance to its ten neighboring Cl atoms of 3.53 Å and is elongated along the $\vec{a}$ axis (Cl2-Cl3′, 7.59 Å vs Cl2-Cl3, 6.65 Å). Occupation of this position by a K ion is apparently less favorable.

Implied by their labels, K2 and K2′ share the common origin, which is the Cs1 position in the parent compound $KCsZr_6Cl_{15}B$. The K2 and K2′ atoms both reside in cavities between clusters in the zigzag chain, and are surrounded by a pair of zigzag chains, and a pair of bent chains. As the cluster chains along the $\vec{b}$ direction bend, the zigzag chains are brought together in pairs, and the distances between the center of a cluster chain and its two adjacent neighbors differ by 1.07 Å. This enlarges the K2 site while closing up the K2′ position. Both of these cation coordination polyhedra are still elongated along the $\vec{b}$ direction, resembling that for Cs1 in the parent compound, and the longest axis of the polyhedron around K2 (Cl3-K2-Cl3′ 10.58 Å) is 1.26 Å larger than

that for K2′ (Cl3-K2′-Cl3′ 9.32 Å). As the consequence, K2 sits at approximately the center of the larger cavity, while K2′ moves much closer to Cl3′ as an effort to maximize the coulombic interaction. This results in two cation sites with different coordination numbers. Since they both are large enough for K^+ ions, the observed difference in their occupancies is attributed to the difference in their coordination polyhedra and the cation-anion interactions. With a relatively isotropical environment and high coordination number, the fully occupied K2′ site is preferred over the K2 site that has the occupancy of 64(1)%. It is also noticed that both K2 and K2′ are closer to the Cl3′ positions, while a pair of K1 ions are near to the Cl3 atom, resulting in similar chemical environments for the two Cl^{a-a} atoms along the zigzag chain.

The K3 site in $KZr_6Cl_{15}Fe$ is derived from the Cs2 in the $KCsZr_6Cl_{15}B$.[47] In the parent compound, Cs2 (point symmetry C_{2h}) is located between a pair of linear chains. Its coordination polyhedron is known to be highly anisotropic, reflected by its peculiar thermal ellipsoid with rather large size. As a result of the lattice expansion accompanying the change of the interstitial atom, this type of cavity in $KZr_6Cl_{15}Fe$ becomes 0.08 Å larger. Counting only the nearest Cl neighbors (K–Cl <4 Å, CN=8), the average radius is 3.58 Å, about the same as that for the K2′ site. Yet, in order to provide more efficient K-Cl interactions, K3 prefers moving to one end of the highly anisotropic coordination. As the K moves off the center of the cavity that has the C_i symmetry, a pair of symmetry-related K positions that are 50% occupied and 3.01 Å apart are generated. Random occupation of

these sites in $KZr_6Cl_{15}Fe$ is required by the lattice symmetry from the crystallographic point of view. Furthermore, since the main body of the structure appears to agree well with the symmetry elements in the lattice, the two K atoms in this pair have identical chemical environment and therefore should have equal occupancies. As the split K cations are located at each end of the elongated thermal ellipsoid of Cs2 in $KCsZr_6Cl_{15}B$, the orientation of the thermal ellipsoid is now changed by about 90°. It points in the direction where it is rather open with Cl9 as the only close neighbor. The coupling of these two sites in the refinement process might have also contributed to the anisotropic thermal ellipsoid of K3.

It seems that although the expansion of the cluster core is essential in inducing the above structure modification, a smaller countercation that facilitates the disproportionation of the cation sites is another requirement that has to be fulfilled. In fact, $RbZr_6Cl_{15}Fe$ has a similar supercell, but the superstructure reflections on the axial photos are weaker compared with those for $KZr_6Cl_{15}Fe$, whereas, $CsZr_6Cl_{15}Fe$ gives clean Weissenberg pictures without any superstructure spots. This implies that the tendency for the structure distortion decreases as the counter cation becomes larger. In addition, the lattice parameters of the $MZr_6Cl_{15}Fe$ compounds do not show a regular change as the size of the countercation varies. Instead, an obvious lattice contraction is observed when K^+ is replaced by Rb^+. A similar phenomenon was observed in the carbide series and was explained in terms of the structure variations involving the cation position change.[47] Although in $KZr_6Cl_{15}Fe$ the countercation K is distributed over the

positions derived from K, Cs1 and Cs2 in $KCsNb_6Cl_{15}B$ rather than occupying one type of cation site, it is likely that structure modifications also occur in the iron compounds related to the selectivity of the cations toward the cavities of different size. In this series, it is plausible that the Rb^+ ions chooses only positions of the Cs types, resulting in the lattice contraction. Yet, with a relatively small size, Rb ions still prefer to occupy positions with optimized coordination conditions that are generated by splitting the oversized cavities, i.e., the Cs1 type in $CsNb_6Cl_{15}$ structure. Therefore, it enhances the distortion of the cluster framework in $RbZr_6Cl_{15}Fe$. As the size of the cation further increases, the undistorted large cavities in the lattice of $CsZr_6Cl_{15}Fe$ become suitable for Cs. Consequently, $CsZr_6Cl_{15}Fe$ does not exhibit the above superstructure.

As an additional observation, the group of 6-15 phases under discussion all have the distances between the centers of the neighboring clusters in the "linear" chain smaller than 10 Å, which are significantly shorter than the corresponding values (~10.2 Å) in the Nb_6F_{15} type compounds. Even in $KZr_6Cl_{15}Fe$ where the tension created by cluster expansion is released though bending of the linear chains, the $Zr\text{-}Cl^{a\text{-}a}$ distances in this direction [2.584(5) and 2.604(5) Å] are still shorter than those in all the Nb_6F_{15}-type compounds by at least 0.05 Å. As the lattice contracts in $RbZr_6Cl_{15}Fe$ or $CsZr_6Cl_{15}Fe$, the $Zr\text{-}Cl^{a\text{-}a}$ distances in the pseudo linear chains are estimated to be 2.58 Å and 2.52 Å, respectively. Due to the structure change, the differences in the $Zr\text{-}Cl^{a\text{-}a}$ distances between the two groups of 6–15 compounds is not surprising. Nevertheless, with the shortest $Zr\text{-}Cl^{a\text{-}a}$ distance in all

known Zr-Cl clusters, it is possible that $CsZr_6Cl_{15}Fe$ also undergoes lattice distortions. Since the superstructure is not observed for $CsZr_6Cl_{15}Fe$, this distortion must occur though a mechanism different from the one detected for $KZr_6Cl_{15}Fe$.

The structure analyses on $MZr_6Cl_{15}Fe$ (M = K, Rb, Cs) compounds that have the $CsNb_6Cl_{15}$ type cluster framework provide a new structure modification of the parent compound. Comparison of these phases with their carbide analogues reveals a correlation between structure and cluster size. In addition, the structure evolution associated with cation changes is also demonstrated. These observations suggest that nearly every structure feature must be the collective result of numerous factors, and compensation between these factors will result in a stable phase with a specific structure.

Zr_6Cl_{14} Type

Nb_6Cl_{14}[48] has many analogues in the zirconium halide cluster systems owing to the diversities of both the interstitial elements and the countercations. Previous research has provided Zr-I clusters of this type with a wide range of centering atoms, including main-group elements (B, C, P, Si, Al, K),[24,30,31] and transition metals (Mn, Fe, Co).[33] Following the electron counting rules more strictly, the centering atoms of the Zr_6Cl_{14} examples had been limited to boron and carbon[42] until the transition metals were introduced into the chloride systems in the present work. The new Zr_6Cl_{14} cluster phases with the transition metal interstitials, namely, $Zr_6Cl_{14}Fe$, $Zr_6Cl_{14}Mn$ and $MZr_6Cl_{14}Mn$ (M = alkali metal) resemble their main-group element analogues in terms of the

structure frameworks, and cluster electron counts are close to the optimal value. In addition, the $MZr_6Cl_{14}Mn$ series shows an interesting correlation between the lattice expansion and the size of the countercation. Although a parallel observation had also been made for the boron series,[42] it was not explained until the structure of $LiZr_6Cl_{14}Mn$ was solved.

Synthesis The new Zr_6Cl_{14} compounds that are related to Nb_6Cl_{14} are presented in Table 35. Among the 18-electron cluster phases, $Zr_6Cl_{14}Fe$ and $MZr_6Cl_{14}Mn$ (M = K, Rb, Cs)[76] could be made regularly in high yields with the appropriate stoichiometries, and these were often observed as side products co-existing with other cluster compounds, or as alternative products when a reaction failed to give the expected phases, implying a relatively high stability for these compounds. On the other hand, $LiZr_6Cl_{14}Mn$ could be only obtained as a single phase around 750°C. As the temperature was increased to 850°C, an on-stoichiometry reaction produced $Li_2Zr_6Cl_{15}Mn$ and ZrCl. Similarly, at 800°C, $NaZr_6Cl_{14}Mn$ was obtained in the company of ZrCl and other less reduced phases, but its yield could be greatly improved to about 90% (plus 10% of an unknown phase) by lowering the reaction temperature to 750°C. The differences of the thermal stabilities that separate the 18-electron $MZr_6Cl_{14}Mn$ compounds into two groups will be rationalized by their structural differences.

The 17-electron cluster $Zr_6Cl_{14}Mn$ was first observed after an attempt to synthesize $Zr_6Cl_{13}Mn$, a hypothetical 18-electron hypothetical analogue of $Zr_6Cl_{13}B$ with the $KZr_6Cl_{13}Be$ structure.[25] However, when the interstitial boron is replaced by Mn, the expansion of the cluster core

Table 35. Cell Parameters (Å) and Volume (Å^3) of $MZr_6Cl_{14}Z$ Compounds[a] (space group Cmca)

compound	a	b	c	V	cation site type[b]
$Zr_6Cl_{14}Mn$	14.486(2)	12.793(3)	11.803(2)	2187.2(7)	–
$LiZr_6Cl_{14}Mn$	14.507(2)	12.858(2)	11.786(2)	2198.6(5)	*a*
$NaZr_6Cl_{14}Mn$	14.478(6)	13.026(4)	11.752(4)	2216(1)	*a*
$KZr_6Cl_{14}Mn$	14.347(2)	12.838(2)	11.796(2)	2172.6(2)	*b*
$RbZr_6Cl_{14}Mn$	14.3451(8)	12.8444(8)	11.8453(6)	2182.5(2)	*b*
$CsZr_6Cl_{14}Mn$	14.381(1)	12.869(1)	11.933(1)	2208.4(3)	*b*
$Zr_6Cl_{14}Fe$	14.332(4)	12.772(4)	11.778(6)	2156(1)	–

[a]All values are from Guinier powder diffraction data.

[b]The cation site type *a* is defined as the Li position in $LiZr_6Cl_{14}Mn$, and *b* as the Cs position in $CsZr_6I_{14}C$.

must introduce an instability in the less flexible lattice that contains not only outer-outer chlorine sharing but also the inner-inner atom sharing. Apparently, this instability is sufficient to cause the formation of a 17-electron cluster with the Nb_6Cl_{14} structure,[48] and the less than optimal metal-metal bonding is traded for the more favorable lattice energy. This again indicates that the stability of a cluster phase is the result of a delicate balance between numerous factors. As a 17-electron cluster, the formation of $Zr_6Cl_{14}Mn$ is also sensitive to the reaction temperatures. Stoichiometric reactions at 800°C yielded only noncluster phases such as $ZrCl_4$ and ZrCl, while $Zr_6Cl_{14}Mn$ was produced when the temperature was lowered to 700°C.

As an additional observation, the $NaZr_6Cl_{14}Mn$ reaction system was noted to produce a mixture of the target compound and an unknown phase. This unidentified phase has been repeatedly observed and can be obtained as the main product with the NaCl:$NaZr_6Cl_{14}Mn$ ratio of 5:1. It provides a large number of reflections in the low angle region of a powder X-ray diffraction pattern, and it will be necessary to obtain single crystal to determine its structure.

Single crystal X-ray analyses were performed on $Zr_6Cl_{14}Fe$ and $LiZr_6Cl_{14}Mn$ to confirm the stoichiometries and to explain the puzzling lattice expansion trend in the $MZr_6Cl_{14}Mn$ series. The single crystal of $Zr_6Cl_{14}Fe$ was not obtained from several reactions started with the appropriate stoichiometry. Instead, small crystals were found from a reaction loaded to make "$NaZr_6Cl_{14}Fe$" (750°C, slow cooling). Based on the lattice constants, which were essentially identical to those of $Zr_6Cl_{14}Fe$, it seemed probable that the planned 19-electron cluster phase

had never formed. The structural analysis on one of the crystals also proved that Na was absent in the lattice. Following the same path, $LiZr_6Cl_{14}Mn$ was also obtained from an off-stoichiometry reaction that was designed to produce $Li_2Zr_6Cl_{15}Mn$ (950-800°C, temperature gradient). Rather than a single phase product, two cluster phases, namely, $LiZr_6Cl_{14}Mn$ and $Li_2Zr_6Cl_{15}Mn$, were obtained from this reaction. Although the total yield of both cluster phases was no higher than 40%, the crystals enabled the single crystal X-ray analyses on the two compounds.

Structure determinations Intensity data for the structure refinement of $Zr_6Cl_{14}Fe$ were collected on a SYNTEX diffractometer. Because of the small size of the crystal, the intrinsic properties of the structure that result in a small number of strong reflections, and the limited power of the incident beam, the observed diffraction intensities were low. A thirty-minute rotation photo on the SYNTEX diffractometer barely gave enough reflections to determine the orientation matrix. Based on the fifteen reflections, BLIND gave a primitive monoclinic cell which was transformed to the conventional C-centered orthorhombic cell in the same setting as the model compound, Nb_6Cl_{14}. Then low angle reflections were replaced by higher angle ones to improve the accuracy of the orientation matrix. Axial photos were taken for both the primitive cell and the C-centered cell, and all the expected mirror symmetries confirmed that the Laue symmetry of the latter was mmm. Data from two octants ($hk\ell$, $-hk\ell$) with $2\theta < 55°$ were collected (Table 36) for the C-centered cell using variable scan rates from 2.02° to 19.53° per minute. An empirical absorption correction was applied to

Table 36. Crystal Data for $Zr_6Cl_{14}Fe$

space group	Cmca (No. 64)
Z	4
a, Å[a]	14.332(4)
b, Å	12.772(4)
c, Å	11.778(6)
V, Å^3	2152(1)
crystal dimen, mm	0.10 x 0.09 x 0.05
data collection instrument	SYNTEX $P2_1$
scan mode	ω
$2\theta_{max}$, deg	55
reflections	$\pm h, k, \ell$
measured	2723
observed	778
observed independent	489
absorp coeff μ, cm^{-1} (Mo Kα)	51.52
range of transm coeff	0.543-0.721
R_{ave}, %	4.7
second ext coeff	0.12(8) x 10^{-4}
R, %	5.5
R_w, %	5.5
largest residue peak, e$^-$/Å^3	0.6

[a]Guinier powder diffraction data (18 observations).

the raw data based on three ψ-scans at approximately 15°, 25°, and 40° 2θ angles.

The data set was then reduced and averaged in space group Cmca after the absence conditions (hkℓ, h+k=2n; h0k, k=2n; hk0, h=2n) were confirmed. Positions of zirconium and chlorine atoms in $Zr_6Cl_{14}C$ were used as the starting model, and following the isotropic refinements of these atoms (R = 0.162, R_w = 0.222), a electron difference map was calculated, from which a residue of about 10 $e^-/Å^3$ was found at the center of the zirconium cluster. Therefore, an iron was added to the structure refinement, and the isotropic refinement of the two zirconiums, five chlorines, and the iron gave R=0.071, R_w=0.116. At this stage the different map was calculated, and it was essentially flat except a few ghost peaks of 0.6 $e^-/Å^3$ around Cl(5). The anisotropic refinement of the thermal parameters improved R to 0.055. The final difference map which was flat within 0.6 $e^-/Å^3$ did not provide any evidence that sodium atoms existed in the structure. Effort was also made to refine the occupancy of the interstitial iron atom. However, no significant change in the iron occupancy (102(2)%) was observed. Therefore it is reported as fully occupied, in agreement with the 18-electron rule. The final structure solution is presented in Table 37.

The data collection on $LiZr_6Cl_{14}Mn$ were conducted on a CAD4 diffractometer. The orientation matrix and the cell constants were established by employing the program SEARCH, INDEX, and TRANS successively. Axial photos about the three principal axes and the [110] direction were then taken, confirming that the unit cell was C-centered orthorhombic. Considering the fact that the structure determination

Table 37. Positional and Thermal Parameters for $Zr_6Cl_{14}Fe$

	x	y	z	B_{11}
Zr1	0.3778(1)	0.0739(2)	0.8805(2)	0.92(8)
Zr2	0	0.3440(3)	0.8877(4)	0.9(1)
Cl12	0.1231(6)	0.0866(4)	0.2517(6)	1.7(3)
Cl2	0.1240(6)	0.2548(6)	0.0073(6)	1.8(2)
Cl3	1/4	0.342(1)	1/4	1.8(4)
Cl4	0	0.157(1)	0.758(1)	1.4(4)
Cl5	0.2472(6)	0	0	0.7(4)
Fe1	0	0	1/2	1.0(3)

B_{22}	B_{33}	B_{12}	B_{13}	B_{23}	B_{eq}
1.09(8)	0.49(7)	−0.08(9)	0.2(1)	0.01(9)	0.83(8)
1.1(1)	0.4(1)	0	0	−0.3(1)	0.8(1)
1.6(3)	1.0(2)	0.4(5)	0.5(2)	0.3(1)	1.43(3)
1.4(2)	1.0(2)	0.4(2)	0.4(2)	−0.2(2)	1.4(2)
1.5(4)	1.2(2)	0	−1.0(4)	0	1.5(3)
1.6(4)	0.9(4)	0	0	−0.5(3)	1.3(4)
2.3(5)	1.5(4)	0	0	0.8(4)	1.5(4)
0.9(4)	0.2(3)	0	0	0.3(3)	0.7(3)

might involve refinement of a light atom, Li, two octants of data were collected up to 2θ of 60° with the reflection condition h+k=2n. Other important crystal data are listed in Table 38.

On examining the data, two additional independent reflection conditions were observed (0kℓ, ℓ=2n; hk0, k=2n), which implied that the possible space groups were Cc2a (a nonstandard setting of Aba2), or Ccmb (a nonstandard setting of Cmca). Since the parent compound Nb_6Cl_{14} belongs to space group Cmca,[48] Ccmb was chosen and transformed to the standard setting. The data were first corrected for nonlinear decay (4.1% in 35.9 hours) since the three intensity standards decreased at rather different rates (2,-4,-4 0.08% per hour; -1,-5,-3 0.19% per hour; 8,-4,0 0.06% per hour). Then, an empirical absorption correction was applied with 10 ψ-scans. Symmetry extinct reflections were eliminated from the data set after the validity of the reflection conditions were confirmed (hkℓ, k+ℓ=2n; h0ℓ, ℓ=2n; hk0 h=2n). The reduced data set including all reflections (2768) with non-negative intensities (I>0) were averaged. The main part of the structure framework, including atoms other than Li, was refined with strong reflections ($I>3\sigma_I$, 883) by using $Zr_6Cl_{14}Fe$ as the model. The isotropic and anisotropic refinements were quickly converged at R=4.1%, R_w=5.3%.

According to the cluster electron counting rule and the composition of the starting materials, there should have been a countercation, Li^+, in the lattice. Therefore, efforts were made to locate the Li atom by including weaker reflections ($0<I<3\sigma_I$) in the refinements. A difference Fourier map was calculated, yet the position corresponding to the counter cation site in $CsZr_6I_{14}Fe$ was clean. Instead, there was a 1.9

Table 38. Crystal Data for $LiZr_6Cl_{14}Mn$

space group	Cmca (No. 64)
Z	4
a, Å[a]	14.507(2)
b, Å	12.858(2)
c, Å	11.786(2)
V, Å^3	2198.5(7)
crystal dimen, mm	0.22 x 0.24 x 0.24
data collection instrument	ENRAF NONIUS CAD4
scan mode	ω
$2\theta_{max}$, deg	60
reflections	h,k,±ℓ
measured	3414
observed	(I>0) 2768 (I>3σ_I) 1864
observed independent	1350 883
absorp coeff μ, cm^{-1} (Mo Kα)	55.2
range of transm coeff	0.88 - 1.00
R_{ave}, %	5.1
second ext coeff	6(2) x 10^{-8}
R, %	6.8
R_w, %	5.3
largest residue peak, e$^-$/Å^3	+1.6 (0.48 Å, Zr1)
	-1.7 (0.69 Å, Mn)

[a]Guinier powder diffraction data (55 observations).

$e^-/Å^3$ residue peak in one interstice surrounded by six Cl's. This peak was then assigned to Li, and simultaneous refinement of its thermal parameters and the multiplicity was successful. The converged refinement gave reasonable occupancy of 25.2(2)% for each of the 16 symmetry related positions, which corresponds to one Li per cluster unit. In addition, the Li thermal parameters and the Li-Cl distances were also plausible.

To examine the contribution of the weak reflections in the structure determination, the data were reaveraged with 3σ cut-off, and the refinement was repeated starting at the point that the Li atom was located. Anisotropic refinement of all the eight heavy atoms gave a rather flat difference Fourier map, with the highest positive residue peak being a ghost peak around Zr2 (1.33 $e^-/Å^3$, 0.53 Å). However, among the top five peaks, there were two that were close to the Li position determined by including weak reflections (1.32 and 1.33 $e^-/Å^3$, 0.23 Å apart). After refining Li at this position and its thermal parameters as well as the multiplicity, the structure solution was essentially the same as the one refined with all reflections, which suggests that although the weak reflections did help to locate the light atom Li, their contribution was not enough to make a difference in the final results. The standard deviations of parameters were slightly higher with fewer observations.

The multiplicity of the Mn position was also studied. Again, shrinkage in thermal parameters and a decrease in occupancy to 90.0(4)% accompanied by a reduction of the negative ghost peaks around Mn were observed no matter whether the data set included the weaker reflections

or not. Based on the arguments presented before, this phenomenon was considered to be a result of a possible imperfect crystallographic work rather than a defect interstitial position. The interstitial site was set to be fully occupied, which caused slight increase of the negative residue around Mn from -1.3 e/Å^3 to -1.6 e$^-$/Å^3.

The final difference map was essentially flat, showing ghost peaks around Zr1, Zr2 and Mn. However, among those with electron density larger that 1 e$^-$/Å^3, there was one residue peak of 1.0 e$^-$/Å^3 at the origin of the unit cell, which corresponds to the cation position $CsZr_6I_{14}Fe$. Refinement of a second Li atom was attempted, yet failed as indicated by an unreasonably large B_{iso}. Therefore, the stoichiometry determined by single crystal X-ray analysis agree well with that of the 18 e$^-$ cluster compound $LiZr_6Cl_{14}Mn$. The positional and thermal parameters refined with strong reflections ($I>3\sigma_I$) are reported in Table 39.

Structure description The structure frameworks in $Zr_6Cl_{14}Fe$ and $LiZr_6Cl_{14}Mn$ are essentially identical to that in the parent compound Nb_6Cl_{14}. It contains a three-dimensional cluster network $[Zr_6Cl_{10}{}^iCl_{2/2}{}^{i-a}]Cl_{4/2}{}^{a-a}Cl_{2/2}{}^{a-i}$ (Figure 36) and, in $LiZr_6Cl_{14}Mn$, a countercation Li^+ occupying a distorted chlorine octahedral interstice between clusters.

Similar to those in $Zr_6Cl_{14}C$ and $Zr_6Cl_{14}B$,[42] the cluster cores with Fe and Mn interstitials may be considered as undergoing a tetragonal distortion (Tables 40 and 41;, the Zr-Mn and Zr–Fe distances differ by 0.039 Å, 2%, and 0.046 Å, 2%, respectively), which is expected because of the asymmetric nature of the terminal chlorine atoms. However, the

Table 39. Positional and Thermal Parameters for $LiZr_6Cl_{14}Mn$

	x	y	z	B_{11}
Zr1	0.38093(5)	0.07327(5)	0.88124(6)	1.35(2)
Zr2	0	0.34636(8)	0.88801(9)	1.46(3)
Cl1	0.1234(1)	0.0870(1)	0.2503(2)	1.89(7)
Cl2	0.1239(1)	0.2557(2)	0.0063(2)	1.94(6)
Cl3	1/4	0.3411(2)	1/4	1.83(9)
Cl4	0	0.1576(2)	0.7600(2)	1.9(1)
Cl5	0.2491(2)	0	0	1.23(8)
Mn	0	0	1/2	1.95(9)
Li	0.251(4)	0.676(4)	0.153(5)	-

B_{22}	B_{33}	B_{12}	B_{13}	B_{23}	B_{eq}
1.72(2)	1.06(2)	-0.03(2)	-0.09(2)	0.02(2)	1.38(1)
1.57(3)	1.16(3)	0	0	-0.05(4)	1.40(2)
2.04(6)	1.55(5)	0.28(6)	0.58(6)	0.48(6)	1.83(3)
1.77(5)	1.72(6)	0.50(6)	-0.33(6)	-0.22(5)	1.81(3)
2.17(9)	1.96(8)	0	-0.52(9)	0	1.99(5)
2.5(1)	1.33(8)	0	0	-0.46(9)	1.90(5)
2.51(9)	1.61(8)	0	0	0.43(8)	1.79(4)
2.09(9)	1.38(8)	0	0	0.01(8)	1.81(4)
–	–	–	–	–	1.9(8)

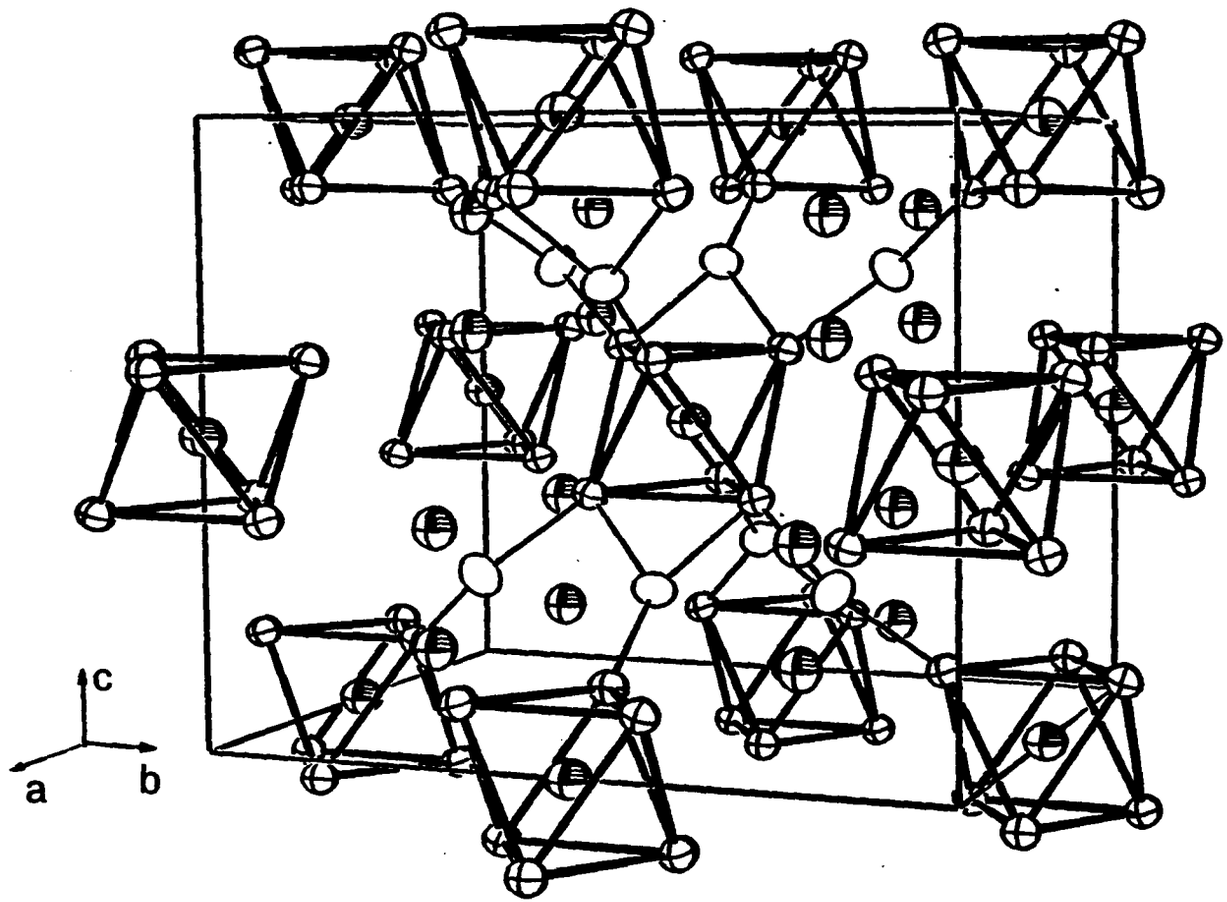

Figure 36. The three-dimensional structure framework and the Li^+ locations $LiZr_6Cl_{14}Mn$ (90% probability). The Cs atoms in the related $CsZr_6I_{14}C$ structure are at the corners and face centers of the unit cell

Table 40. Interatomic Distances in $Zr_6Cl_{14}Fe$ (Å)

Zr–Zr	Zr1-Zr1	X2	3.390(5)
	Zr1-Zr1	X2	3.503(4)
	Zr1-Zr2	X4	3.420(4)
	Zr1-Zr2	X4	3.410(5)
	$\bar{d}$		3.246
Zr–Fe	Zr1-Fe	X4	2.438(2)
	Zr2-Fe	X2	2.392(4)
	$\bar{d}$		2.423
$Zr-Cl^{i}$	Zr1-Cl5	X2	2.526(7)
	Zr1-Cl2	X2	2.557(8)
	Zr1-Cl1	X2	2.552(7)
	Zr2-Cl1	X2	2.544(9)
	Zr2-Cl2	X2	2.539(8)
	$\bar{d}$		2.544
$Zr-Cl^{i-a}$	Zr1-Cl4	X2	2.62(1)
$Zr-Cl^{a-i}$	Zr2-Cl4	X2	2.84(2)
$Zr-Cl^{a-a}$	Zr1-Cl3	X4	2.624(7)

Table 41. Important Distances and Angles in $LiZr_6Cl_{14}Mn$

Distances (Å)						
Zr-Mn	Zr1-Mn	x4	2.4147(7)	Li-Cl1	x1	2.44(6)
	Zr2-Mn	x2	2.376(1)		x1	2.45(6)
	$\bar{d}$		2.402	Li-Cl2	x1	2.78(6)
Zr-Zr	Zr1-Zr1	x2	3.375(1)		x1	2.71(6)
		x2	3.455(1)	Li-Cl3	x1	2.41(5)
	Zr1-Zr2	x4	3.384(1)	Li-Cl5	x1	2.89(5)
		x4	3.392(1)	$\bar{d}$		2.61
	$\bar{d}$		3.397			
$Zr\text{-}Cl^{i}$	Zr1-Cl5	x4	2.551(2)			
	Zr1-Cl1	x4	2.576(2)			
	Zr1-Cl2	x4	2.568(2)			
	Zr2-Cl1	x4	2.564(2)			
	Zr2-Cl2	x4	2.556(2)			
	$\bar{d}$		2.563			
$Zr\text{-}Cl^{i\text{-}a}$	Zr1-Cl4	x4	2.633(2)			
$Zr\text{-}Cl^{a\text{-}i}$	Zr2-Cl4	x2	2.857(3)			
$Zr\text{-}Cl^{a\text{-}a}$	Zr1-Cl3	x4	2.685(1)			
Angles (°)						
	Cl1-Zr1-Cl2	x4	173.54(7)			
	Cl4-Zr1-Cl5	x4	172.39(6)			
	Cl1-Zr2-Cl2	x4	171.38(8)			
	average		172.44			

striking 0.08 Å difference of the two Zr1-Zr1 distances makes the distortion pattern greater than the cases of the carbide and boride clusters, in which the Zr1–Zr1 distances differ by 0.04 Å. On one hand, this difference is not surprising due to the different functions of the bridging chlorines; on the other hand, it is not obvious why this discrepancy should be more profound in the transition-metal compounds. It could be the result of the difference in the electronic structure between 14 e^- and 18 e^- clusters, and/or the consequence of cluster expansion. Except the distortion discussed above, the cluster unit behaves rather normally in the sense that the average Zr-Fe and Zr-Mn distances agree with those in other related cluster phases (e.g., $Li_2Zr_6Cl_{15}Mn$, 2.4111(6) Å; $Cs_3ZrCl_5Zr_6Cl_{15}Mn$, 2.4142(4) Å; $LiZr_6Cl_{15}Fe$, 2.424(1) Å; $KZr_6Cl_{15}Fe$, ave. 2.423 Å). When these two isostructural 18-electron clusters are compared with each other, a smaller cluster core in $LiZr_6Cl_{14}Mn$ is observed. Similar to what is observed in the transition-metal centered iodide cluster systems, a lengthening of the Zr–Cl^i distances accompanies the decrease in cluster core size. At the same time, the lattice of $LiZr_6Cl_{14}Mn$ is expanded due to the incorporation of the countercation Li^+, which results in the stretching of the Zr–Cl^a distances.

One other interesting aspect of these single crystal studies is the locatition of the countercation in $LiZr_6Cl_{14}Mn$. In contrast to the larger monovalent cations, which occupy a twelve-coordinate position in the close-packed layers, the single crystal study and ^7Li solid state NMR data (below) have shown that Li^+ chooses a distorted octahedral interstice between close-packed layers (Figure 37). The average Li-Cl

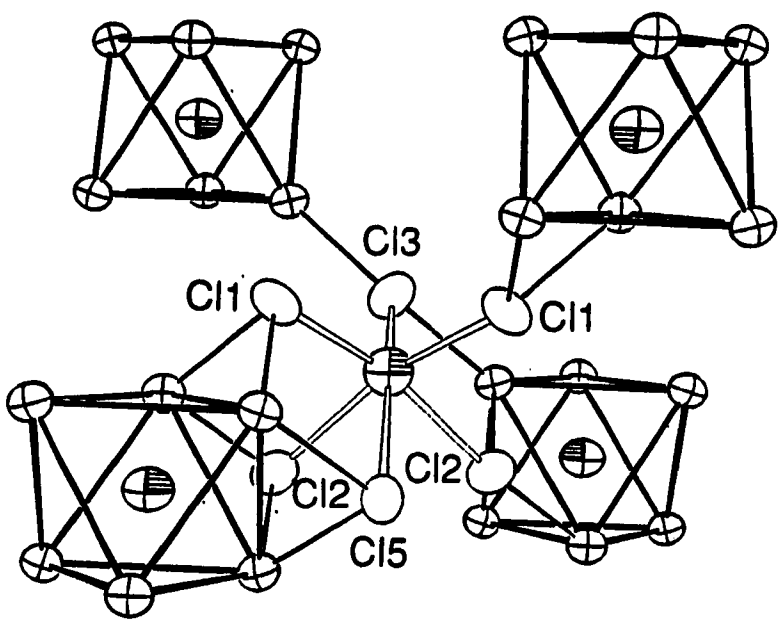

Figure 37. The Li coordination environment in $LiZr_6Cl_{14}Mn$ (90% probability)

distance (2.61 Å) is slightly longer than the sum of Cl^- and six-coordinate Li^+ crystal radii (1.67 + 0.90 Å)[66] as expected for a partially occupied position. The location of the Li is not at the center of the interstice but closer to one of the triangular faces, resulting in three short and three long Li-Cl distances. This displacement of the Li atom by about 0.6 Å is not surprising when the size of the vacancy and the surrounding cluster units are taken into consideration. As shown by Figure 37, on one side of the Li coordination polyhedron, there are Zr atoms residing between the same pair of Cl layers at rather close distances (<3.76 Å), while on the other side, the Zr atoms are farther away (>3.96 Å). The interaction between the positive charged ions displaces Li^+ from the center of the slight oversized polyhedron. This explains the three short Li-Cl distances which do not agree with the value for coordination number of six and, since the other three Cl atoms have Li–Cl distances larger than the expected value, a lower effective coordination number may result. This fact is helpful in understanding the quadrupole coupling constant of Li in this phase, which is smaller than that in $Li_2Zr_6Cl_{15}Mn$. Since the 12-coordinate cation position has an average distance of 3.64 Å to Cl atoms, occupation of it cannot provide sufficient Li-Cl interaction, and therefore it is left empty.

^{7}Li solid state NMR for $LiZr_6Cl_{14}Mn$ To provide supporting evidences for the results of the single crystal study on $LiZr_6Cl_{14}Mn$, ^{7}Li solid state NMR experiments were conducted. The sample was prepared by reacting stoichiometric amounts of starting materials at 750°C for 20 days followed by annealing at 580°C for 20 days. The product was a

black powder and was free of impurities detectable by X-ray diffraction. A 50 mg sample was sealed in a piece of Pyrex tubing under vacuum, and a static spectrum was taken at room temperature.

The spectrum (Figure 38) shows a signal with a sharp central peak and two rather featureless side bands. The fact that only one signal is observed is consistent with the X-ray analysis which revealed that there is only one type of Li position in $LiZr_6Cl_{14}Mn$. The line shape of the signal is distinctly different from that of LiCl, which is a typical Gaussian peak (Figure 4), and this confirms the existence of Li in a position with symmetry lower than cubic. The chemical shift of the signal with respect to LiCl of −2.2 ppm is rather small compared with +11.6 ppm in $Li_6Zr_6Cl_{18}H$, indicating similar chemical environments of Li atoms in $LiZr_6Cl_{14}Mn$ and LiCl, i.e., the number of Cl atoms around the Li and the charge distributions between Li and Cl are similar in both compounds. The poor profile of the side bands presumably is associated with the poor crystallinity of the sample which was prepared at a relatively low temperature. In addition, instrumental limitations caused difficulties to locate the centers of the side bands, therefore making it impossible to determine the asymmetric parameter (η) and the quadrupole coupling constant (Q_c) with accuracy. Nevertheless, the less distinctive side bands, in contrast to those in $Li_2Zr_6Cl_{15}Mn$, imply a symmetry lower than axial for the Li in $LiZr_6Cl_{14}Mn$ ($\eta>0$), which agrees with the evidence provided by X-ray analysis that Li sits on a general position ($\eta\neq0$). Furthermore, the line profile of this spectrum is certainly different from that for $\eta=1$, which has washed-out singlets and shoulders, and is essentially one broad central peak.[83] The single

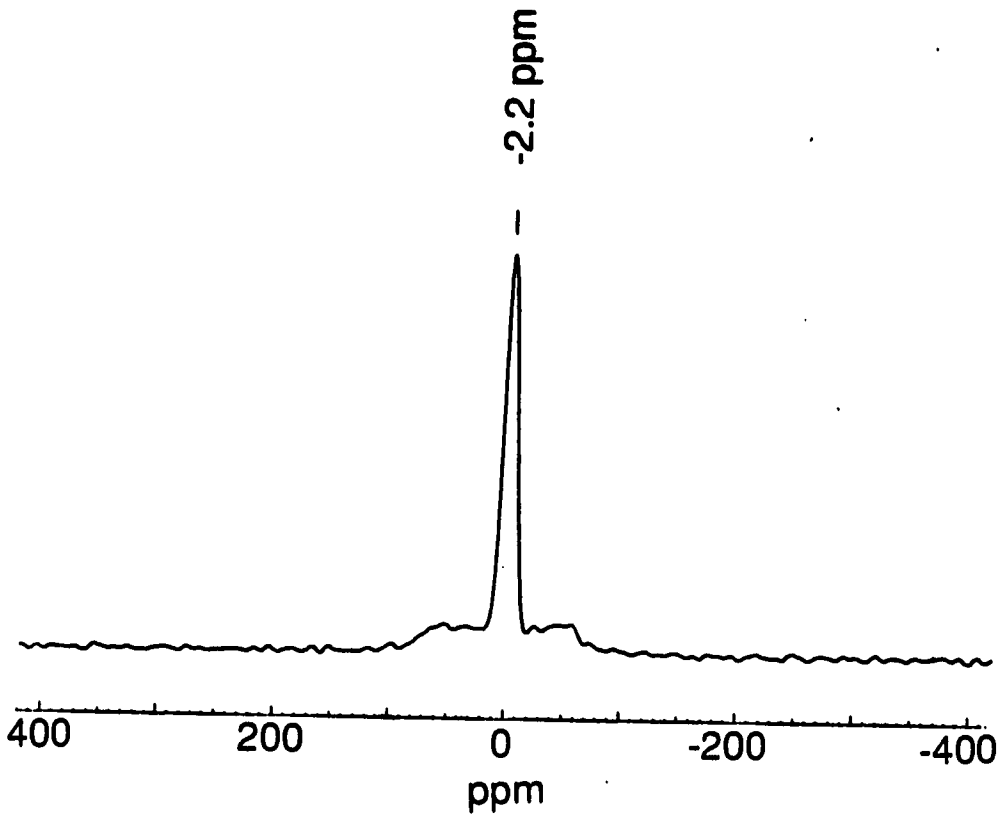

Figure 38. A room temperature ^{7}Li solid state NMR spectrum of $LiZr_6Cl_{14}Mn$

crystal X-ray diffraction indicated that although the Li site does not have a well-defined axial symmetry, the three short and three long Li-Cl distances impose a pseudo three-fold axis along $\vec{c}$, and η is expected to be not too far away from zero. Assuming η is close to 0, one can estimate Q_c to be smaller than but in the vicinity of 0.014 MHz by assigning the edges of the side bands to be the singlets at ±60 ppm ($\gamma_1 = Q_c = 120$ ppm, 14 kHz). The small value of Q_c compared with 58 kHz for $Li_2Zr_6Cl_{15}Mn$ is not understood; yet, it is probably associated with the lower occupancy (25% vs 33%), lower symmetry, and the three long Li-Cl distances in this compound. Again, the results of ^7Li NMR are not conclusive by themselves. However, they support the fact that Li is in the lattice and agree with the symmetry of Li position established by X-ray structure determination.

The two structure variations in the $MZr_6Cl_{14}Z$ series It was known that the cell volume of $LiZr_6Cl_{14}B$ does not fit into the volume-change trend of the other $MZr_6Cl_{14}B$ compounds, although it also has a 14 cluster electron count.[42] Similarly irregular lattice expansion is observed for the $MZr_6Cl_{14}Mn$ series (Table 35), and based on the experience, such phenomena usually imply structure modifications.

The present study on $LiZr_6Cl_{14}Mn$ was able to locate the Li atom in the 6-14 lattice by combining ^7Li solid state NMR and X-ray diffraction. It proves that besides $CsZr_6I_{14}C$, [16,24] there is a second modification of the original Nb_6Cl_{14} structure.[48] While a large cation such as Cs occupies the 12-coordinate position, the smaller Li cation sits in a six-coordinate position with 25% occupancy in $LiZr_6Cl_{14}Mn$. With this information, the discontinuity in the cell volume vs the volume

increment[79] of the countercations in the $MZr_6Cl_{14}Z$ (Z = B, Mn) series (Figure 39, Table 42) can be rationalized. Although $Zr_6Cl_{14}Mn$ is a 17-electron cluster phase, it still may be used as a helpful reference, as long as the lattice expansion owing to the oxidation of the cluster core, which is usually less profound than that caused by cation variations, is also kept in mind.

For the Mn series, Li^+ and apparently Na^+ choose the six-coordinate posititon, because the alternative 12-coordinate position is too large to provide sufficient cation-anion interactions. Taking r_{Cl} = 1.79 Å, which is the half of the average Cl–Cl distance in $LiZr_6Cl_{14}Mn$, the r_+[66] of Li or Na is larger than the size of a six-coordinate interstice (~0.41 r_- for a closest packed anion lattice). The incorporation of these cations enlarges the interstice and therefore causes lattice expansion with respect to $Zr_6Cl_{14}Mn$. As the r_+/r_- increases, the CN=6 position becomes less favorable compared with the CN=12 site, and the K, Rb and Cs compounds adopt the latter $CsZr_6I_{14}C$ structure. In this case, for cations with r_+/r_- smaller than one, the interaction between cations and the chlorine atoms tends to pull the Cl atoms closer to certain extent, resulting a net volume decrease with respect to $Zr_6Cl_{14}Mn$; while for Cs^+ with r_+/r_- greater than one, the repulsion between nuclei induces a lattice expansion, as expected.

A similar trend in volume variation was also observed for the boride series with the discontinuity occurring between $LiZr_6Cl_{14}B$ and $NaZr_6Cl_{14}B$. Yet, the irregular cell volume of $LiZr_6Cl_{14}B$ was not explained because of the lack of conclusive evidences to verify the content and the location of Li in the lattice. As the Li involvement is

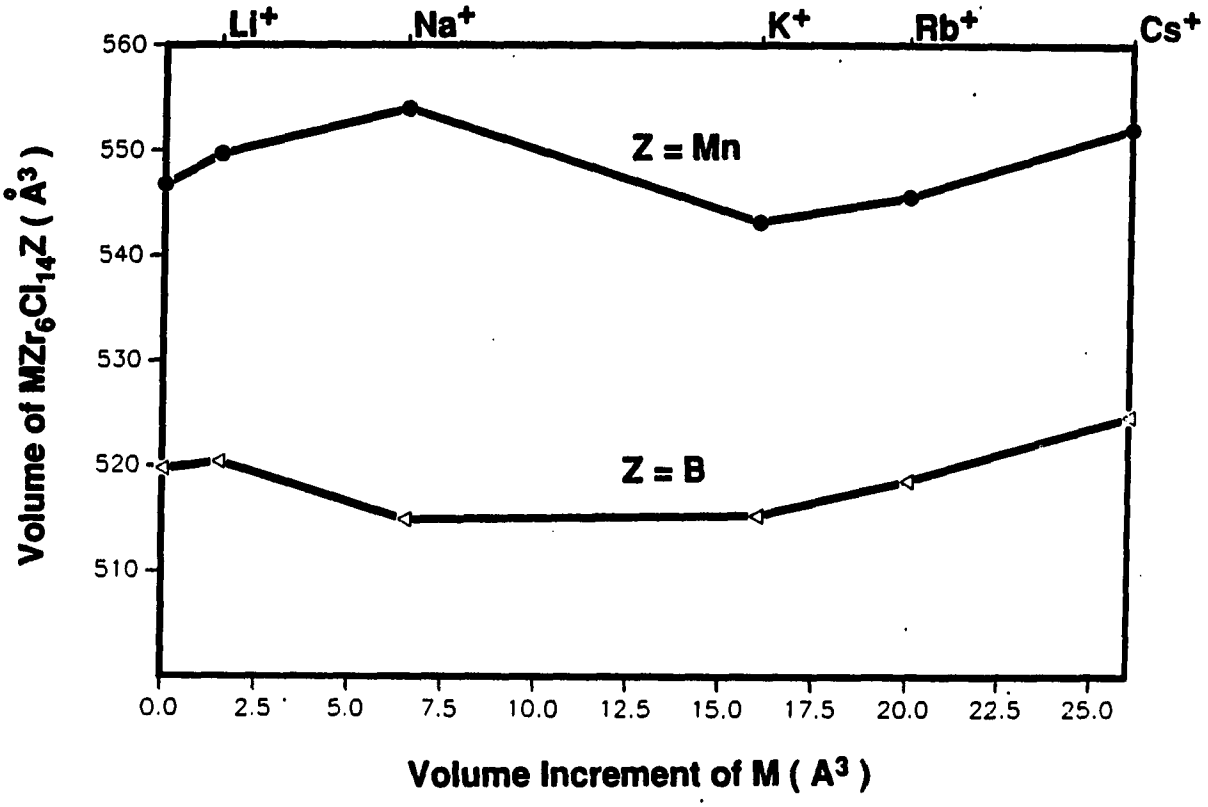

Figure 39. The correlation between the formula volume and the volume increment of the countercations in the $MZr_6Cl_{14}Z$ (M = alkali metal, Z = Mn, B) series

Table 42. The Relationship Between the Cation Sizes and the Structure Types in the $MZr_6Cl_{14}Z$ Series (M = alkali metal, Z = Mn, B)

	M^+			Z = Mn		Z = B	
M	r(CN=6)	r(CN=12)	volume increment($Å^3$) (CN=6)	formula volume ($Å^3$)	structure type[a]	formula volume ($Å^3$)	structure type[a]
–	–	–	–	546.8(2)	–	519.7(1)	–
Li	0.90	–	1.5	549.7(1)	a	520.4(2)	a
Na	1.16	1.53	6.5	554.0(3)	a	514.9(1)	b
K	1.52	1.78	16	543.2(2)	b	515.3(1)	b
Rb	1.66	1.86	20	545.6(1)	b	518.6(1)	b
Cs	1.81	2.02	26	552.1(1)	b	524.7(1)	b

[a]Structure type a is defined as the $LiZr_6Cl_{14}Mn$, and b as $CsZr_6I_{14}C$ type.

confirmed and its coordination environment determined via the structural analysis on $LiZr_6Cl_{14}Mn$, the volume change pattern in the boride systems may be rationalized. The turning point for the structure change from $LiZr_6Cl_{14}Mn$ to $CsZr_6I_{14}C$ type is at Na^+, clearly due to the size change of the cation position associated with the smaller size of the cluster core.

Besides the peculiar volume change in these series, additional evidences that support the cation assignments were obtained from powder X-ray diffraction studies. Switching the positions from the Cs site in $CsZr_6I_{14}C$ structure to the Li site in $LiZr_6Cl_{14}Mn$ causes obvious intensity change for the reflections in the low angle region of calculated powder patterns for the heavier alkali metals (K, Rb, Cs). The cation assignments made by comparing the calculated intensities with the observed ones agree that the heavier alkali metals occupying the 12-coordinate position. On the other hand, due to the low diffraction power of the lighter alkali metals, Li and Na, an unambiguous judgment of the structure types can not be made on the basis of the powder patterns.

The observed structure modifications in the $MZr_6Cl_{14}Z$ series present another example of a delicate balance between chemical interactions and space-filling efficiency. In these groups of compounds, cation-anion interactions are the dominating factor with respect to the space-filling requirement. For smaller alkali metals, the choice of the cation position allows the optimized coulombic interaction at the cost of lowering the space filling efficiency. As the size of the cation

becomes larger, a different cation position is selected by the heavier alkali metals, which provides both sufficient cation-anion interactions and higher densities of the materials.

General Observations

Zirconium chloride clusters centered by 3d transition metal elements

Electronic states The new zirconium chloride cluster phases stabilized by 3d transition metal interstitials resemble their iodide analogues in terms of the electronic structure. With a few exceptions, the optimal bonding condition for these compounds involves 18 cluster electrons. Extended-Hückel calculations performed in the iodide systems demonstrated the substitution of a centered main-group atom by a transition metal results in the optimal stability increasing from 14 to 18 cluster electrons through the addition of the interstitial-based (e_g^4) nonbonding state.[33] As also noticed in the case of main-group-element interstitials, the chloride clusters obey the electron counting rule more restrictively than the iodide clusters, in which the matrix effect is a major factor in phase formation and stabilization. In addition, the zirconium chlorides have the centering atoms covering Mn through Ni, while the iodides have interstitial elements range from Cr to Co.[33]

Furthermore, careful analysis of the calculations[24,33] on $[Zr_6I_{18}C]^{4-}$ and $[Zr_6I_{18}Fe]^{4-}$ suggests that as the consequence of the interactions between the zirconium 4d orbitals and interstitial 3d orbitals, the t_{2g} orbital which are the HOMO in the main-group atom centered clusters are split in energy and the upper set becomes the LUMO, t_{2g}^*, in a

transition-metal-centered cluster. Since the t_{2g}^* lies below the a_{2u} orbital, which is the LUMO for clusters with main group interstitials, a slight band gap decrease may accompany the substitution of a transition metal into a cluster core.

As direct supporting evidence, it was observed that in the zirconium chloride systems the two groups of cluster phases have distinctively different colors. While the main-group-element centered cluster phases are usually deep red under transmitted light, their transition metal counterparts exhibit a dark purple color under similar conditions. Assuming the results of the above calculations may be applied to the chloride systems, the origin of the colors is the symmetry-allowed electron transition between the HOMO and the LUMO (e.g., $t_{2g} \rightarrow a_{1u}$ in $Zr_6I_{18}C^{4-}$; $t_{1u} \rightarrow t_{2g}^*$ in $Zr_6I_{18}Fe^{4-}$). The observed change in color corresponds to a shift of the absorption band to a longer wave length region from a decrease in the band gap, as suggested by the results from the extended Hückel calculations.

Although at the present no calculation has been conducted for a transition-metal-centered zirconium chloride cluster, the similarities between the orbital diagrams[24,37] of $Zr_6I_{18}C^{4-}$ and $Zr_6Cl_{18}C^{4-}$ in the region near the Fermi level imply that the validity of the calculation on $Zr_6I_{18}Fe^{4-}$ may be extended to $Zr_6Cl_{18}Fe^{4-}$, and the color change in the chloride systems may be explained qualitatively with the results for the iodide clusters. In addition, it is also noticed that the band gaps given by the calculations on the zirconium clusters are about 1.3 eV, which corresponds to absorptions in the infrared region. The discrepancy between the calculations and the experimental observations

may be justified with the fact that the energy of the empty states may not be precisely defined by extended Hückel method. Quantitative measurements of the absorption band of the cluster compounds may provide a more conclusive evaluation of their electronic states.

Structures Although the electronic states of the transition metal stabilized chloride and iodide clusters are similar, they are strikingly different from each other from the structural point of view. As observed previously for the main-group interstitial cluster phases, the known iodide clusters exhibit only three structure types,[16,24,31-33,36] namely, the $Zr_6I_{12}C$, the Nb_6Cl_{14} and the $K_2ZrCl_6 \cdot Zr_6Cl_{12}H$ types. On the other hand, the (transition-metal-centered-zirconium) chloride cluster phases show a large variety of stoichiometries and structure types.[26] When the chloride cluster compounds with different classes of centering atoms are compared, similarities as well as differences are observed. They have many common structure types, namely, the $K_2ZrCl_6 \cdot Zr_6Cl_{12}H$,[22,42] $CsLuNb_6Cl_{18}$,[43] $Ba_2Zr_6Cl_{17}B$,[38] $Cs_3(ZrCl_5)Zr_6Cl_{15}Mn$[10] types and those related to $CsNb_6Cl_{15}$[46,47] and Nb_6Cl_{14}[48,24] types. The structure types that have examples with main group elements but not transition metals or vise versa are usually those that have a restrictive requirement on the cluster size. As the cluster containing transition metals have Zr–Zr distance about 0.2 Å larger than the cluster cores with main-group element, the Zr atoms in the former are closer to the plane of the square faces formed by the four Cl^i atoms and the Cl^i–Zr–Cl^i angle across these faces increases ($\geq 173°$ vs $<170°$). These effects destabilize certain structure types, such as the $Zr_6Cl_{13}Be$ type. Meantime, they generate cluster phases with novel structure features that

are unique to the transition metal interstitials, e.g., the Nb_6F_{15}[17] structure. In a moderate case, the expansion of a cluster core may induce modifications of parts of the structure with the retention of the main framework, as in the case of $KZr_6Cl_{15}Fe$.

Before the discovery of the zirconium chloride clusters stabilized by transition metals, the size of the interstitial atoms was considered as one major reason for the absence of the chloride analogues with larger main-group atoms, e.g., Al, Si, P, Ge, which are known in iodide systems. The successful syntheses of the transition metal centered phases clearly indicates that the metal cores of the chloride clusters are flexible enough to accommodate large interstitials, since the sizes of the 3d transition metals are about the same as those of third period main-group elements. As the formation of a cluster phase is a collective effect of numerous optimized conditions such as the electron count, strong interstitial to zirconium bonding interaction, suitable counterions, and high space filling efficiency, the reason for the lack of certain phases is also complicated. The absence of the above examples might be because the favorable experimental conditions have not been found, or the competing phases are more stable with respect to the target compounds. Nevertheless, an unidentified phase was observed in the powder patterns from reactions aimed at making $K_2BaZr_6Cl_{18}Ge$ (700–800°C, 25 days).[87] The unknown phase was reproducible, providing a large number of reflections with d_{max} ~10.5 Å. If this compound is indeed proven to be a Ge-centered cluster phase, it will support the statement that the zirconium chloride clusters are also capable of

accepting the large main-group interstitial atoms as their iodide counterparts.

Cluster distortions and matrix effect

Theoretically speaking, there are two major causes that lead to the distortion of the cluster cores, namely, a less than ideal electronic configuration and matrix effects. Since the majority of the known zirconium chloride cluster phases have the optimal 14 or 18 cluster based electrons, an electronically driven cluster distortion is less frequently observed. Even in the cases where the cluster phases do not obey the electron counting rules, the cluster cores may not necessarily experience serve distortions (e.g., $Li_6Cl_{18}H$, 13 e^-/cluster).[39] Systematic structural studies, on the other hand, have often revealed relationships between cluster distortions and ionic interactions or matrix effects. This correlation may be verified by analyzing the structures of a group of compounds. To simplify this process, examples that obey the 14 or 18 electron rule and have point symmetry S_6 imposed by the space group are chosen so that the observed trigonal distortion may be considered as the contribution solely from the matrix effect.

The average distances that are relevant to the trigonal distortions in four cluster phases are tabulated (Table 43). With Figure 40 as the reference, which shows the $[Zr_6Cl_{18}Z]$ cluster units with countercations in their first coordination sphere (M–Cl distance ~ sum of crystal radii), it is observed that the location of the countercations has a great influence on the type and extent of the distortion of a cluster core. In the first three examples, the cations are situated above and below the pair of triangular faces normal to the three-fold axis,

Table 43. The Observed Trigonal Distortions and the Matrix Effect in Selected Zirconium Chloride Cluster Phases

Compound (Structure type) Space group		$(K,Ba)_2BaZr_6Cl_{18}C$ $(K_2ZrCl_6 \cdot Zr_6Cl_{12}H)$ $R\bar{3}$	$CsLaZr_6Cl_{18}Fe$ $(CsLuNb_6Cl_{18})$ $P\bar{3}1c$	$Ba_3Zr_6Cl_{18}Be$ $(Ba_3Zr_6Cl_{18}Be)$ $R\bar{3}c$	$Cs_3(ZrCl_5)Zr_6Cl_{15}Mn$ $(Cs_3(ZrCl_5)Zr_6Cl_{15}Mn)$ $R\bar{3}c$
Zr–Zr	d_1[a]	3.2248(3)	3.391(1)	3.3154(3)	3.4019(8)
	d_2[b]	3.2118(3)	3.3813(9)	3.276(1)	3.4296(7)
	Δ[c]	0.0130(6)	0.010(2)	0.039(1)	−0.028(2)
	Δ/d_{ave}	0.40%	0.30%	1.18%	−0.82%
Zr–Cl[i]	Zr–Cl1	2.549(1)	2.563(4)	2.597(3)	2.567(1)
	Zr–Cl2	2.524(1)	2.547(4)	2.557(2)	2.585(1)
Zr–Cl[a]	Zr–Cl3	2.6207(5)	2.671(2)	2.683(2)	2.7294(7)
M		(K,Ba)	Cs	Ba2	Cs
Cl–M	Cl1–M	3.697(2)	4.025(2)	3.682(4)	3.582(1)
	Cl2–M	3.646(1)	–	3.464(2)	3.768(2)
	Cl3–M	3.2160(6)	3.842(2)	3.090(2)	3.6814(6)

[a]Zr–Zr distance in the triangle faces of the clusters normal to the 3-fold axis.

[b]Zr–Zr distance around the waist of the cluster.

[c]$\Delta = d_1 - d_2$.

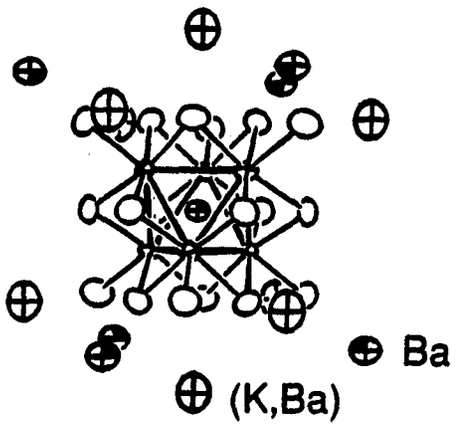

$(K,Ba)_2BaZr_6Cl_{18}C$

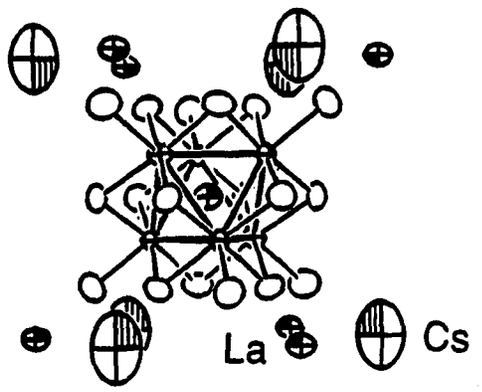

$CsLaZr_6Cl_{18}Fe$

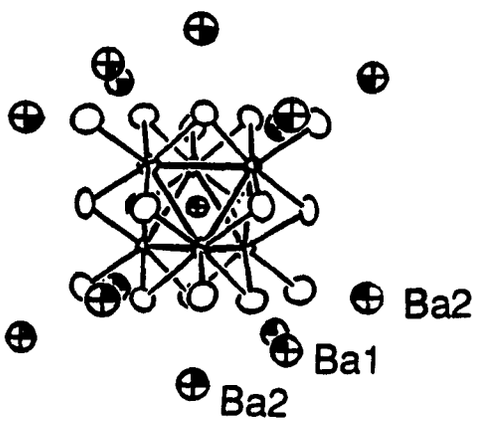

$Ba_3Zr_6Cl_{18}Be$

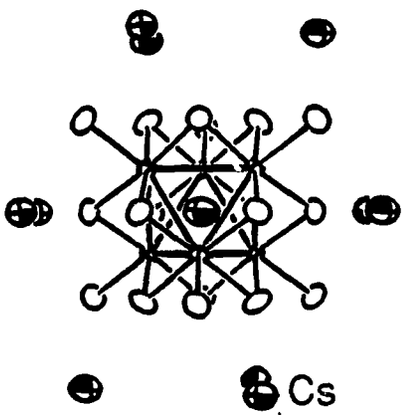

$Cs_3(ZrCl_5)Zr_6Cl_{15}Mn$

Figure 40. The location of the countercations around the cluster cores that experience trigonal distortions in selected compounds. In each case the cluster unit possesses S_6 symmetry with the principal axis vertical

imposing static pressure along the principal axis, and resulting in the observed trigonal compression. In contrast, the cluster core in $Cs_3(ZrCl_5)Zr_6Cl_{15}Mn$ exhibits a trigonal elongation as the Cs^+ ions locating around the waist of the cluster are closer to the metal core than those at the top or bottom (Cs–Mn 6.45 Å vs 6.95 Å).

Since the cluster cores are wrapped inside the Cl atoms, the distortions are likely accomplished via the coupled M–Cl and Cl–Zr interactions. There is an obvious correlation between $Zr–Cl^i$ and Zr–Zr distances, while the $Zr–Cl^a$ distances may vary with the structure types and the cations. In the cases where the $M–Cl^i$ interactions result in Cl1–Zr distances that are larger than the Cl2–Zr distances, the cluster cores have the Zr–Zr distances $d_1 > d_2$, corresponding to trigonal compressions. Following the same argument, if the M–Cl2 interaction is stronger, the Zr–Cl2 distances becomes longer, and therefore a trigonal elongation is observed.

The magnitude of the distortions depends on several factors. First, it depends on the electric field of the cations. When $(K,Ba)_2BaZr_6Cl_{18}C$ and $Ba_3Zr_6Cl_{18}Be$ are compared, which have similar cation arrangements around the clusters, the latter experiences a distortion three times as severe as that in the former. The degree of distortions also relies on the M–Cl distances or the M–cluster distances. Although in $CsLaZr_6Cl_{18}Fe$ and $Cs_3(ZrCl_5)Zr_6Cl_{15}Mn$ the major contributions of the distortion are from the same cation, Cs^+, a much larger Cs–Cl distance in the former results in the less pronounced distortion. Finally, when the subtle differences are concerned, the change in the structure type

and the counterions that are further away from the clusters also have to be taken into consideration.

FUTURE WORK

During the last decade, exploratory research in the zirconium chloride cluster systems has generated over 70 new compounds with over 20 structure types and structure variations in the $M_x[Zr_6Cl_{12}Z]Cl_n$ (x, n = 1–6) series.[26] The systematic investigations have made the family of Zr–Cl clusters one of the most thoroughly studied and best described. It also provides enormous possibilities in cluster compositions and structure variations.

At the present, the centering atoms in the Zr–Cl cluster systems are limited to small main-group element (H, Be–N) and 3d transition metals (Mn–Ni). Attempts to introduce Al, Si, Cr, or Mo into zirconium chloride cluster systems have failed.[42,87] Yet, encouraged by the successes in the iodide cluster systems,[34,35] it is possible that under optimized conditions, new Zr–Cl cluster phases that capture larger main group elements or heavier transition metals, e.g., Ge, Ru, Rh, may also be obtained, and novel structure features may be observed. The further expansion of the cluster core may induce different degrees of cluster condensation, forming phases with cluster dimers, chains or superclusters that are known only for cluster systems of other metals.[7,26] These may fill the structure gap between the known Zr–Cl phases with discrete cluster units and ZrCl containing an extended metal array and contribute to the understanding of the evolution of the structures and the variation of electronic states.

The search for metal cluster phases may also be extended to other systems, such as Ti and Hf halide systems. Limited studies of the titanium chlorides have not yet provided analogues of the zirconium

clusters.[87] However, triangular Ti_3 fragments with substantial metal–metal bonding interactions similar to those in Ti_7Cl_{16}[88] were found in MTi_4Cl_{11} (M = K, Cs). Several additional unidentified phases were also observed. Interesting phases were also observed in the reduced Ti–I systems.[89] Primary research in the Hf–I systems,[89] however, have not provided any phases more reduced than HfI_3. Although the Ti and the Hf systems may not have the same cluster chemistry as its zirconium counterpart due to the contractions of the d orbitals in Ti and Hf, the investigations in these areas may be just as exciting.

REFERENCES

1 Schäfer, H.; von Schnering, H.-G. *Angew. Chem.* 1964, *76*, 833.

2 Wells, A. F. "Structural Inorg. Chem."; 5th ed.; Clarendon Press: Oxford, 1984; pp. 432–437.

3 Corbett, J. D. *Acc. Chem. Res.* 1981, *14*, 239.

4 Simon, A.; Mattausch, Hj.; Miller, G. J; Bauhofer, W.; Kremer, R. K. in "Handbook on the Physics and Chemistry of Rare Earths" Ed. Gschneidner, K. A., Jr.; Eyring, L. North-Holland Physics Publishing: Amsterdam, 1991, Vol. 15.

5 Simon, A. *Angew. Chem., Int. Ed. Engl.* 1988, *27*, 159.

6 Köhler, J.; Miller, G.; Simon, A. *Z. Anorg. Allg. Chem.* 1989, *568*, 8.

7 Simon, A.; Köhler, J.; Tischtan, R.; Miller, G. *Angew. Chem., Int. Ed. Engl.* 1989, *28*, 1662.

8 Harned, H. S. *J. Am. Chem. Soc.* 1913, *35*, 1078.

9 Rogel, F.; Ph.D. Dissertation, Iowa State University, Ames, IA, 1990.

10 Rogel, F.; Zhang, J.; Payne, M. W.; Corbett, J. D. *Adv. Chem. Ser.* 1990, *226*, 369.

11 Gronwold, F.; Kjekshus, A.; Raaum, F. *Acta Crystallogr.* 1961, *14*, 930.

12 Bateman, L. R.; Blorent, J. F.; Dahl, L. F. *J. Am. Chem. Soc.* 1966, *88*, 1082.

13 Simon, A.; von Schnering, H.-G.; Schäfer, H.; *Z. Anorg. Allg. Chem.* 1967, *355*, 295.

14 Chevrel, R.; Sergent, M.; Prigent, J. *J. Solid State Chem.* 1971, *3*, 515.

15 Corbett, J. D.; Daake, R. L.; Poeppelmeier, K. R.; Guthrie, D. H. *J. Am. Chem. Soc.* 1978, *100*, 652.

16 Guthrie, D. H.; Corbett, J. D. *Inorg. Chem.* 1982, *21*, 3290.

17 Schäfer, H.; von Schnering, H.-G.; Niehues, K.-J.; Nieder-Vahrenholz, H. G. *J. Less-Common Met.* 1965, *9*, 95.

18 Bauer, D.; von Schnering, H.-G. *Z. Anorg. Allg. Chem.* 1968, *361*, 259.

19 Corbett, J. D. *Adv. Chem. Ser.* 1980, *186*, 329.

20 Wijeyesekera, S. D.; Corbett, J. D., Ames Laboratory, Iowa State University, unpublished research; 1984.

21 Simon, A. *Z. Anorg. Allg. Chem.* 1967, *355*, 311.

22 Imoto, H.; Corbett, J. D.; Cisar A. *Inorg. Chem.* 1981, *20*, 145.

23 Lauker, J. W. *J. Am. Chem. Soc.* 1978, *100*, 5305.

24 Smith, J. D.; Corbett, J. D. *J. Am. Chem. Soc.* 1985, *107*, 5704.

25 Ziebarth, R. P.; Corbett, J. D. *J. Am. Chem. Soc.* 1985, *107*, 4571.

26 Ziebarth, R. P.; Corbett, J. D. *Acc. Chem. Res.* 1989, *22*, 256.

27 Hwu, S.-J.; Corbett, J. D.; Poeppelmeier, K. R. *J. Solid State Chem.* 1985, *57*, 43.

28 Warkentin, E.; Masse, R.; Simon, A. *Z. Anorg. Allg. Chem.* 1982, *491*, 323.

29 Warkentin, E.; Simon, A. *Rev. Chem. Miner.* 1982, *20*, 488.

30 Smith, J. D.; Corbett, J. D. *J. Am. Chem. Soc.* 1986, *108*, 1927.

31 Rosenthal, G.; Corbett, J. D. *Inorg. Chem.* 1988, *27*, 53.

32 Hughbanks, T.; Rosenthal, G.; Corbett, J. D. *J. Am. Chem. Soc.* 1986, *108*, 8289.

33 Hughbanks, T.; Rosenthal, G.; Corbett, J. D. *J. Am. Chem. Soc.* 1988, *110*, 1511.

34 Hughbanks, T.; Corbett, J. D. *Inorg. Chem.* 1988, *27*, 2022.

35 Hughbanks, T.; Corbett, J. D. *Inorg. Chem.* 1989, *28*, 631.

36 Payne, M. W.; Corbett, J. D. Iowa State University, unpublished research, 1989.

37 Ziebarth, R. P., Ph.D. Dissertation, Iowa State University, Ames, IA, 1987.

38 Zhang, J.; Corbett, J. D. *J. Less-Common Met.* 1989, *156*, 49.

39 Zhang, J.; Ziebarth, R. P.; Corbett, J. D., Ames Laboratory, Iowa State University, unpublished research, 1987.

40 Ziebarth, R. P.; Corbett, J. D. *J. Am. Chem. Soc.* 1989, *111*, 3272.

41 Simon, A.; von Schnering, H.-G.; Schäfer, H. *Z. Anorg. Allg. Chem.* 1968, *361*, 235.

42 Ziebarth, R. P.; Corbett, J. D. *J. Solid State Chem.* 1989, *80*, 56.

43 Ihmaine, S.; Perrin, C.; Sergent, M. *Z. Acta Crystallogr.* 1989, *C45*, 705.

44 Ziebarth, R. P.; Corbett, J. D. *Inorg. Chem.* 1989, *28*, 626.

45 Ziebarth, R. P.; Corbett, J. D. *J. Am. Chem. Soc.* 1988, *110*, 1132.

46 Imoto, H.; Simon, A., Max-Planck-Institut für Festkörperforschung, Stuttgart, Germany, unpublished research, 1980.

47 Ziebarth, R. P.; Corbett, J. D. *J. Am. Chem. Soc.* 1987, *109*, 4844.

48 Simon, A.; von Schnering, H.-G.; Wöhrle, H.; Schäfer, H. *Z. Anorg. Allg. Chem.* 1965, *339*, 155.

49 Holmberg, B.; Dagerhamn, T. *Acta Crystallogr.* 1961, *15*, 919.

50 Meyer, G.; Ax, P. *Mat. Res. Bull.* 1982, *17*, 1447.

51 Corbett, J. D. *Inorg. Syn.* 1983, *22*, 15.

52 Corbett, J. D. in "Solid State Chemistry: Techniques" Ed. Cheetham, A. K.; Day, P. Clarendon Press: Oxford, 1987, Chap. 1.

53 Miller, A. E.; Daane, A. H.; Haberman, C. E.; Beaudry, B. J. *Rev. Sci. Inst.* 1963, *34*, 644.

54 Clark, C. M.; Smith, D. K.; Johnson, G. J. A Fortran IV Program for Calculating X-Ray Powder Diffraction Patterns – Version 5, Department of Geosciences, Pennsylvania State University: University Park, PA, 1973.

55 Imoto, H. Ames Laboratory, Iowa State University, unpublished research, 1978.

56 Takusagawa, F., Ames Laboratory, Iowa State University, unpublished research, 1981.

57 Werner, P.-E. TREOR-V4, Department of Structural Chem., Arrhenius Laboratory, University of Stockholm: Stockholm, Sweden, 1984.

58 Sheldrick, G. M.; SHELXS-86, Programs for Structure Determination, Universit Göttingen, Germany, 1986.

59 SDP User's Guide, Enraf-Nonius, Delft, Holland and B. A. Frenz & Associate, Inc., College State, TX, 1988.

60 TEXSAN: Single Crystal Structure Analysis Software, Version 5.0, Molecular Structure Corporation, The Woodlands, TX, 1989.

61 International Tables for X-Ray Crystallography; Kynoch Press: Birmingham, England, 1968, Vol. III.

62 Walker, N.; Stuart, D. *Acta Crystallogr.* 1983, *A39*, 159.

63 Coppens, P.; Hamilton, W. C. *Acta Crystallogr.* 1970, *A26*, 71.

64 Johnson, C. K. ORTEP, a Fortran Thermal-Ellipsoid Plot Program for Crystal Structure Illustrations, Oak Ridge, National Laboratory, Oak Ridge, TN, 1970.

65 Chu, P. J.; Ziebarth, R. P.; Corbett, J. D.; Gerstein, B. C. *J. Am. Chem. Soc.* 1988, *110*, 5324.

66 Shannon, R. P. *Acta Crystallogr. Sec. A* 1976, *A32*, 751.

67 Corbett, J. D. *Pure and Applied Chem.* 1984, *56*, 1527.

68 Broll, A.; Schäfer, H. *J. Less-Common Met.* 1970, *22*, 367.

69 Broll, A.; Ph.D. Dissertation, Westfischen Wilhelms-Universität, Münster, Germany, 1969.

70 von Schnering, H.-G., private communication, 1989.

71 Speckelmeyer, B.; von Schnering, H.-G. *Z. Anorg. Allgem. Chem.*, 1971, *386*, 27.

72 Koknat, F. W.; McCarley, R. E. *Inorg. Chem.* 1974, *13*, 295.

73 Perrin, C.; Ihmaine, S.; Sergent, M. *New J. Chem.* 1988, *12*, 321.

74 Ziebarth, R. P.; Corbett, J. D. *J. Less-Common Met.* 1988, *137*, 21.

75 Simon, A.; Böttcher, F. Max-Plank-Institut für Fortkörperforschung, Stuttgart, Germany, unpublished research, 1988.

76 Hughbanks, T. R.; Corbett, J. D. Iowa State University, Ames, IA, unpublished research, 1987.

77 Pauling, L. *J. Am. Chem. Soc.* 1947, *69*, 542.

78 von Schnering, H.-G.; Nesper, R. *Angew. Chem. Int. Ed. Engl.* 1987, *26*, 1059.

79 Biltz, W. in "Raumchemie der Festen Stoffe", Leopold Voss Verlag: Leipzig, Germany, 1934.

80 Bray, P. J.; Gravina, S. J. in "Advances in Materials Characterization II", Ed. Snyder, R. L.; Condrate, R. A. Sr.; Johnson, P. F. Plenum Publishing Corporation: New York, 1985.

81 von Günther, H.; Moskau, D.; Bast, P.; Schmalz, D. *Angew. Chem.* 1987, *99*, 1241.

82 McCart, B. R.; Barnes, R. G. *J. Chem. Phys.* 1968, *48*, 127.

83 Creel, R. B.; Barnes, R. G. *J. Chem. Phys.* 1972, *56*, 1549.

84 West, A. R. in "Solid State Chemistry and its Applications", John Wiley and Sons: New York, 1984.

85 Wells, A. F. in "Structural Inorg. Chem.", 5th ed., Clarendon Press: Oxford, 1984, Chap. 6.

86 Cotton, F. A.; Wilkinson, G. in "Advanced Inorganic Chemistry", 5th ed., John Wiley & Sons: New York, 1988, Chap. 1.

87 Zhang, J.; Corbett, J. D., Department of Chemistry, Iowa State University, Ames, IA, unpublished research, 1989.

88 Schäfer, H.; Laumanns, R. *Z. Anorg. Allg. Chem.* 1981, *474*, 135.

89 Qi, R.-Y.; Corbett, J. D., Department of Chemistry, Iowa State University, Ames, IA, unpublished research, 1989.

ACKNOWLEDGEMENTS

The author wishes to thank Professor John D. Corbett for his support, guidance, encouragement and enthusiasm during the course of this work.

Dr. Lee M. Daniels, Professor Robert A. Jacobson and his group are gratefully thanked for their assistance with diffractometers and helpful discussion in crystallography. Thanks are due to Dr. Venceslav Rutar, Professor Richard G. Barnes, Professor Bernard C. Gerstein and his group for their specialties on solid state NMR studies; Dr. Lance L. Miller and Jerome E. Ostenson for conducting magnetic susceptibility measurements. The advice from Professor Hugo F. Franzen is greatly appreciated. Professor Karl A. Gschneidner and his group are thanked for the use of metal-working facilities. The cooperation and suggestions from Dr. Robin P. Ziebarth and Dr. Timothy R. Hughbanks are gratefully acknowledged.

Arnold M. Guloy is kindly thanked for many constructive discussions. The author is indebted to Mrs. Shirley A. Standley for her help extended beyond this thesis. The friends and coworkers of the author will be warmly remembered for their help, encouragement and understanding.

Special thanks to the author's parents, Rong-Sen Zhang, Chun-Hui Huang, and grandmother, Dai-Ru Sheng for raising her with love and providing her the courage to reach her dreams.

Finally, the author wishes to thank her husband Ren Xu and her son Patrick Mengchih Xu for filling her life besides chemistry with love and joy, and for giving her reasons to work and live with dignity.